이학박사 학위논문

GaN microrod LED for bio-medical applications

바이오메디컬 응용을 위한 질화갈륨 마이크로막대

발광 다이오드

2020 년 7 월

서울대학교 대학원

물리천문학부

송 민 호

Doctoral thesis

GaN microrod LED for bio-medical applications

July 2020

Minho Song

Department of Physics and Astronomy,

Seoul National University

GaN microrod LED for bio-medical applications

바이오메디컬 응용을 위한 질화갈륨 마이크로막대
발광 다이오드
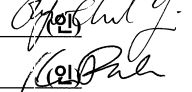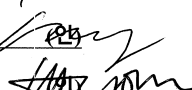
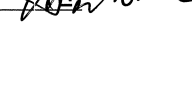지도교수 이 규 철

이 논문을 이학박사학위논문으로 제출함

2020년 07월

서울대학교 대학원

물리천문학부

송 민 호

송민호의 박사학위논문을 인준함

2020년 07월

위 원 장	홍 성 철	(인)
부 위 원 장	이 규 철	(인)
위 원	박 혜 윤	(인)
위 원	최 현 용	(인)
위 원	박 원 일	(인)

Abstract

Bio-medical applications using nanomaterials are an emerging research field that takes advantage of the properties of high material quality and small size for applications at the interface of biological cells and devices. Researchers have been studying about bio-medical applications. For this applications, the formation of interface with living things and devices is important. Moreover, the direct interface with cells is very important because the cells are the basic unit of the living things. The size of materials or devices should be nano/micro meter size to form the proper interface with cells because the size of cell is around from few hundreds nanometer to few hundreds micrometer. Among these bio-medical applications using nanomaterials, the optogenetics is a recently emerging new method to study and manipulate the behavior of neuronal cells with light. Recently, many papers about optogenetics applications were reported using light-emitting diodes.

Gallium nitride (GaN) is a promising material for fabrication of light-emitting diode because of its high free exciton binding energy, direct band gap property. Using this promising material advantage, GaN material can be used for this application. In particular, GaN is a well-known, non-toxic, biocompatible material with a high optical quality. In this reason, this GaN material is suitable for the recent trend for bio-medical applications. Here, this dissertation introduces bio-medical applications using GaN micro-/nanomaterials and GaN microrod LED fabrication for optogenetics application.

First, I discuss on laser emission from GaN microrods that were introduced into mammalian cells and the application of these microrods for cell labeling. GaN microrods were grown on graphene-coated SiO$_2$/Si substrates by metal-organic vapor-phase epitaxy. Microrods are easily detached from the substrates because of the weakness of the Van der Waals forces between GaN and graphene. The uptake of microrods into HeLa cells via endocytosis and viability after uptake was investigated. Normal cellular activities, including migration and division, were observed over two weeks in culture. Furthermore, photoluminescence spectra of the internalized microrods exhibited sharp laser emission peaks with a low lasing threshold of 270 kW/cm^2.

The following part demonstrate that the GaN microrod LEDs fabricated on the thin film LED for optogenerics application. The diameter of 200 nm nanorod LEDs also fabricated using dry and wet etching processes. The fabricated GaN microrod LEDs showed that enough output power for the optogenetics experiment. Moreover, the diameter of 200 nm nanorod LED showed higher power efficiency. The intracellular potential variations from the cells were also observed with patch clamp method after light illumination using GaN microrod LEDs.

Keywords: Gallium nitride, Light-emitting diode, Microrod, Intracellular laser. Optogenentics, Bio-medical application

Student Number: 2013-22989

Table of Contents

5

List of figures

8

9

15

with aging time ta = 100 s, unequivocally, match both the EA and TA MSDs from the experiment. (c) Individual TA MSD curves of the aging Lévy walk processes with the aging time t_a = 100 s. The thick blue curve is the average of the TA MSDs (gray curves). (d) Normalized amplitude scatter distributions $\phi(\xi)$ for the TA MSDs as a function of the rescaled variable $\xi = \overline{x^2}/\langle\overline{x^2}\rangle$. The experimental distribution from Figure C.2d (black circles) is compared with the theoretically expected distributions from the aging Lévy walk at three different aging times. (e) Aged probability density functions $P(x,\Delta t)$ of mRNP particles from the experiment and the aging Lévy walk simulations. (f) A fraction $q(t_a;T)$ of the trajectories showing no run at all in $[t_a, t_a + T]$ as a function of ta. Two theoretical curves for the aging Lévy walk were obtained from simulations with and without the uncertainty of ~1 μm (red and blue curves, respectively) for identifying the silent trajectories. Thus, the shaded region indicates the expected probabilities $q(t_a;T)$ in theory. The horizontal dashed line represents the experimental values for mRNP particles. It can be seen in the plot that the expected aging time is about t_a = 100 s………145

List of tables

Introduction

1

1.1. Motivation: Current research status in bio-medical applications using nano/micro inorganic materials

Bio-medical applications using inorganic nanomaterials have been attracted a great deal of attention because of their promising properties such as small size of materials and high material quality. Among these properties, the optical properties of materials have been preferred for bio-applications because the light can interact with biological cells with minimal damage. Many field was studied about optical properties of inorganic nano-/micromaterials such as drug delivery into cells using micro size magnet, optogenetic application, optical tweezer, intracellular lasers, and neural probes. The size of inorganic micro- and nanostructures also have good advantage for bio-medical applications because their size is small enough to form a direct interface with biological cells.

Cell labeling techniques play an essential role in cell imaging and individual cell tracking. In medical and biological science, the cell labeling is used for studying cell migration[1], differentiation[2], dynamic behavior of cells[3], and

the progression of many diseases including cancer cell metastasis[4]. Fluorescent dyes have been used for imaging cells or single cell tracking but their broad emission spectrum has been an obstacle in labeling large number of cells.[5-7] In addition, the low efficiency and photobleaching of organic materials still remains to be resloved.[7] To address these issues, a new form of approach using intracellular lasers have been introduced. In particular, inorganic optical materials have recently been introduced for intracellular laser application since they offer excellent lasing characteristics and chemical and mechanical stability.[8-11] For example, inorganic materials including CdS nanowires[10], AlGaP multi quantum well nanodisks[9], InGaAsP nanodisks[8] have been used for inorganic intracellular lasers exploiting their advantages. However, the toxicity of CdS and InGaAsP can be a problem for bio-application and the toxicity of AlGaInP is not still well known.[12] Meanwhile, GaN is a well-known non-toxic, biocompatible material[13,14] with a high refractive index and optical gain coefficient[15]. In this thesis, fabrications of GaN microrod lasers and their lasing characteristics were studied for intracellular laser applications.

Optogenetics is also an emerging technology based on introducing light-sensitive ionic channel into cells, and then using light to control ionic channel.[16,17] These light-sensitive ionic channel open the ionic channel when absorbing light of a specific wavelength. Depending on the function of the light-sensitive ionic channel, this enables us to manipulate migration, metabolism, or

electrical activity of cells. Optogenetics is a successful tool in neuroscience, where light-activated ion-channels are now widely used for controlling the intracellular potential of neuronal cells. To control this light-sensitive ionic channel, light sources that are spectrally matched to the activation spectrum of this light-sensitive ionic channel is required. At the early stage, most of optogenetics experiments have used arc lamps[18], lasers[19], or light-emitting diodes (LEDs)[20]. For the cultured cells, light is typically delivered through a microscope, and for the *in vivo* experiments, optical fibers were used for delivering the light to the target cells.[21] Although these methods are very promising, the spatial resolution and light illumination to large number of individual cells still remains to be solved.

1.2. Objective and approach

GaN is a promising material for fabrication of optoelectronic devices because of its high recombination rate, high carrier mobility, and stable material properties. Moreover, the superior biocompatibility of GaN material allow us to use this material for bio-medical applications. In this reason, this GaN material is suitable for the recent trend in bio-medical applications.

In this thesis, GaN micorords and micro LED pixel arrays for bio-medical applications are demonstrated using this high optical quality and biocompatibility. The high quality of GaN microrods grown on graphene films were used for intracellular laser application to label the cells. The GaN micro LED was also used

for optogenetics application using this strong light emission. The fabricated GaN micorod LED has high spatial resolution to stimulate cells with <500 nm micorod LED.

1.3. Outline

This thesis consists of 7 parts. Following by general introduction in chapter 1, chapter 2 reviews growth methods and for optogenetics application. In chapter 3, the detailed experimental set-ups and procedures, including growth, fabrication method of microrod LED for optogenetics application, and characterization methods, are described. Using high optical quality of GaN microrods grown on graphene films, the intracellular laser experiment for bio-application is described in chapter 4. The GaN mircrorod LED was fabricated for optogenetics application and the intracellular potential variation was induced using fabricated GaN mircrorod LED in chapter 5. Finally, chapter 6 presents the summaries of this thesis with suggestion for future works.

Literature Review

2

In this chapter, current research activities on bio-medical applications are reviewed. Especially, this chapter focus on the intracellular lasers for cell labeling and micro LED for optogenetics application. For the intracellular laser, the small lasers that are the gain medium and resonator itself are reviewed more in details. For the micro LED, recently studied micro LEDs with pixel arrays fabricated on the organic and inorganic materials are introduced.

2.1. Intracellular lasers using micro-/nano materials

Cell labeling techniques is widely used for the cell imaging and individual cell tracking.[22] In medical and biological science, cell labeling is used to study cell migration[1], differentiation[2], the dynamic behavior of cells4, and the progression of diseases, including the metastasis of cancer[4] (figure 2.1).

2.1.1 Intracellular lasers using organic materials

The first remarkable achievement for the intracellular laser was reported by Humar *et al.*.[23] As shown in the Figure 2.2a, they injected oil composed of

natural lipid droplet into the cells with fluorescent material. This microlaser was produced lasing signals from the cells via optical pumping and that is a gain medium and resonator itself. However, this method is not applicable for large number of cells because the oil should be injected using micro syringe. This injection method can damage the cell membrane and this is not appropriate for application on the large number of cells.

The first applicable intracellular laser that is a gain medium and resonator itself was reported using polymer bead (Figure 2.2b).[24] In this paper they used polystyrene divinylbenzene (PS-DVB) polymer bead for resonator and the gain medium was green fluorescent dye. The green fluorescent dye was doped into the microsphere PS-DVB. The reflective index of PS-DVB is 1.60. That value is higher than the reflective index in biological cells (n_{cell} ~ 1.375) so that this PS-DVB microsphere can act as whispering gallery mode (WGM) microsphere resonator inside cells. They used four different mammalian cells for the intracellular laser experiment. Interestingly, their small laser can be internalized into the cells without any injection, but the naturally internalized into cell via endocytosis due to the small volume of laser.
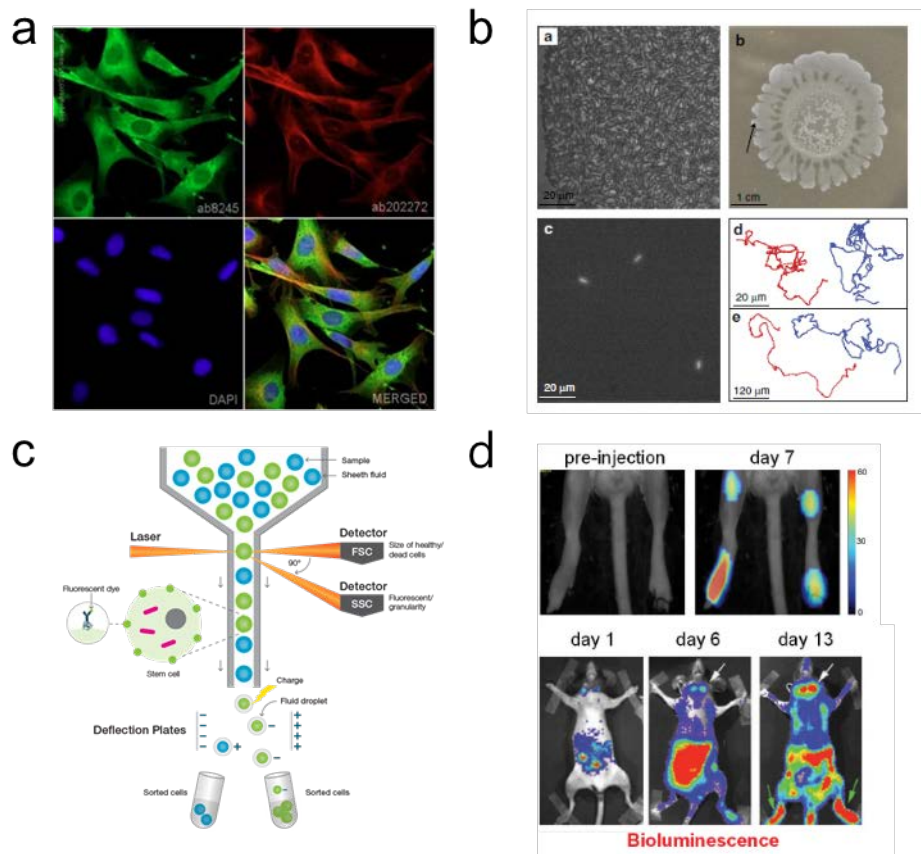
Figure 2.1. Widely used cell labeling techniques. (a) The fluorescent image from the stained cells. (b) Research for the cell migration. (c) Fluorescence-activated cell sorting (FACS) technique for cell sorting using fluorescent proteins or dyes. (d) Study about the cancer cell metastasis.
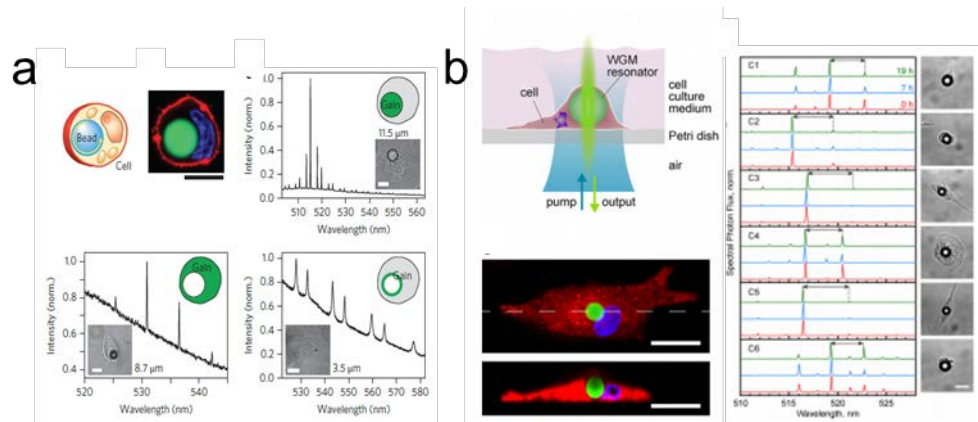
Figure 2.2. Intracellular lasers using organic materials. (a) Injected oil droplet with fluorescent dye was used for intracellular laser. (b) PS-DVB microsphere doped by fluorescent dye intracellular laser.

2.1.2 Intracellular lasers using inorganic materials

The intracellular laser using inorganic material was also reported by Fikouras *et al.*.[9] In this paper, the used aluminum gallium indium phosphide (AlGaInP) multi-quantum well nanodisks. To fabricate the nanodisks, they etched the thin film AlGaInP (Figure 2.3a). The internalization of nanodisks was also performed via endocytosis process. This shows good lasing properties with low lasing threshold because they used high optical quality of inorganic material. Recently, another inorganic intracellular laser was reported by Martino *et al.*.[8] They used indium gallium arsenide phosphide (InGaAsP) nanodisks (Figure 2.3b). This nanodisks also internalized into cells via endocytosis. They fabricated the emitted wavelength tunable intracellular lasers from 1,170 nm to 1,580 nm with and interval around 1nm using different diameter of nanodisks. Moreover, they also showed the practical application for cell tracking using a live mouse.
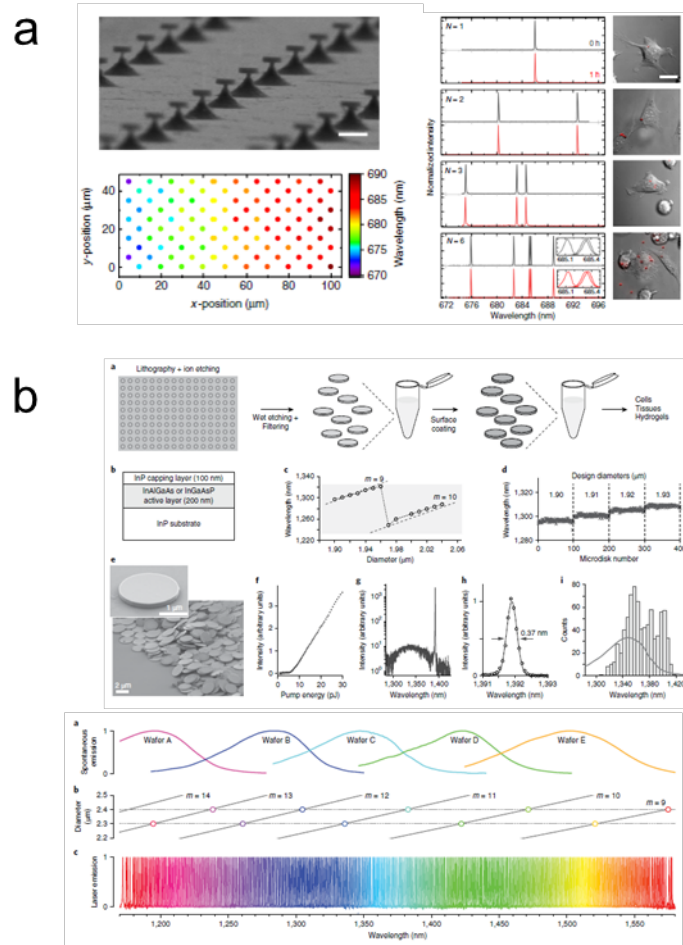
Figure 2.3. Intracellular lasers using inorganic materials. (a) Intracellular nanodisk lasers using AlGaInP material. (b) InGaAsP nanodisk intracellular lasers with different diameter for tuning the lasing peak wavelength.

2.2. Micro LEDs for optogenetics application.

Optogenetics has been attracted a great deal of attention because this method enables to control the neuronal cells using the light so that researchers study and manipulate the neuron cells with any minimal damage (Figure 2.4). In this review, an overview of recent advances in materials, devices, and current applications are introduced. At the initial stage of optogenetics applications, arc lamps[25], lasers[19], or light-emitting diodes (LEDs)[20] were used but, this wide area illumination is difficult to illuminate the specific position such as a single neuron cell.

2.2.1 Organic micro LEDs for optogenetics application.

The OLED pixel array with 6×9 mm^2 pixel size for optogenetics application was reported by Steude *et al.*.[26] This micro OLED was deposited on top of a complementary metal-oxide semiconductor (CMOS) backplane circuit (Figure 2.5). This small pixel size of OLED provides high spatial resolution to illuminate single neuronal cell. For this experiment, they used genetically engineered HEK cells that express a ChR2 mutant fused to enhanced yellow fluorescent protein; HEK-293$_R$ (ChR2-H134R-EYFP). They demonstrated current variation from the cells after light illumination using fabricated micro OLED pixel arrays. In this paper, the single cell stimulation was archived using high spatial

resolution. However, their low output power density of OLED (~1 W/m^2) could

produce small current variation (< 20 pA).
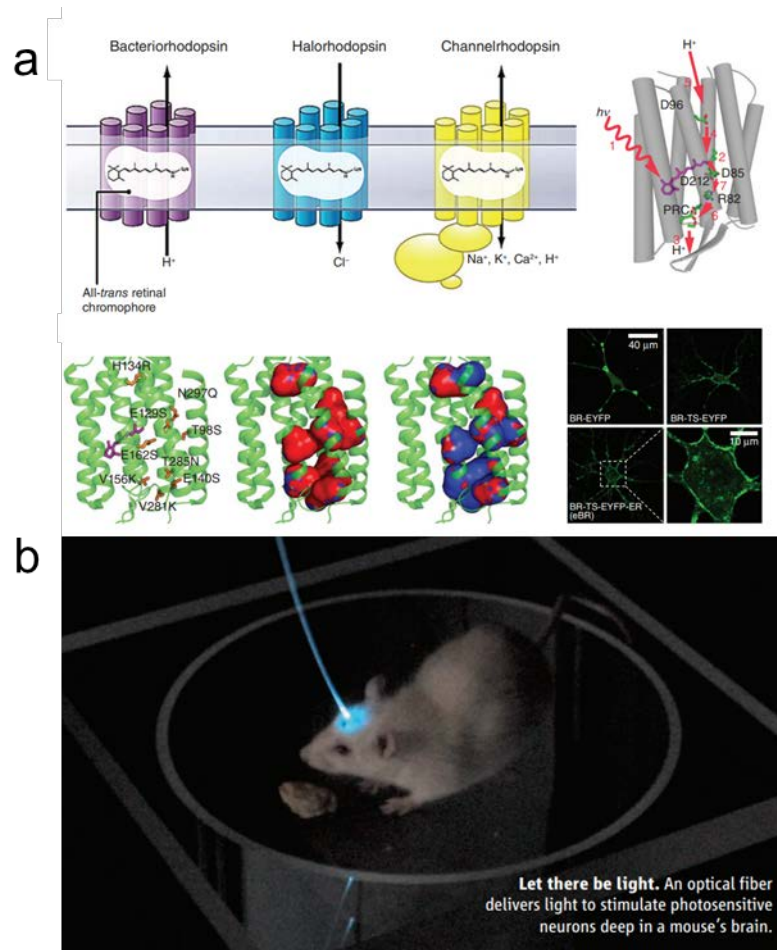
Figure 2.4. light-activated proteins for optogenetics applications and an *in vivo* application. (a) Various light-activated proteins for optogenetics application (b) An *in vivo* application using light-activated proteins
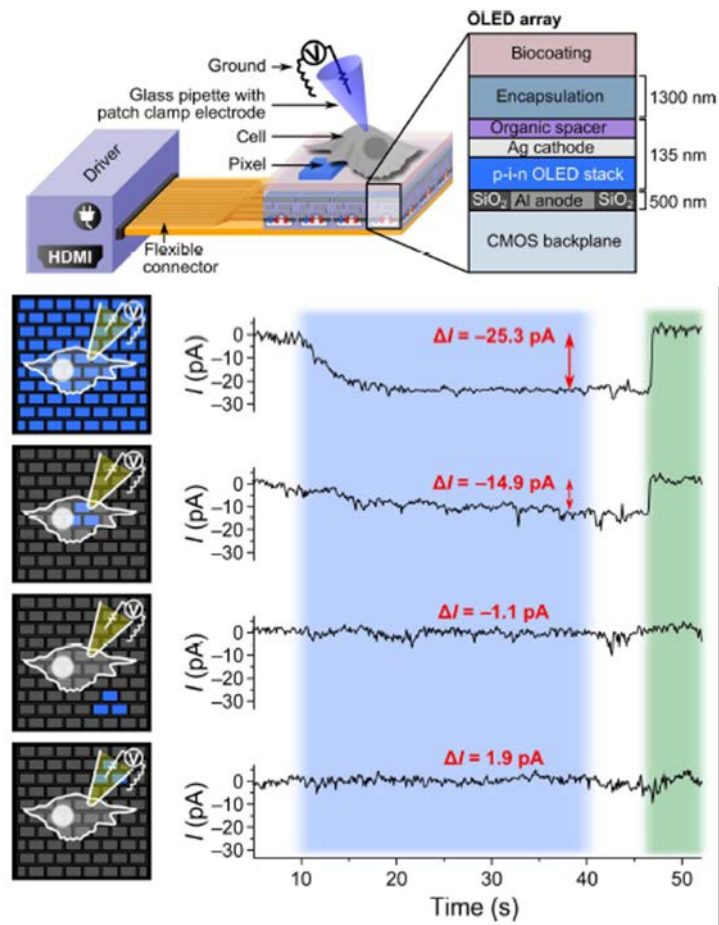
Figure 2.5. OLED pixel array for optopgenetics experiment. OLED

fabricated on the CMOS backplane circuit illuminated single neuronal

cell.

2.2.2. Inorganic micro LEDs for optogenetics application

To overcome this low power density and durability, the inorganic micro LED was fabricated for optogenetics application. The GaN is a very promising optoelectric material due to its high free exciton binding energy, direct band gap property and biocompatibility. Using this promising material advantage, GaN material was used for this application. Grossman *et al.*.[27] reported GaN micro LED array for optogenetics application (figure 2.6a). The GaN micro LED was integrated with CMOS control chip using flip-chip-bonding method providing independent control of each LED pixel. They demonstrated the neuron cell stimulation using this micro LED pixel array but its low spatial resolution (~50 µm) makes it difficult to stimulate single neuron cell. Recently, the Mao *et al.*[28] reported GaN micro LED array with $4 \times 4 \, \mu m^2$ pixel size for optogenetics application (figure 2.6b). The used passive matrix addressing method for this micro LED. In this paper, the Ca^+ indicator was used for sensing the neural signal.
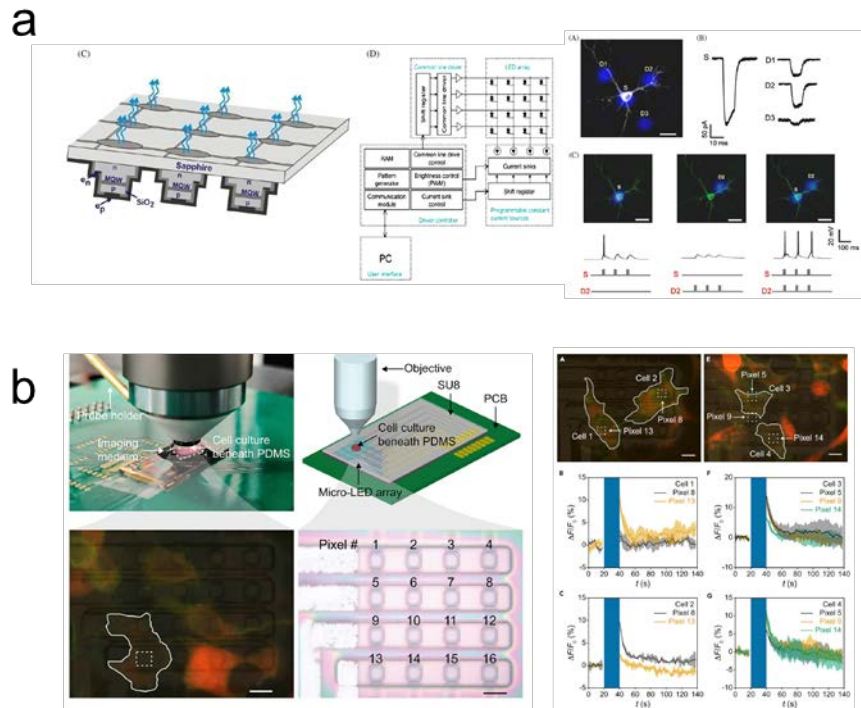
Figure 2.6. Inorganic LED pixel arrays for optopgenetics experiment. (a) GaN LED pixel array integrated with CMOS control chip using flip-chip-bonding method. (b) GaN micro LED array with 4×4 μm² pixel size with passive matrix addressing method for optogenetics application

Experimental methods

3

3.1. Metal-organic chemical vapor deposition system

This chapter describe apparatus and methods for ZnO nanotube growth. Catalyst-free metal-oragnic chemical vapor deposition (MOCVD) was employed for the growth of ZnO nanostructures, including nanotubes arrays. MOCVD method had been widely used for fabrication of the epitaxial growth of semiconductor materials on the substrates and the growth of 1D semiconducting nanostructure has been reported using MOCVD method.

3.1.1. Gas delivery system

Figure 3.1 shows gas delivery system of ZnO MOCVD. The gas delivery system consists of gas regulators (Tescom, 44-2263-241), mas flow control (MFC) controller (smtek, DFC4000), pneumatic gas manifold control card (Clippard Instrument Laboratory, No. EMC-08-24-30), and pneumatic valves connected with 1/4'' electro-polished 316-stainless steel (SS) tubing. The connections between SS tubes were made with SS welding fitting or SS gasket (Swagelok Inc., SS-4-VCR-2). The gas fluxes were controlled by individual MFCs (Tylan Co., FC-280S

Celerity, TN 280 or Mycrolis, FC- 280S). Individual delivery line pressures for MO source were kept around 300 Torr using metering valves (Swagelok, SS- 4BMG-VCR) and line pressure was measured by mini baratron pressure gauge (Setra Systems Inc., 225G-025P-A-D4-2C-06).
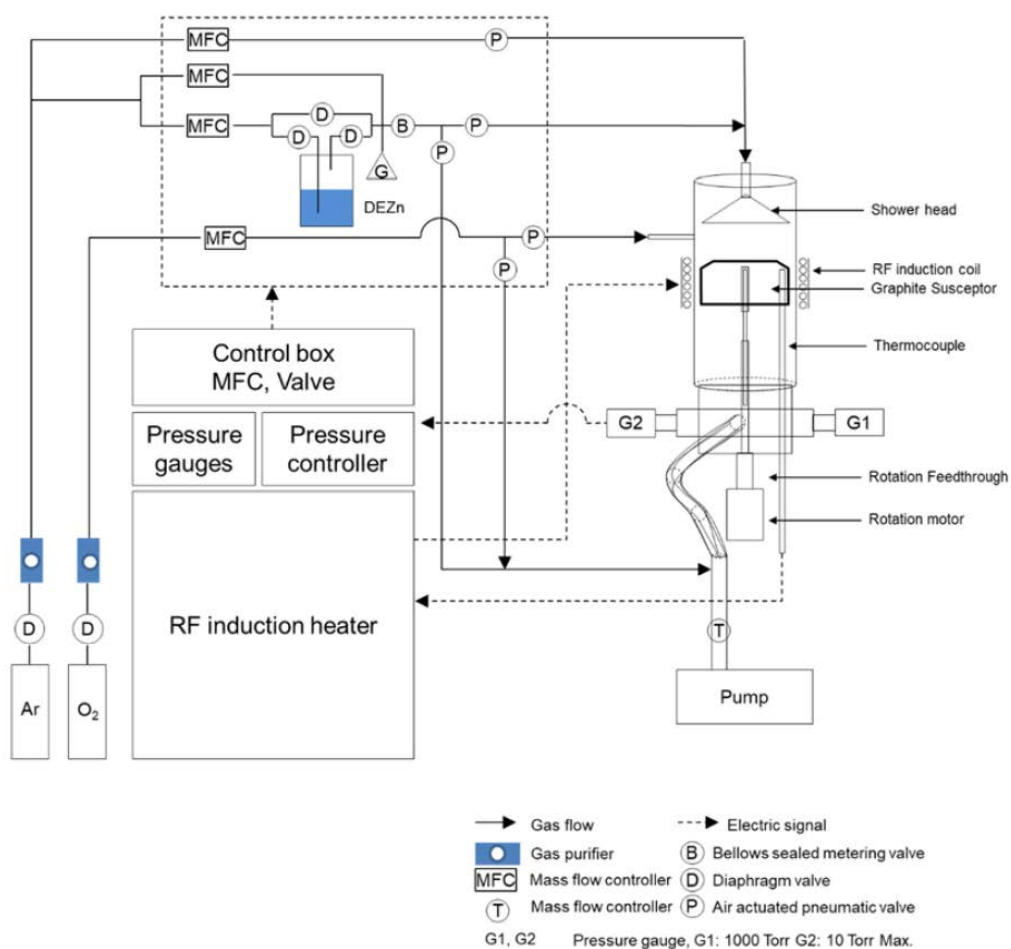
Figure 3.1. Gas Delivery system of ZnO MOCVD.

3.1.2. Growth chamber and substrate heating

Quartz reactor was used for the ZnO nanotube growth in MOCVD system, as shown in Figure 3.2. The ZnO chamber is a vertical type reactor and made of a fire polished tube quartz (material grade: GE-214), with 90 mm outer diameter, 86 mm inner diameter, and 300 mm length, and two 316SS ultra-torr fitting flanges on both ends. ZnO was grown in these chamber using susceptor and induction heating system. The susceptor is made of graphite coated with SiC and a 2 inch wafer size pocket is placed on the top of suscepter. The heating method is a radio frequency induction heater (Eltek, Inc., 15 kW for ZnO reactor). A copper coil was surrounded the quartz reactor with inter-distance of 10 mm, and temperature above 1000°C can be obtained in this chamber. The growth temperatures were controlled and measured by proportional-integral-derivative (PID) type temperature controller (Chino Co., KP1000) and thermocouples (Omega Co., K type), respectively. Additionally, the ZnO chamber contains showerhead and susceptor rotation parts which improve the uniformity of growth or composition over the entire 2 inch wafer-scale substrate. The showerheads are connected to the gas delivery system with using O-ring sealed ultra-torr fitting. O_2 gas line of ZnO chamber is separately connected to the chamber for preventing pre-reactions of ZnO.

38
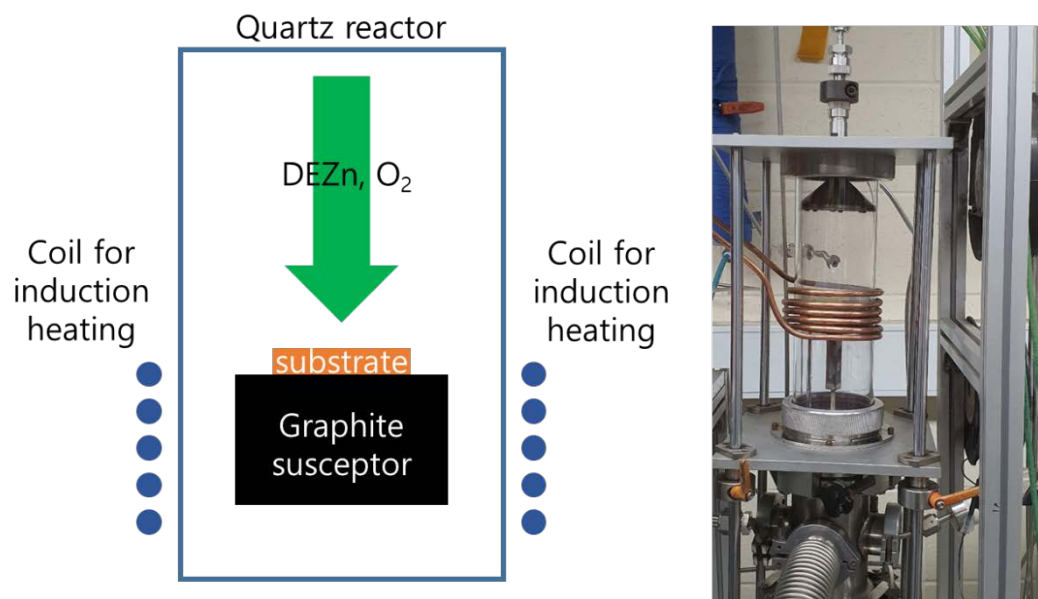
Figure 3.2. A schematic diagram and photograph of MOCVD chamber

3.1.3. Low pressure pumping and exhaust system

The by-product gas-phase chemicals were blown out through the exhaust tubing lines, which part corresponds to downstream of reactor, and were disposed by a scrubber system. The exhaust tubing lines at the vent line were connected to a series of vaccum component and the pressure was controlled by throttle valve (MKS Co., No. 253B) The manual angle valve, and a rotary pump (Kodivac, GHP-660K) are the last parts of vacuum line. The Baratron pressure gauge (MKS Co., No. 628B11TBE1B) is located at the bottom side of the reactor.

3.1.4. Gas and reactants

For ZnO growth, diethylzinc (DEZn) and O_2 (99.995 %) were used as reactants, and high purity Ar (99.999 %) was used as an ambient and carrier gas. Since the vapor pressure of metal-organic source was changed by the source temperature, metal-organic source kept constant temperature using water bath circulators (JEIO Tech, RW-1025G). Typical bath temperatures of DEZn were in the rage of -15°C to -10°C with different target growth rate. The details about gas flow rate for ZnO nanotube growth is in the Table 3.1.

Table 3.1 Gas and reactants for ZnO MOCVD

Reactant	Gas	Purity (%)	Vapor pressure	Company
DEZn		Electronic grade	$Log_{10}P=8.208\text{-}2109/T$	Epichem
O_2		99.995		
	Ar	99.9999		

P: Pressure (Torr), T: Temperature (K)

3.2. Growth techniques

The position and dimension controlled growth of 1D materials have been attracted tremendous attention due to their various applications. There was difficulty in position and morphology controlled growth of 1D inorganic materials. Moreover, most of inorganic material growth was performed on the single crystal substrate because of epitaxial growth. In this chapter, the position and morphology controlled 1D ZnO nanotube growth method are described. This controlled growth can give more advantage in many applications. And, the ZnO nanotubes grown on graphene films can easily be transferred onto arbitrary substrate because of weak an der Waals bonding of graphene layers.

3.2.1. ZnO nanotube growth on graphene films

Large-area, multi-layered graphene films were synthesized on Cu foil using the CVD method. The graphene films were transferred onto a Si wafer with 300-nm-thick SiO_2 layer. A SiO_2 layer was deposited onto the transferred CVD-graphene layers using PECVD (STS Co, LTD.) method as a growth mask. The thickness of the SiO_2 growth mask layer was typically 50 nm. After that, the oxide layer was annealed at 600°C in O_2 reach condition before the patterning process to reduce the number of defects in the as-deposited SiO_2 film because that defects can affect in selectivity for the selective growth of ZnO nanotubes. The patterns were formed using the electron beam lithography technique. The SiO_2 film was etched

42

using dry etching and wet etching using RIE and BOE, respectively. ZnO nanotubes were selectively grown on a graphene layer using catalyst free MOVPE.[29] Diethylzinc (DEZn) and high-purity O_2 (>99.995%) were used as reactants, and high-purity Ar (>99.999%) as the carrier gas. The flow rates of DEZn and O_2 were 15–30 and 70–90 sccm, respectively. During growth, Ar flowed into the quartz reactor through the bubbler with a DEZn bubbler temperature of –15°C to –10°C. To prevent premature reaction, the O_2 gas line was separated from the main gas manifold line. The reactor pressure was kept at 300 Torr during growth, and the temperature ranged from 600–700°C. The details for the growth parameters are in the Table 3.2.[29]

Table 3.2 Typical conditions for MOCVD growth for ZnO nanotube

Substrate temperature	600-700 °C
Reactor pressure	2.5-10 Torr
Vertical growth rate	5-8 µm/hr
O_2 flow rate	20-100 sccm
Ar flow rate	1500 sccm
DEZn flow rate	10-50 sccm
DEZn dilute flow rate	10-50 sccm
DEZn line pressure	300-400 Torr
DEZn bubbler Temperature	-15 to -10 °C

3.3. Optical characterization

For the characterization of grown GaN nano-/micro structures, a confocal micro-PL measurement system is required. In this chapter, the confocal micro- PL measurement system is explained.

3.3.1. Confocal micro-photoluminescence measurement

For the characterization of grown GaN nano-/micro structures, a confocal micro-PL measurement system was used. The measurement was performed at room temperature. Thes laser lights was focused using an objective lens, and the PL emissions from the sample were measured using a monochromator (Dongwoo, Monora 320i) with thermoelectric cooled charge-coupled device (CCD) (Andor, DU401A-UV). As laser sources, a HeCd laser (325 nm) and the third harmonic of Nd:YAG laser (355 nm, pulse width 6 ns, repetition rate 10 Hz) were used. For the study of PL emissions in UV region, an UV objective (OFR, x39) was used. The excitation position could be monitored simultaneously with the acquisition of PL spectrum using a beam splitter in the PL emission path. For a translation of sample position, a XY-motorized stage with a 2 µm resolution (Sigma Koki, SGSD26-50) was used.
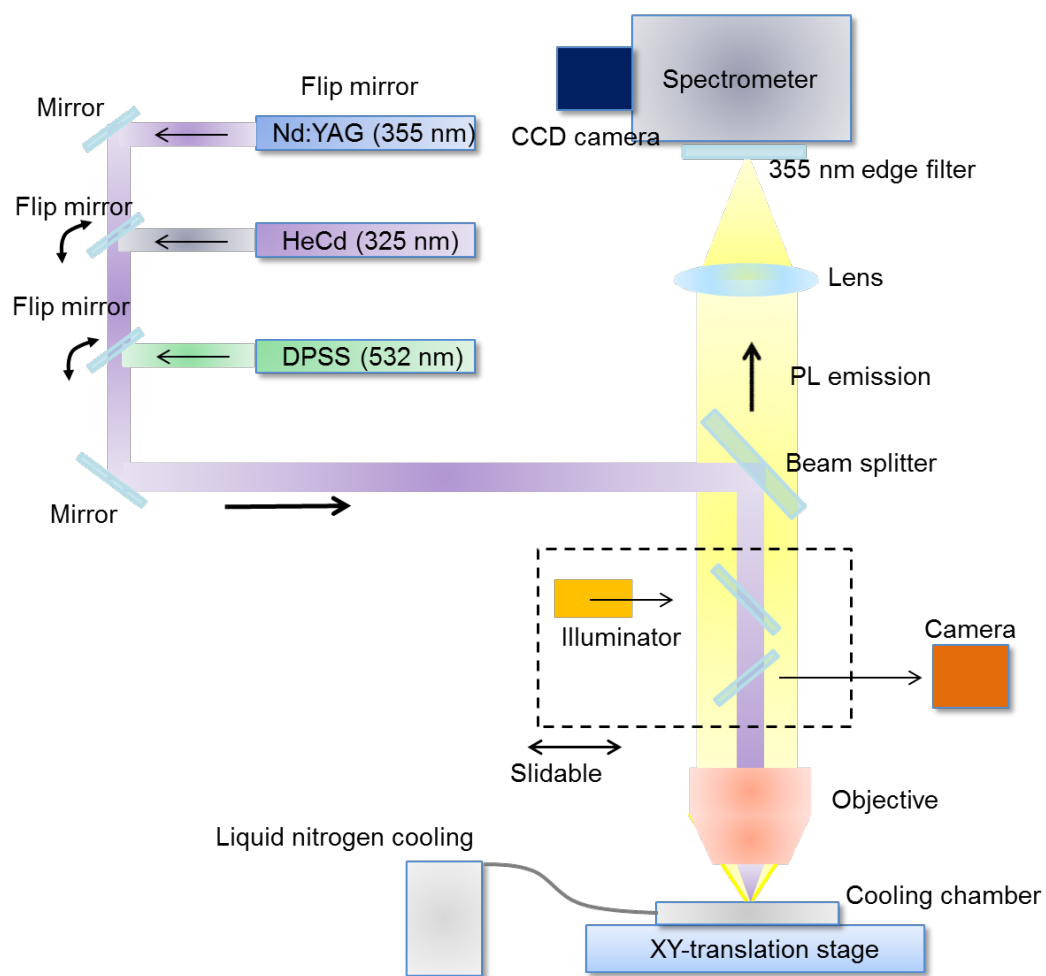
Figure 3.3. Schematic for micro-PL measurement

3.3.2. Photoluminescence measurement at high pumping density

For PL spectroscopy to measure the lasing signals from samples, the third harmonic of Nd:YAG laser (355 nm, pulse width 6 ns, repetition rate 10 Hz) was used and the laser intensity was controlled using neutral density filters (Thorlabs, NDK01). The other measurement setup is same as explained in chapter 3.3.1.

3.3.3. Electroluminescence measurement

The electroluminescence (EL) characteristics of the fabricated LEDs were measured using an EL measurement setup with a microscope (Carl Zeiss, Axioskop 2 MAT). For applying a voltage or current to LED devices, electrical source meter (Keithley 2400 or 2600) were used. The light emissions were collected by an objective lens and delivered into monochromator and CCD camera.
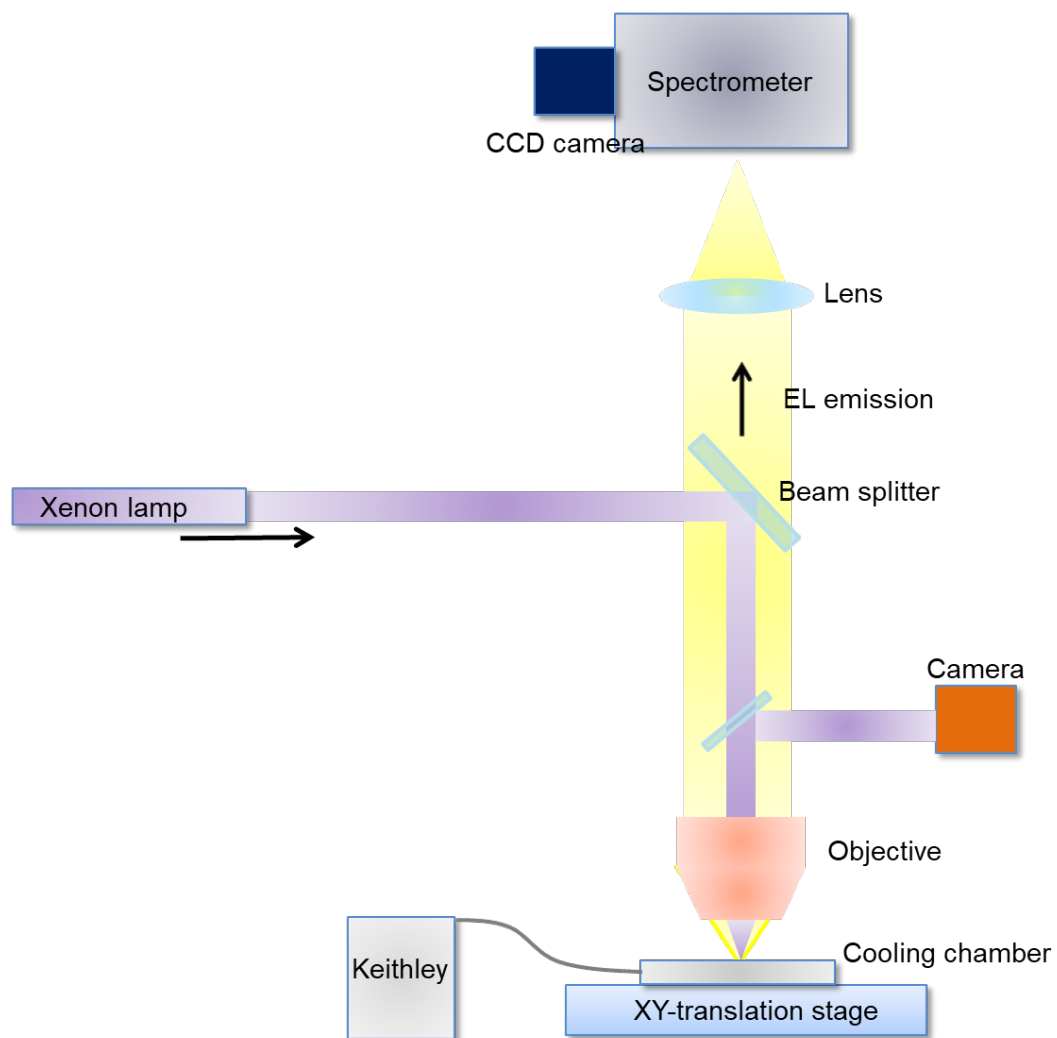
Figure 3.4. Schematic for EL measurement set-up.

3.4. Light-emitting diodes fabrication

3.4.1. Thin film light-emitting diode fabrication

To fabricate LED pixel arrays, GaN-based thin films composed of p-GaN, InGaN/GaN multiple quantum well structure, and n-GaN were prepared.

(1) p-contact formation: Before the p-contact metallization, the sample was dipped into BOE for 40s for removal of oxide layers. For metal contacts on p-GaN, Ni/Au (10/10 nm) bilayers were deposited on the top surface of p-GaN. After that, the thick Ti/Au (5 /60 nm) layers were deposited for endurance during successive dry etching process as shown in Figure 3.6. The metal contacts were annealed at 600°C in an air atmosphere for ohmic contact formation.

(2) Metal leads formation: The 300-nm-thick SiO2 layer were deposited using plasma-enhanced chemical vapor deposition for insulation. Metal leads (Ti/Au) were formed on SiO_2 layer using photolithography and metal deposition.

(3) Connection between leads and each LED pixels: Then the SiO_2 layer was selectively opened using reactive ion etching to allow current injection as shown in Figure 3.6. Finally, metal leads formed by photolithography were connected to each pixel to form addressable LED pixel arrays. For n-type contact, all pixels shared common eelctrode. Figure 3.7 shows light emissions from the fabricated LED pixels. Each pixel could show light illumination independently.
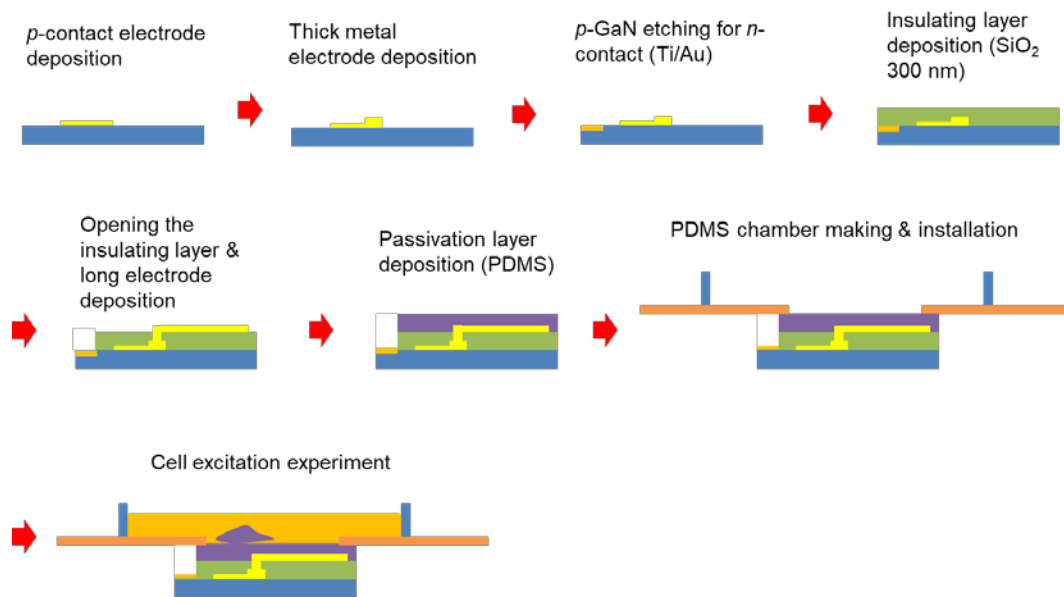
Figure 3.5. Schematic illustrations for fabrication of thin film LED pixel array.

Fabricated sample

a

2 cm

200 μm

b

50x50 μm² 20x20 μm² 10x10 μm²

200 μm

5x5 μm² 2x2 μm²
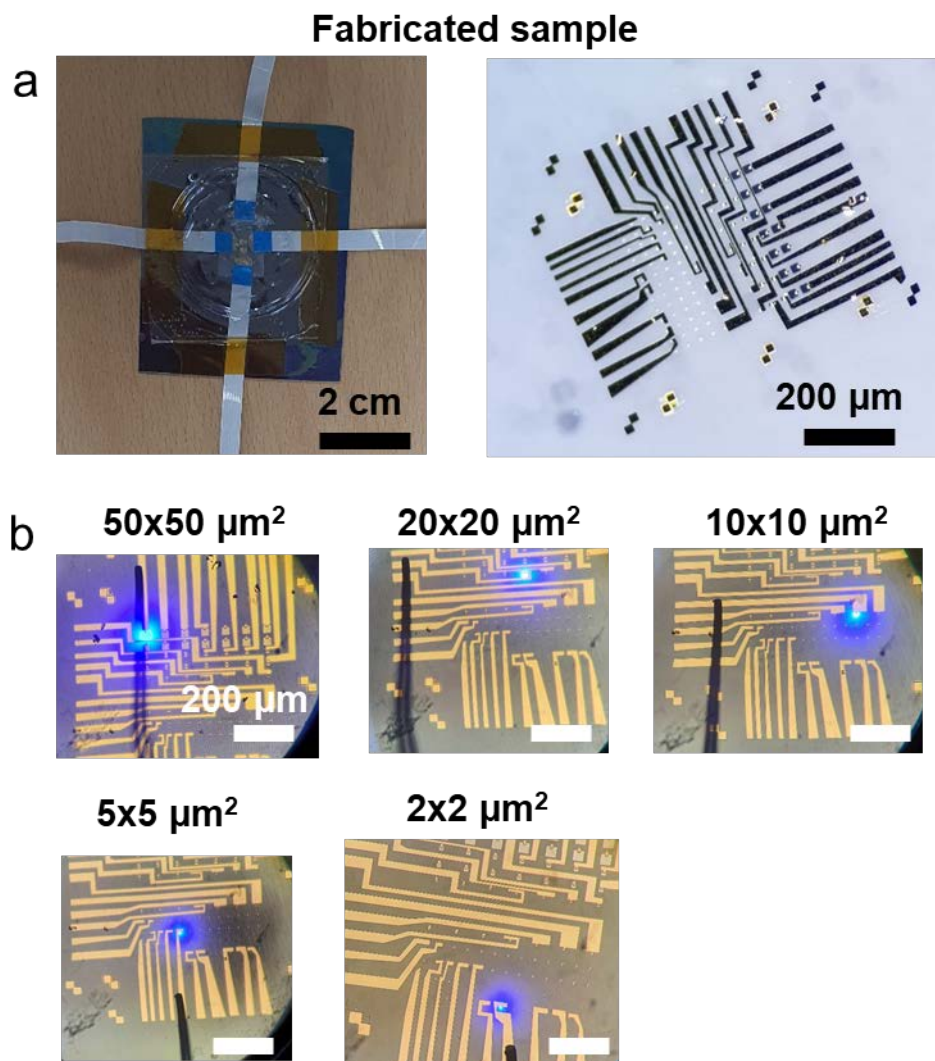
Figure 3.6. Optical microscope images for light illumination from all the pixels. (a) Fabricated sample images. (b) Light illumination from the LED pixels with 5 V applying voltage

Table 3.3 Typical conditions for fabrication of thin film GaN LED pixel array

Fabrication steps	Process conditions
1.1.metallization and metal contact annealing	Ni/Au 10/10 nm (variable), rapid thermal annealing, air, 760 Torr, 600°C for 5 min. ramping for 1 min
2.1. insulator layer coating	SiO_2 : the thickness is 300 nm using PECVD
2.2. insulator layer etching	Oxford P80+ RIE Ar 5 sccm, CF_4 45 sccm, 150W, 50 mTorr 6 min at room temperature
3.1. photolithography	contact size: 2x2−50x50 μm^2, AZ5214E
3.2. metallization	Ti/Au 10/80 nm (variable)

3.4.2. Micro- and nanostructure light-emitting diodes fabrication

To fabricate microrod LED pixel arrays, GaN-based thin films composed of p-GaN, InGaN/GaN multiple quantum well structure, and n-GaN were prepared.

(1) Dry etching of GaN microrod: To fabricate the GaN micorord LED, the thin film GaN should be etched via dry etching. The 80 nm of Ni etch mask was deposited using e-beam evaporator following the e-beam lithography technique. After deposition of Ni etch mask, the GaN thin film was etched using ICP-RIE (FR-IE20). The etching condition was 30 sccm, 5 sccm, 800 W, 100 W, and 5 mTorr for Cl_2 gas flow rate, BCl_3 flow rate, ICP power, RF power, and pressure, respectively. In this condition, the etching rate was around 500 nm/min.

(2) Wet etching of GaN: The shape of GaN was truncated cone shape after ICP-RIE. To fabricate the microrod LED, the additional wet etching process is needed. The GaN cone shape can be etched to the microrod shape using 1 molar concentration of KOH solution at room temperature. After 8 hrs etching, the shape of GaN microstructure was turn to the microrod shape due to the anisotropic wet etching of KOH.

(3) PI coating: PI insulating layer should be coated on the GaN microrod to separate p-contact and n-contact electrodes. The thickness of PI layer is around 7 µm at 4000 rpm coating with spin coater and the thickness of 1:1

diluted PI with N-Methyl-2-pyrrolidone is around 2 µm at 4000 rpm spin coating condition. Soft baking process was performed after PI coating with 120 °C during 1 min 30 sec. PI was cured using RTA after soft baking. The PI was cured at 300 °C with N_2 rich condition for 3 min.

(4) Metal contact: For metal contacts on p-GaN, Ni/Au bilayers were deposited on the top surface of p-GaN. These p-type metal contact areas were composed of two regions. For one region, semi-transparent Ni/Au (10/10 nm) layers were deposited for light transmission, and for the other region thick Ti/Au (5/60 nm) layers were deposited for endurance during successive dry etching process. For n-contact, the Ti/Au (10/90 nm) layer were deposited.

(5) Metal lead formation: Then 300 nm-thick SiO_2 layer were deposited using plasma-enhanced chemical vapor deposition for insulation. Metal leads (Ti/Au) were formed on SiO_2 layer using photolithography and metal deposition.

(6) Connection between leads and each LED pixels: Then the SiO_2 layer was selectively opened using reactive ion etching to allow current injection as shown in Figure 3.6. Finally, metal leads formed by photolithography were connected to each pixel to form addressable LED pixel arrays. For n-type

contact, all pixels shared common contact. Figure 3.7 shows light emissions

from the fabricated LED pixels. Each pixel could be operated independently.
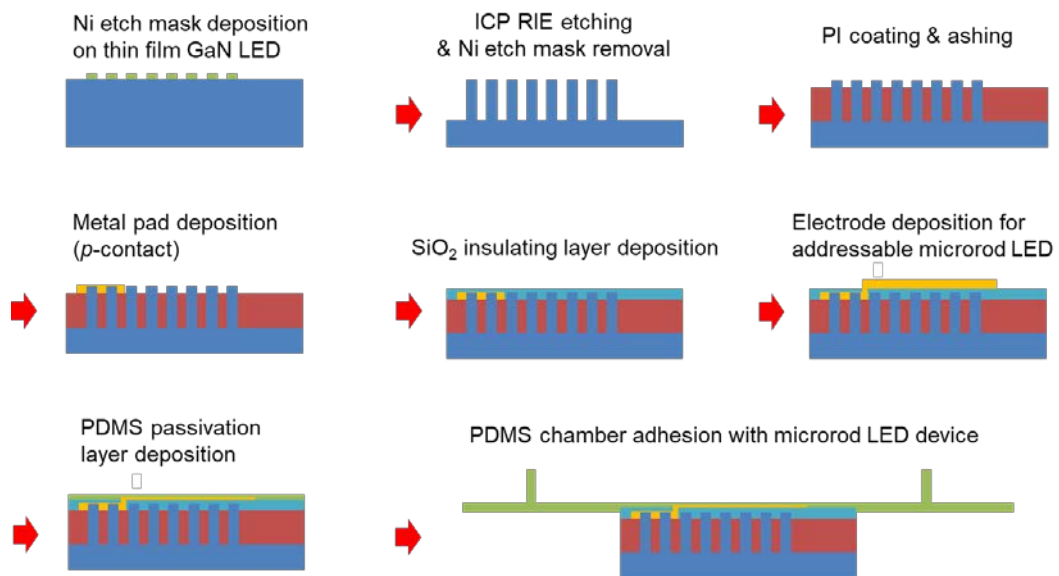
Figure 3.7. Schematic illustrations for fabrication of microrod LED pixel array.

Fabricated sample

Various pixel size
50x50 μm² = ~600 microrods
20x20 μm² = ~100 microrods
10x10 μm² = 20~25 microrods
5x5 μm² = 6~9 microrods
2x2 μm² = 1~3 microrods

50x50 μm²
~600 microrods

20x20 μm²
~100 microrods

10x10 μm²
20~25 microrods

5x5 μm²
6~9 microrods

2x2 μm²
1~3 microrods
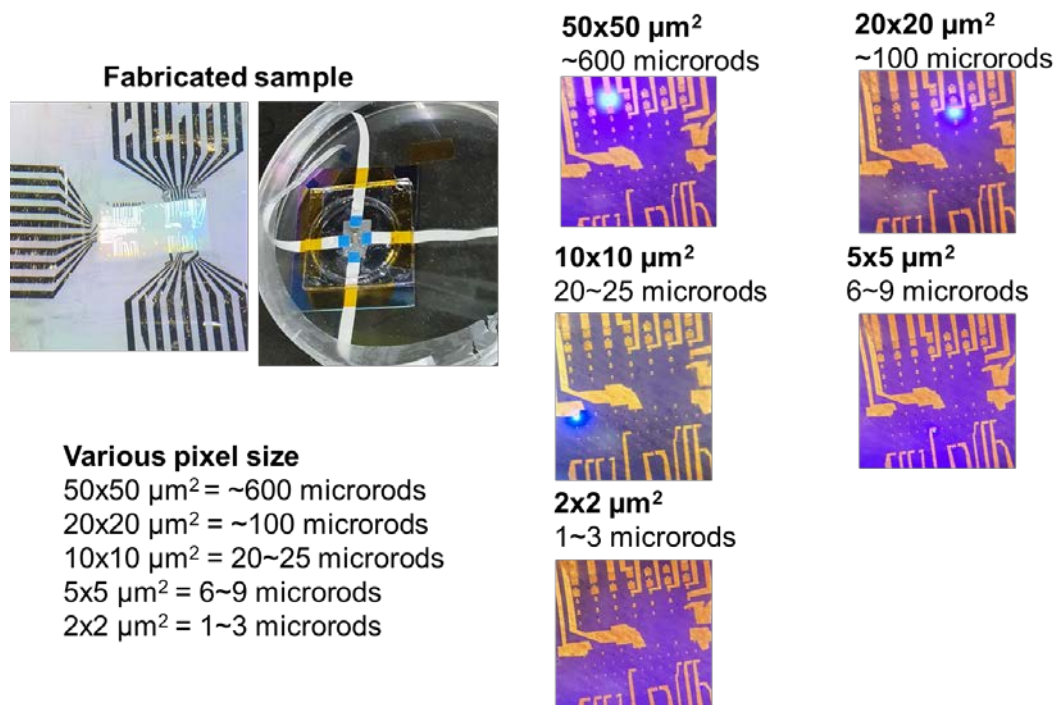
Figure 3.8. Optical microscope images for light illumination from microrod LED pixels. (a) Fabricated sample images. (b) Light illumination from the microrod LED pixels with 5 V applying voltage

57

Table 3.4. Conditions for fabrication of GaN microrod LED

Fabrication steps	Process conditions
1.1. Dry etching	30 sccm, 5 sccm, 800 W, 100 W, and 5 mTorr for Cl2 gas flow rate, BCl3 flow rate, ICP power, RF power, and pressure, respectively. Etching rate~500 nm/min using ICP-RIE (FR-IE20)
1.2. Wet etching	1 molar concentration of KOH for 8 hrs
2.1. insulator layer coating	for no-dilution polyimide: the thickness is ~10 μm after spin coating @4000 rpm
2.2. insulator layer etching	O_2 plasma ashing 3−15 min, 50mA, 100 mTorr
3.2. *e*-beam lithography for metal contact	contact size: 2x2−50x50 μm^2, PMMA 950K 5%, dose 400−900 $\mu C/cm^2$
3.3. metallization	Ni/Au 20/20 nm for *p*-contact Ti/Au 20/80 nm for *n*-contact

GaN microrod intracellular laser

4

4.1. Introduction

Cell labeling techniques play an essential role in cell imaging and individual cell tracking.[22] In medical and biological science, the cell labeling is used for studying cell migration[1], differentiation[2], dynamic behavior of cells[3], and the progression of many diseases including cancer cell metastasis[4]. Fluorescent dyes have been used for imaging cells or single cell tracking but their broad emission spectrum has been an obstacle in labeling large number of cells.[5-7] In addition, the low efficiency and photobleaching of organic materials still remains to be resloved.[7] To address these issues, a new form of approach using intracellular lasers have been introduced.[30] In particular, inorganic optical materials have recently been introduced for intracellular laser application since they offer excellent lasing characteristics and chemical and mechanical stability.[8-11] For example, inorganic materials including CdS nanowires[13], AlGaP multi quantum well nanodisks[9], InGaAsP nanodisks[8] have been used for inorganic intracellular lasers exploiting their advantages. However, the toxicity of CdS and InGaAsP can

59

be a problem for bio-application and the toxicity of AlGaInP is not still well known.[12] Meanwhile, GaN is a well-known non-toxic, biocompatible material[13,14] with a high refractive index and optical gain coefficient[15]. In this chapter, the fabrications of GaN microrod lasers and their lasing characteristics for intracellular laser applications are presented.

4.2. GaN microrod growth

The GaN microrods were grown on graphene films using metal-organic chemical vapor deposition (MOCVD), as shown in Figure 4.1a. The graphene films were grown on copper foil using chemical vapor deposition (CVD) and transferred onto 300 nm amorphous SiO_2 coated Si substrates. GaN microrods were grown on CVD grown graphene films using two step growth temperatures of 750−850 ℃ for 3 min and 950−1050 ℃ for 30 min, followed by substrate heating at 1100 ℃ for 10 min with hydrogen. The trimethyl-gallium (TMGa), ditertiarybutyl-silane (DTBSi), and ammonia (NH_3) were employed as reactants, and nitrogen was used as the carrier gas. The carrier gas flow rates that pass through metal organic sources bubbler of TMGa, DTBSi, and NH_3 were in the ranges of 15–30 sccm, 1–3 sccm, and 100–500 sccm, respectively. During the growth of the GaN microrods, the chamber pressure was maintained at 300 Torr. The 2 μm thickness of GaN buffer layer was grown to improve the vertical alignment of the microrods before the growth of the GaN microrods. GaN was grown on the surface of graphene with a uniform density of 10^7 cm^{-2}. The length and aspect ratio of GaN microrods

depended on the growth time. GaN microrods grown for 30 min exhibited a

diameter of 1.0 ± 0.3 μm and a length of 7.5 ± 1.0 μm (Figure 4.1b).
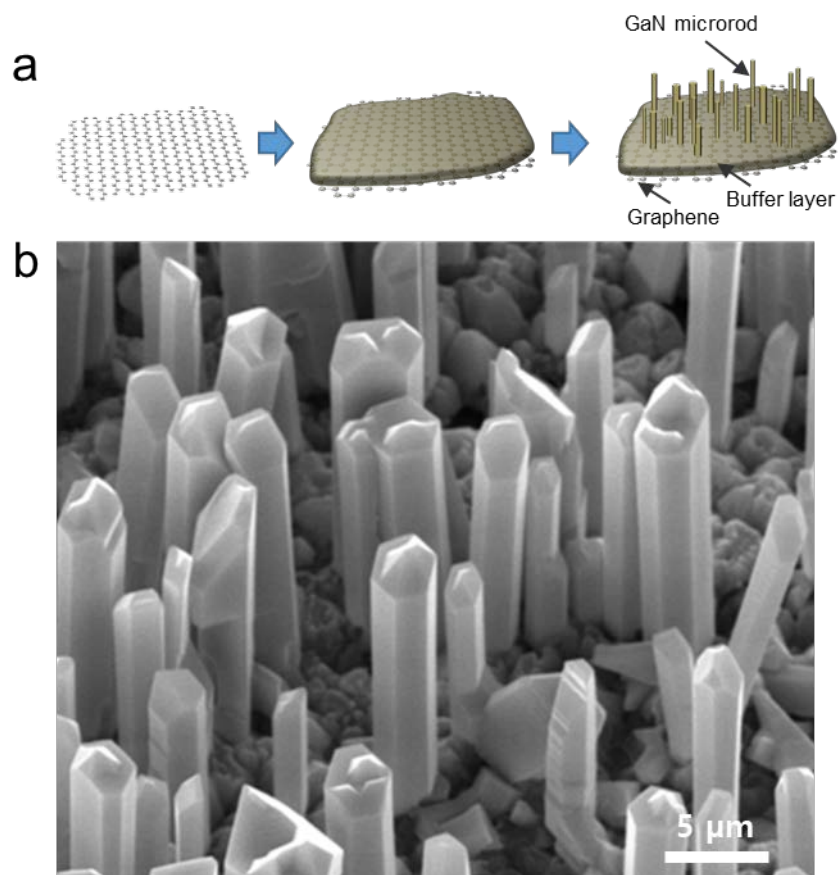
Figure 4.1. Growth of GaN microrod. (a) A schematic illustration for the GaN microrod growth on graphene layers. (b) An SEM image of GaN microrod on graphene layers

4.3. Sample preparation for intracellular laser experiment

The schematic illustrations for intracellular experimental methods are shown in Figure 4.2a. The GaN microrods were grown on graphene films using metal-organic vapor phase epitaxy (MOVPE) without employing any metal catalysts. A key benefit for using graphene is that the GaN microrods can be easily detached from the graphene substrate due to weak bonding between graphene and GaN. The GaN microrods were prepared using the bottom-up growth method without any additional etching processes. For the growth of the microrods, CVD grown graphene films synthesized on copper foil were first transferred onto a SiO$_2$/Si substrate. During the growth of the GaN microrods, the chamber pressure was maintained at 300 Torr. The 2 μm thickness of GaN buffer layer was grown to improve the vertical alignment of the microrods before the growth of the GaN microrods. GaN was grown on the surface of graphene with a uniform density of 10^7 cm^{-2}. GaN microrods were grown using catalyst-free metal-organic vapor-phase epitaxy. Details of GaN microrods growth are reported in elsewhere.[31] GaN microrods with a diameter of 1.5±1 μm and a length of 10±3 μm were employed for intracellular lasing experiments and a corresponding field-emission scanning electron microscopy (FESEM) image is in Figure 4.2b. The GaN microrods were internalized into the HeLa cells. To internalize into cells, the microrods were detached from the substrate using sonication in the cell culture media. Afterwards, the microrods immersed in the cell culture media were dispersed into the cell culture

dish where HeLa cells were cultured as a corresponding optical microscope (OM) image is shown in the Figure 4.2c. From the OM image, several bright spots due to GaN microrods were observed in the cell culture dish. After that, the microrods were internalized into the cells via endocytosis a process few hours after dispersing of GaN microrods. After internalization of GaN microrod into cells, the intracellular lasing characteristic signals were measured using confocal micro-photoluminescence (μ-PL) spectroscopy.
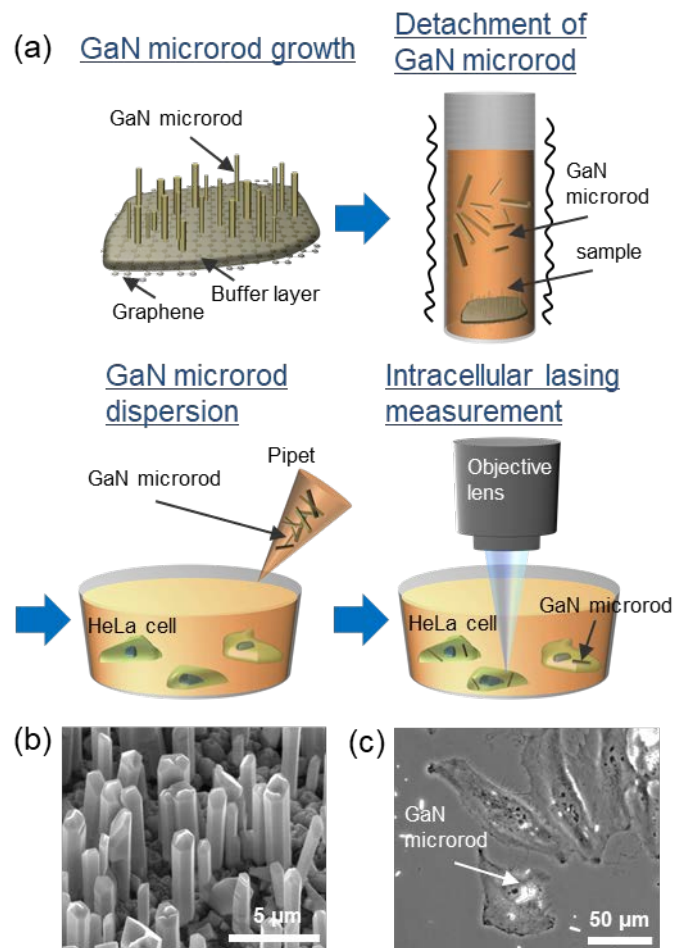
Figure 4.2. Experimental methods for intracellular laser experiment. (a) Schematic illustrations of procedure for intracellular GaN lasing measurement. (b) An FESEM image of GaN microrods grown on graphene films. (c) An OM image of HeLa cells with intracellular GaN microrods

4.4. Internalization of the GaN microrod into cells

The internalization of a microrod into a cell by endocytosis process was investigated before the lasing experiments. As shown in Figure 4.3a, the representative time-lapse images of the cells show that the HeLa cell was randomly migrating nearby a GaN microrod for the first few hours. After 5 hrs, the filopodia and lamellipodia of the cell suddenly extended to the microrod indicated by arrow in Figure 4.3a. Then the GaN microrod was fully internalized into the cell within few minutes. Since our GaN microrods have relatively small volumes, they could be easily internalized into the cells.[24] To confirm the internalization of GaN microrods, three-dimensional (3D) fluorescent microscope images of the cells were obtained using a confocal laser scanning microscope (CLSM). As shown in Figure 4.3b, the Z-projection and two cross-sectional images along the axial or coaxial direction show that the GaN microrods outlined with white dashed lines were clearly observed in the cytoplasm of cell. These results clearly indicate that the GaN microrods were totally enclosed by cytoplasm.
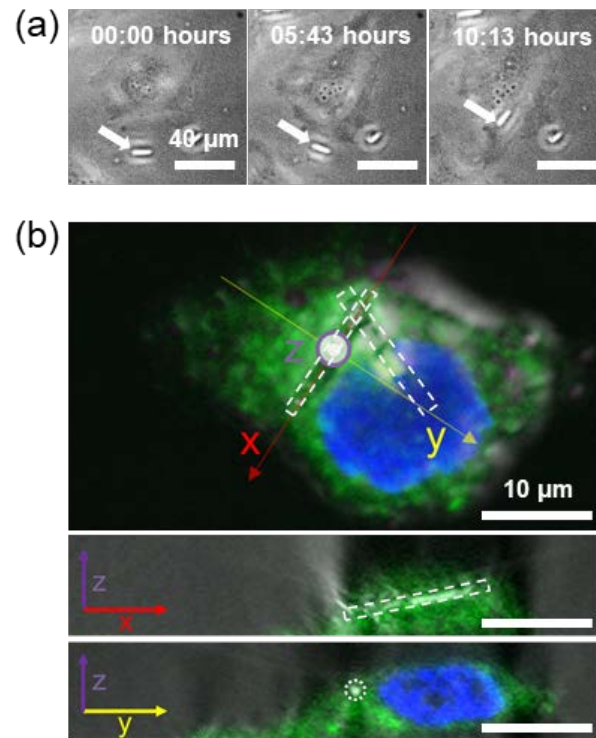
Figure 4.3. Cell viability checking. (a) Time lapse images of a HeLa cell showing normal cell division after internalization of a GaN microrod. The cell outlined in a red dashed line was divided into two cells outlined by orange and green lines. (b) Phase contrast and fluorescent OM images. Fluorescent images were obtained from Calcein AM and Ethidium homodimer-1 dyes.

4.5. Biocompatibility of GaN microrod

The cell activity was monitored using phase contrast optical microscopy (OM) in order to check the biocompatibility of GaN microrods with the cells. Figure 4.4a shows representative time-lapse images of migration and normal cell division after two weeks. The HeLa cell containing two GaN microrods migrated randomly in the Figure 4.4a. After 5 hours observation, they entered mitosis by appearing to fully round up. Then, daughter cells positioned in the adhesion pattern of the mother cell since mitotic spindles tend to be aligned with the long axis of the pre-mitotic mother cell. This cell division appearance is consistent with the normal cell division.[21] Even after cell division, the internalized microrods indicated by white arrows remained in one of the daughter cells.

The cell viability was also checked using a commercial cell viability assay kit. As shown in Figure 4.4b, calcein AM green-fluorescent image showed that all cells in the phase contrast OM image were stained with calcein AM dye, indicating that all cells were alive. In contrast, ethidium homodimer red-fluorescent signal could not be observed from the same cell culture dish, indicating that there was no dead cell. An overlapped image of phase contrast, calcein AM, and ethidium homodimer fluorescence unambiguously showed that all the cells were alive.
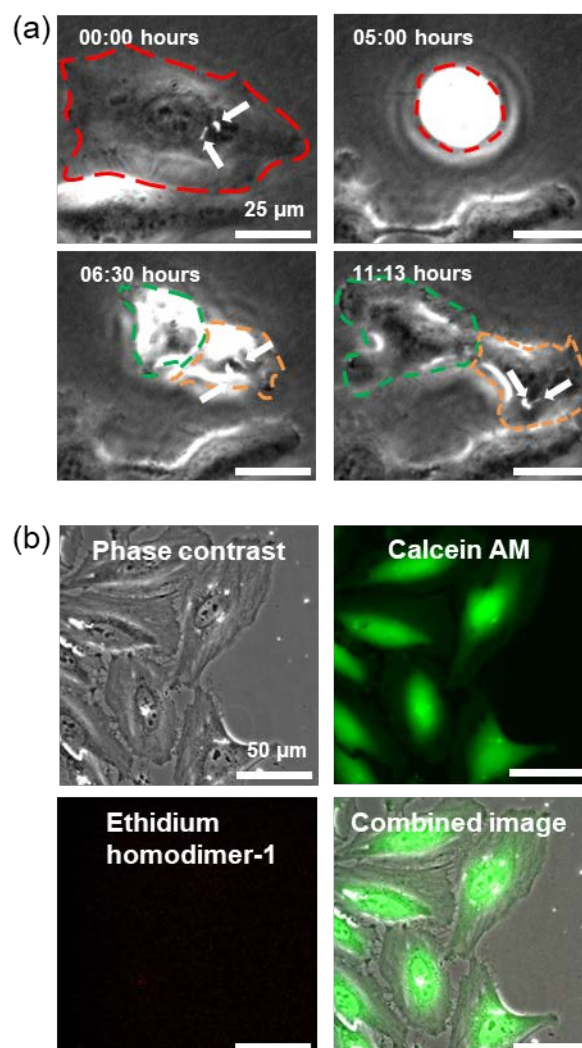
Figure 4.4. Cell viability checking. (a) Time lapse images of a HeLa cell showing normal cell division after internalization of a GaN microrod. The cell outlined in a red dashed line was divided into two cells outlined by orange and green lines. (b) Phase contrast and fluorescent OM images. Fluorescent images were obtained from Calcein AM and Ethidium homodimer-1 dyes.

4.6. Lasing characteristics of intracellular GaN microrod laser

PL spectra of GaN microrods internalized into cells were investigated at room temperature using a μ-PL system. Figure 4.5a shows PL spectra of the GaN microrods at several excitation power intensities of 20–720 kW/cm^2. The inset shows an OM image of the GaN microrods used for these measurements. Below the lasing threshold (I_{th}= 270 kW/cm^2), a broad emission centered at 370 nm was observed around the near-band-edge (NBE) emission of GaN. With increasing the excitation power intensity, additional sharp peaks appeared in the NBE emission spectra, eventually becoming the dominant feature in the PL spectra. From the mode spacing, the observed sharp peaks were attributed to Fabry-Perot type lasing along the axial direction of the microrods. According to previous report on GaN microrod lasing on SiO$_2$ substrate, the mode spacing for FP resonances is given by $\Delta\lambda \sim \frac{a}{L}$, where $\Delta\lambda$ is the mode spacing, L is the cavity length, and $a = 0.014$ μm^2 is the experimentally obtained values by linear fitting between $\Delta\lambda$ and $1/L$. For lasing spectra observed in Figure 4.5a, the $\Delta\lambda$ was around 1.11 nm, which was in good accordance with calculated the one using above relation with $L = 12.3$ μm for the length of the microrods. The lasing spectra from microrods were highly dependent on geometry of microrods. Basically, since the lasing oscillation is Fabry-Perot type, mode spacing was highly dependent on the length of the microrods. Additionally, it could be substantially dependent on the diameter, the

shape of cross-section, and the morphology of end facets of microrods. The diameters of the GaN microrods were much larger than the single mode diameter, thus many transverse waveguide modes could be excited simultaneously in a single microrod. The existence of multiple transverse modes and competition between them led to quite complicated lasing spectra with irregular mode spacings and intensity ratio as the PL spectrum in Figure 4.5a with an excitation power of 3.98 I_{th}.

Figure 4.5b shows the plot of integrated PL intensity versus the excitation pumping intensity. At low excitation power below the threshold, the slope was 3.7, but it increased to 10.4 above the lasing threshold. The threshold value of 270 kW/cm^2 was similar to those of high-quality GaN micro- and nanostructures grown on single crystal substrates[32-34], demonstrating that the GaN microrods grown on graphene films are of high optical quality. Additionally, due to the relatively high refractive index of GaN microrods (n_{GaN} = 2.6)[35], the lasing threshold was low in the intracellular conditions (n_{cell} = 1.36)[36]. The threshold value was also comparable with the previously reported one observed from intracellular laser using a microsphere.[24] Considering two orders of magnitude smaller volume of the GaN microrod and the comparable value of the lasing threshold, GaN microrods can be the better candidate for intracellular laser application.

The lasing characteristics was investigated for the intracellular GaN microrod laser depending on its geometry for cell-labelling. Figures 4.6a and b show OM images of cells with internalized microrods and corresponding lasing spectra. The lasing spectra from different intracellular microrods are clearly distinguishable based on their different center peak wavelength, the different mode spacings, and relative PL intensities between modes. In other words, individual microrods had their own proper lasing spectra enabling one to distinguish them each other, which can be used for cell labelling.

After the lasing measurement, cell viability was tested with commercial cell viability assay kits. While the cells were exposed to the focused laser beam with 10 mJ/cm^2 for 2 sec, the cells were alive. Additionally, the cell nucleus was less exposed from focused laser beam since the position of the GaN microrods was usually distant from the cell nucleus.[30,37]
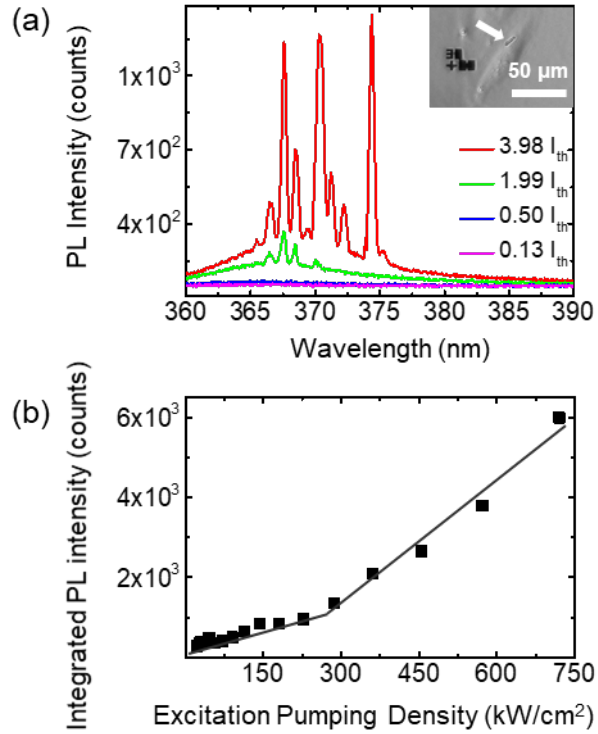
Figure 4.5. Characteristics of intracellular GaN microrod laser. (a) PL spectra measured at different optical pumping powers. The inset shows an OM image of an intracellular microrods used for the measurement. (b) Plot of output PL intensity versus input excitation power.
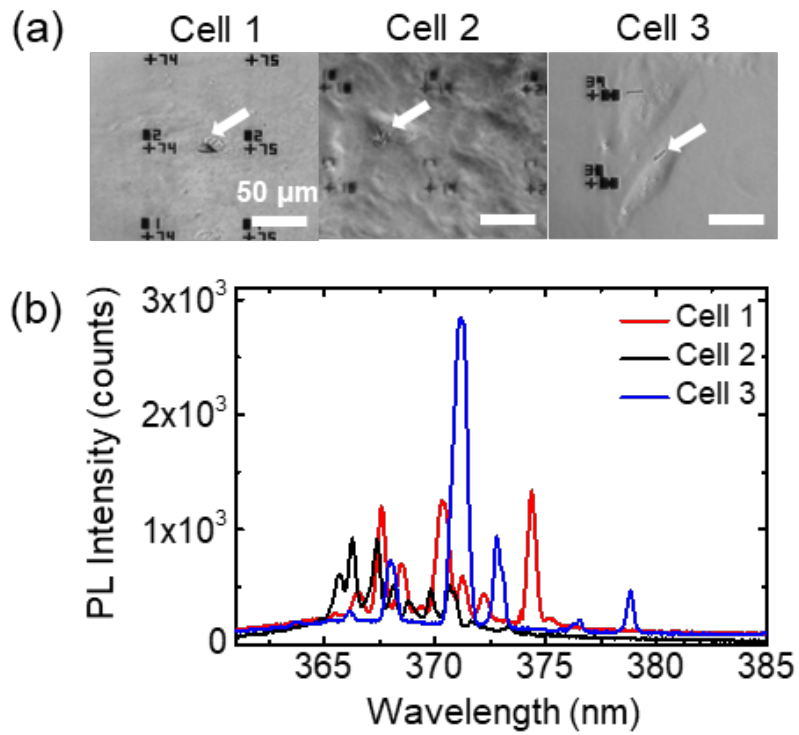
Figure 4.6. Lasing spectra from different intracellular microrod lasers in living cells. (a) OM images of cells containing GaN microrods. The microrods are indicated by white arrows. (b) Lasing spectra obtained from the intracellular microrods shown in (a).

4.7. Summary

In summary, we fabricated GaN microrod intracellular lasers for cell labelling applications. The GaN microrods grown on graphene films using MOVPE exhibited excellent lasing characteristics. The use of graphene as the substrate enabled to detach the GaN microrods very easily from the substrate and be dispersed into a solution for their internalization into cells. The relatively small volume and high aspect ratio of GaN microrods allowed easy internalization into the cells without any injection. Excellent lasing signals were observed even in the intracellular condition due to high optical quality and high refractive index of GaN microrods. We believe that the intracellular GaN microrod lasers can be used for a cell labelling and tracking application.

GaN thin film and microrod LED for optogenetics

5

5.1. Introduction

Optogenetics is an emerging technology based on introducing light-sensitive ionic channel into cells, and then using light to control ionic channel.[16] These light-sensitive ionic channel open the ionic channel when absorbing light of a specific wavelength. Depending on the function of the light-sensitive ionic channel, this enables us to manipulate migration, metabolism, or electrical activity of cells. Optogenetics is a successful tool in neuroscience, where light-activated ion-channels are now widely used for controlling the intracellular potential of neuronal cells. To control this light-sensitive ionic channel, light sources that are spectrally matched to the activation spectrum of this light-sensitive ionic channel is required. At the early stage, most of optogenetics experiments have used arc lamps[25] and light-emitting diodes (LEDs)[20]. For the cultured cells, light is typically delivered through a microscope, and for the *in vivo* experiments, optical fibers were used for delivering the light to the target cells[38]. Although these methods are very promising, the spatial resolution and light illumination to large

76

number of individual cells still remains to be solved. In this chapter, microrod GaN
LED arrays was fabricated for an optogenetics application.

5.2. Fabrication of microrod LED

To fabricate microrod LED pixel arrays, GaN-based thin films composed
of p-GaN, InGaN/GaN multiple quantum well structure, and n-GaN were prepared.
The details in fabrication process for GaN microrod LED is explained at the Figure
5.1 and bellows.

(1) Dry etching of GaN microrod: To fabricate the GaN micorord LED, the thin
film GaN should be etched via dry etching. The 80 nm of Ni etch mask was
deposited using e-beam evaporator following the e-beam lithography
technique. After deposition of Ni etch mask, the GaN thin film was etched
using ICP-RIE (FR-IE20). The etching condition was 30 sccm, 5 sccm, 800
W, 100 W, and 5 mTorr for Cl_2 gas flow rate, BCl_3 flow rate, ICP power,
RF power, and pressure, respectively. In this condition, the etching rate was
around 500 nm/min.

(2) Wet etching of GaN: The shape of GaN was truncated cone shape after ICP-
RIE. To fabricate the microrod LED, the additional wet etching process is
needed. The GaN cone shape can be etched to the microrod shape using 1
molar concentration of KOH solution at room temperature. After 8 hrs

etching, the shape of GaN microstructure was turn to the microrod shape due to the anisotropic wet etching of KOH (Figure 5.2).

(3) PI coating: PI insulating layer should be coated on the GaN microrod to separate p-contact and n-contact electrodes. The thickness of PI layer is around 7 µm at 4000 rpm coating with spin coater and the thickness of 1:1 diluted PI with N-Methyl-2-pyrrolidone is around 2 µm at 4000 rpm spin coating condition. Soft baking process was performed after PI coating with 120 °C during 1 min 30 sec. PI was cured using RTA after soft baking. The PI was cured at 300 °C with N_2 rich condition for 3 min.

(4) Metal contact: Before metal contact, the PI layer was exposed using O2 plasma ashing (Figure 5.3). For metal contacts on p-GaN, Ni/Au bilayers were deposited on the top surface of p-GaN. These p-type metal contact areas were composed of two regions. For one region, semi-transparent Ni/Au (10/10 nm) layers were deposited for light transmission, and for the other region thick Ti/Au (5/60 nm) layers were deposited for endurance during successive dry etching process. For n-contact, the Ti/Au (10/90 nm) layer were deposited.

(5) Metal lead formation: Then 300 nm-thick SiO_2 layer were deposited using plasma-enhanced chemical vapor deposition for insulation. Metal leads

(Ti/Au) were formed on SiO_2 layer using photolithography and metal deposition.

(6) Connection between leads and each LED pixels: Then the SiO_2 layer was selectively opened using reactive ion etching to allow current injection as shown in Figure 3.6. Finally, metal leads formed by photolithography were connected to each pixel to form addressable LED pixel arrays. For n-type contact, all pixels shared common contact.

Figure 5.1. Schematics for fabrication of GaN microrod LED.
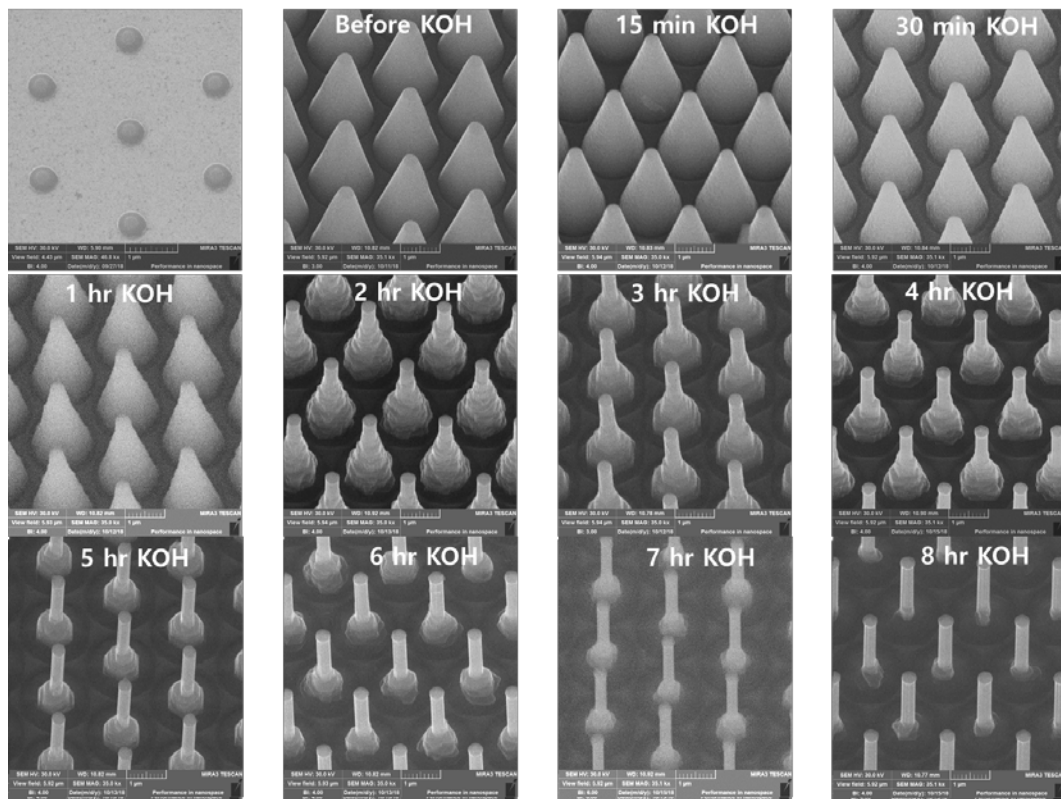
Figure 5.2. FE-SEM images after KOH wet etching condition study.

The shape of GaN microstructure was turn to the microrod shape due to

the anisotropic wet etching of KOH.
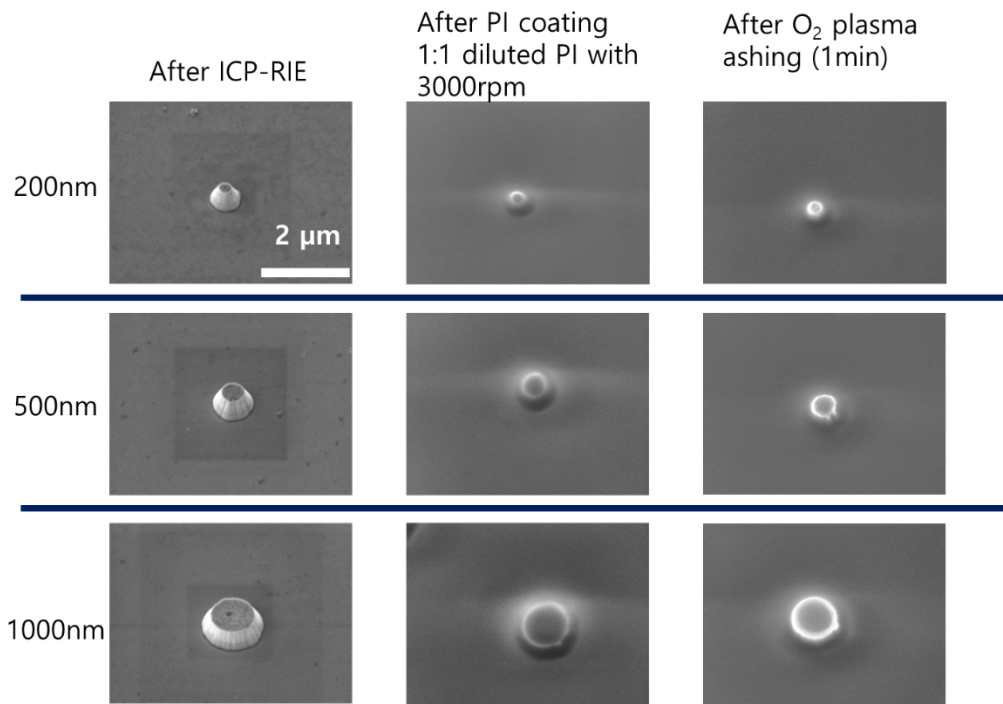
Figure 5.3. FESEM images after PI after coating and ashing. PI coating and ahsing condition study was performed with different diameter GaN microrods. After 1 min O_2 ashing, the top side of GaN microrod was exposed.

5.3. EL characteristics of microrod LEDs

The EL characteristics of the fabricated microrod LEDs were investigated using EL spectroscopy. Figure 5.4 shows I–V characteristics and OM images about different diameter of microrod LEDs. The I–V characteristic curve exhibits a good rectifying behavior but the current density was increased according to the decreasing diameter of GaN microrod LED. Presumably, the increased current density through a smaller nanopillar device is attributed to the enhanced radiative efficiency due to the reduction of the quantum-confined Stark effect (QCSE). Figure 5.5 shows the room temperature EL spectra and corresponding EL images of the LED at various applied voltage levels of 2.5, 3, 3.5, 4, 4.5, 5, 5.5, 6, 7, 8, 9, and 10 V. The EL spectra and LED light emission images show an increase of emission intensity with the applied voltage level increase. Additionally, as the applied voltage level increased from 2.5 to 10 V, the dominant EL peak slightly shifted to low wave length, i.e., blue shift.
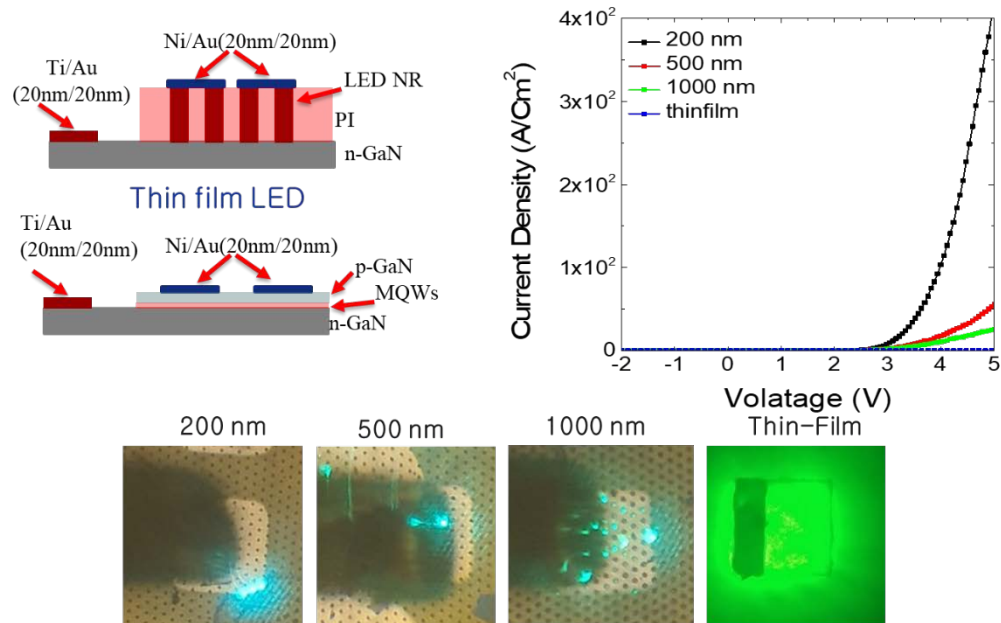
Figure 5.4. I–V characteristics and OM images of different diameter GaN microrod LEDs. The I–V characteristic curve exhibits a good rectifying behavior and the current density was increased according to the decreasing diameter of GaN microrod LED. The OM images for the light illumination were obtained at 5 V of applying voltage.
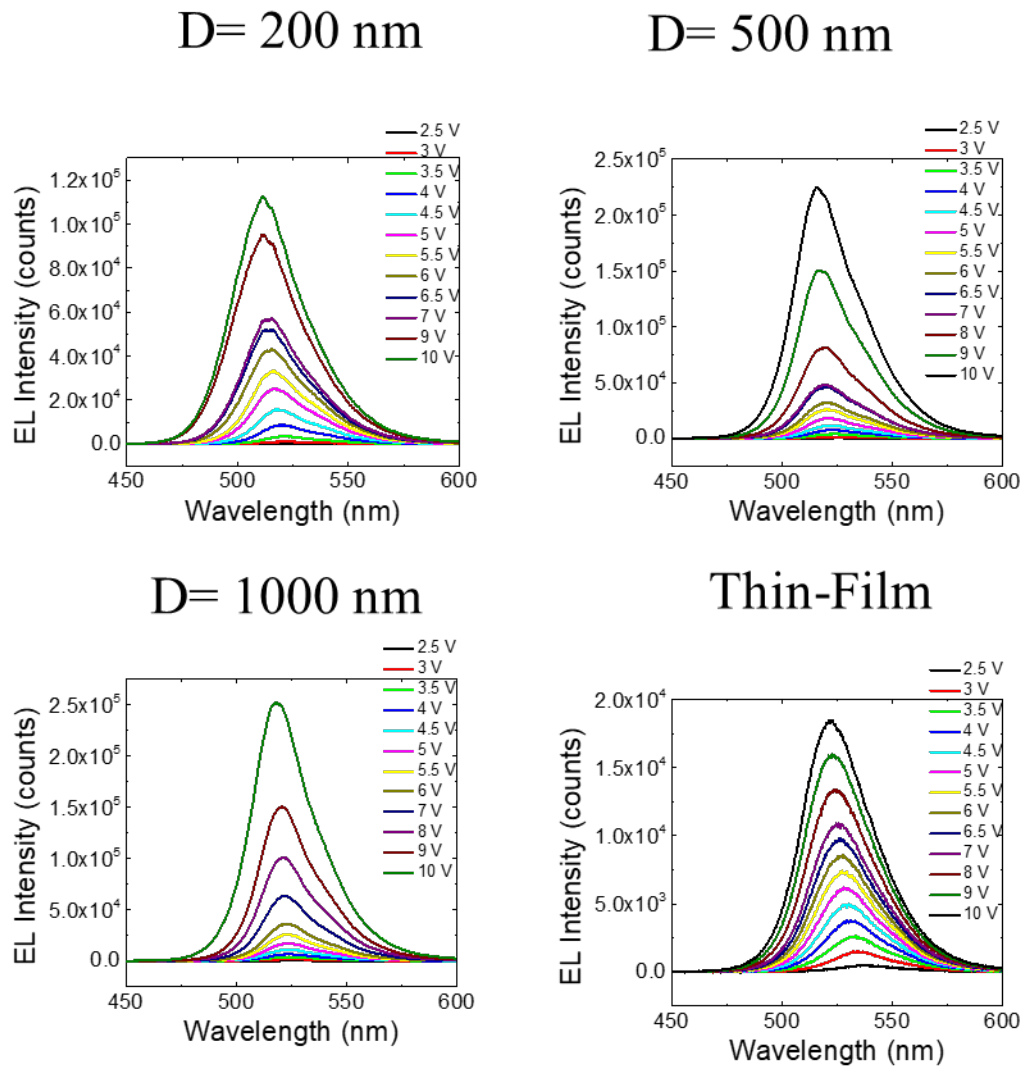
Figure 5.5. PL spectra from different diameter GaN microrod LEDs

Room temperature EL spectra of the LED from various applied voltage

levels.

5.3.1 EL peak shift in microrod LEDs

To investigate the EL peak shift, we plot the peak wavelength according to the applying current density as shown in the Figure 5.6. The current density was calculated from the data in Figure 5.6. This blue shift can be explained in terms of both a band filling effect of the localized energy states and a screening effect by the internal polarization electric field, i.e., QCSE, typically observed in LEDs with GaN/In$_{1-x}$Ga$_x$N MQW structures grown on a polar surface of GaN(0001). LED devices can become hot because applying current produce heat. In this case, the EL peak position must show a red shift with increasing current density. However, the EL emission peak position was blue-shifted with increasing current levels. The blue shift indicates that the device temperature was not high enough to cause the remarkable red-shift because the drive currents in these experiments were much lower than those used for conventional high-power LEDs. The blue shift was dominant in the thin film LED and large diameter of micro LEDs rather than small size microrod LED. Presumably, the more strain relaxation can be in the small diameter of nano/microrod LED.

a	200 nm	500 nm	1000 nm	Thin film
FWHM/2 shift (nm)	-1.5	-2.3	-2.8	-14.5
Peak shift (nm)	-2.3	-4.6	-4.3	-16
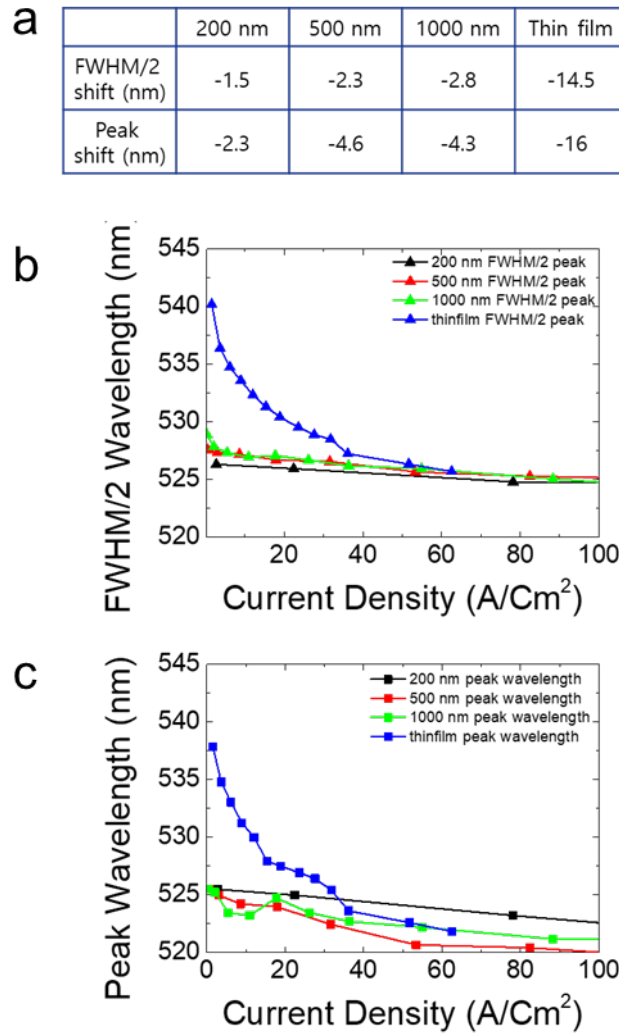
Figure 5.6. EL peak shift according to different applying current density. (a) The maximum peak shift of dominant main peak and FWHM/2 peak according to different applying current. EL peak shift plot from different size of GaN micro LED with FWHM/2 peak (b) and dominant main peak (c).

5.3.2 Power efficiency of microrod LEDs

The power efficiency was also investigated. Figure 5.7 shows that the output power density according to the input power density. The output power was measured by photodiode. The power efficiency was increased by decreasing microrod LED diameter. This increasing diameter can be explained by decreasing strain relaxation and increasing radiative recombination rates according to the decreasing diameter. Moreover, the power density of microrod LEDs was higher than the power density demand for optogenetics applications. This means that fabricated GaN LEDs have enough light intensity for the optogenetics applications.
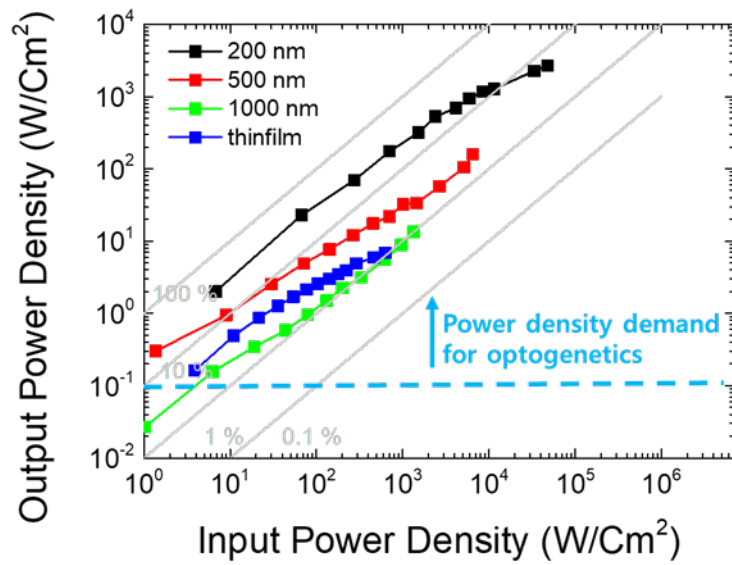
Figure 5.7. Power efficiency plot from the different diameter of GaN micro LEDs. Output power density according to the input power density. The output power was measured by photodiode and the input power was calculated by multiplying applying current and voltage.

5.4. Intracellular potential variation stimulated by GaN LEDs

Figure 5.8 shows that the intracellular potential variations from the cells were measured with patch clamp method. To stimulate the cells, we used GaN microrod and thin film LEDs with various pixel size. In normal condition, the intracellular potential was around –60mV compare to the extracellular environment. When the LED light was turned on, the intracellular potentials were rapidly increased and saturated in 100 msec. The rapid increasing intracellular potentials were due to the opening the CHETA cation channel. When the ChETA cation channel opened, the cations such as sodium and potassium were rapidly flow into cell along the potential difference. The intracellular potentials were sustained during the LED light turned on. During the LED light was turning on, the potential variation was saturated so to balance potential difference and osmotic pressure of cations. The intracellular potential was rapidly decreasing in few msec when the light was turned off because the other endogenous ion channel and pumps rapidly recover the intracellular potential and ion concentration to normal condition. When we turning on the light, the maximum potential level was different from the LED pixel size and pulse width. The light intensity is increasing with increasing LED pixel size and this increasing light intensity can open more ChETA channel. This can induce higher cationic current level into cell.   If the pulse width is less than 100 ms, the maximum potential levels were lower. After the light illumination, around 100 ms is need for reaching the saturation potential. If the pulse width is

less than 100 ms, ChETA cation channel will be closed before saturation current and this results less maximum potential level according to the decreasing pulse width. In the 1ms pulse width, inctracellular potential variation was not observed. Presumably, the pulse width was not enough to open the ChETA channel. Microrod LED showed similar results compare to the thin film case. In the microrod LED with 50x50 μm^2 pixel size, around 100 microrod LEDs were contained and the illumination area was much less than the thin films with same pixel size. But, the higher potential variation was observed from the microrod LED compare to the thin film LED. This is due to the thickness of PDMS passivation layer. The thickness of PDMS passivation layer was around 500 µm and 50 µm in the thin film and microrod case respectively.
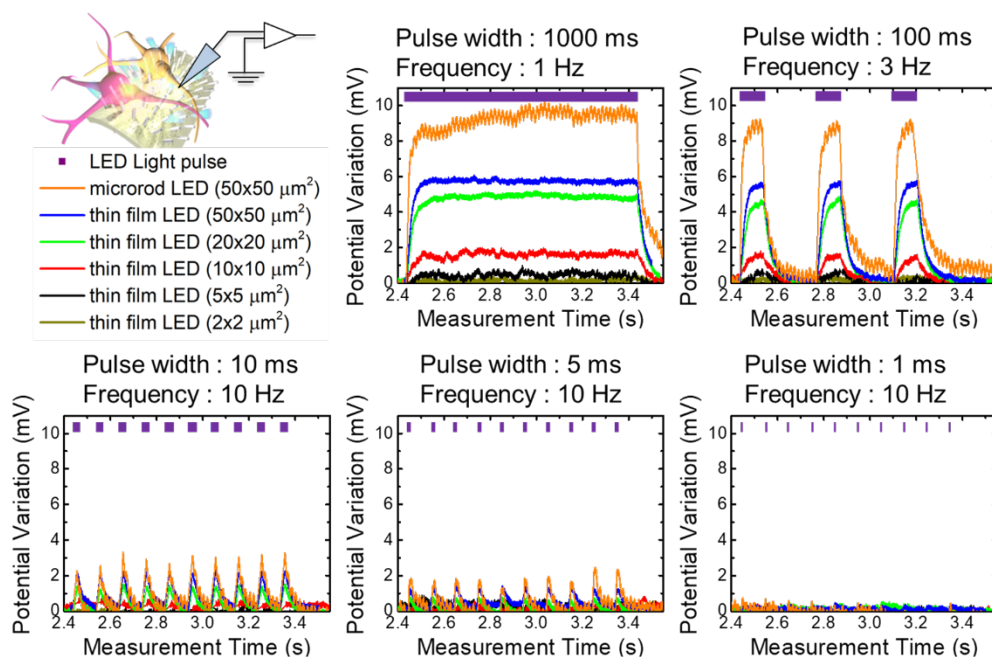
Figure 5.8. Intracellular potential variations from the cells. The intracellular potential variation was measured by whole cell patch clamp. CHETA cation channel was activated using the different GaN micro LEDs.

5.5. Summary

The GaN microrod LEDs were fabricated on the thin film LED. The diameter of 200 nm nanorod LED also fabricated using dry and wet etching processes. The fabricated GaN microrod LEDs showed that enough output power for the optogenetics experiment. Moreover, the diameter of 200 nm nanorod LED showed higher power efficiency by reducing strain relaxation and increasing radiative recombination rates. This imply that this submicron diameter GaN nonorod LED can be used for the specific region in a neuron cell. The intracellular potential variations from the cells were measured with patch clamp method. To stimulate the cells, we used GaN microrod and thin film LEDs with various pixel size. In normal condition, the intracellular potential was around –60mV compare to the extracellular environment. This results shows that this nano-/microrod LEDs can be used for practical applications for optogenetics.

Concluding remarks and outlooks

6

6.1. Summary

The goal of this dissertation was bio-medical applications using GaN microrod. Especially, GaN microrods grown on graphene films were used for intracellular laser and fabricated GaN microrod LEDs were used for optogenetics application. The lasing characteristics from the intracellular GaN microrod lasers were studied. And, this showed promising results for cell labeling. The GaN microrod LEDs were fabricated on thin film LED using etching processes. The optogenetics experiment was performed using this GaN micro LEDs. Followings are detailed experiment results

The GaN microrods grown on graphene films using MOVPE exhibited excellent lasing characteristics. The use of graphene as a substrate enabled facile detachment of the GaN microrods from the substrate and dispersion into culture media for internalization into cells. The small volume and high aspect ratio of GaN microrods allowed cells to internalize cells by endocytosis, thereby avoiding injection. Excellent lasing signals were observed under intracellular conditions due

to the optical quality and high refractive index of the GaN microrods. We believe that intracellular GaN microrod lasers are suitable for cell labeling and tracking applications.

The GaN microrod LEDs were fabricated on the thin film LED. The diameter of 200 nm nanorod LED also fabricated using dry and wet etching processes. The fabricated GaN microrod LEDs showed that enough output power for the optogenetics experiment. Moreover, the diameter of 200 nm nanorod LED showed higher power efficiency by reducing strain relaxation and increasing radiative recombination rates. This imply that this submicron diameter GaN nonorod LED can be used for the specific region in a neuron cell. The intracellular potential variations from the cells were measured with patch clamp method. To stimulate the cells, we used GaN microrod and thin film LEDs with various pixel size. In normal condition, the intracellular potential was around –60mV compare to the extracellular environment. This results shows that this nano-/microrod LEDs can be used for practical applications for optogenetics.

6.1. Future works and outlook

(1) Multifunctional neural probes using nano LED light source array and neural probes.

The feasibility of nano LED light source was demonstrated in this thesis. This nano LED light source also can be used for the specific synapse or dendrite in

neuron cell. It can be useful for basic neuroscience study or manipulate specific region in neuron cells. This GaN nanostructure can be used for neural probes that can measure the electrical neuron signal. GaN nanorod diameter less than 200 nm can penetrate cell membrane to measure the intracellular potential variations. By integrating these two functions, the multifunction neural probe can be fabricated using GaN nanorod LEDs.

(2) Artificial neural network using GaN nano structures

Neuron and other mammalian cells can also be cultured on the nanostructure. Moreover, the cultured cells show specific patterns according to the nanostructures because of interaction with cells and nanostructures. Neuron cells can interact chemically and electrically with synaptically connected other neuron cells. The fabricated GaN nanostructure with different patterns and dimensions can affect in neuron cell culturing patterns. Cultured neuron pattern can be controlled and specific artificial neuron network also can be achieved by controlling this nano patterns. This artificial neuron circuit may give us more information in neuroscience and other applications.

Appendix A

Position and morphology controlled ZnO nanotube growth on CVD graphene films

A.1. Introduction

The position and dimension controlled growth of 1D materials have been attracted tremendous attention due to their various applications. There was difficulty in position and morphology controlled growth of 1D inorganic materials. Moreover, most of inorganic material growth was performed on the single crystal substrate because of epitaxial growth. In this chapter, the position and morphology controlled 1D ZnO nanotube was grown on the 2D graphene layers. This controlled growth can give more advantage in many applications. And, the ZnO nanotubes grown on graphene films can easily be transferred onto arbitrary substrate because of weak an der Waals bonding of graphene layers.

A.2. Growth behavior of ZnO nanotube on graphene films

Morphology of selectively grown ZnO on CVD graphene is affected by various growth parameters. In this chapter, effect of growth temperature, reagent supply and chamber pressure on morphology of ZnO nanosturcture were studied.

A.2.1. Effect of growth temperature on ZnO nanotube morphology

The effect of growth temperature for ZnO nanotubes was investigated by changing the growth temperatures from 500 to 660 °C. Figure A.1. displays the SEM images of ZnO nanostructures grown at different temperatures. The morphology and growth selectivity of ZnO nanostructures grown on CVD-graphene films dramatically changed according to the growth temperature. At low process temperature of 500 °C, ZnO nanowalls were grown on the whole area of SiO$_2$ growth-mask covered region. We can see a hexagonal array of short tubular nanostructures among the nanowall structure. By increasing growth temperature, the nanowall grown on the growth mask layer was not observed i.e., growth selectivity increased. And, the average aspect ratio of ZnO nanostructures grown at designed positions was increased. At 550 °C of growth temperature, truncated cone-shaped nanostructure hexagonal array was observed with some lumps on the void between each nanotube. As shown in Figure A.1., the truncated cone-shaped nanostructures altered to straight tubular structures, i.e., vertically aligned natotubes. At 640 °C of process temperature, the SEM image shows a clearly defined hexagonal array of ZnO nanotubes. When the process temperature reached 660 °C, the tips of ZnO nanotubes were split.
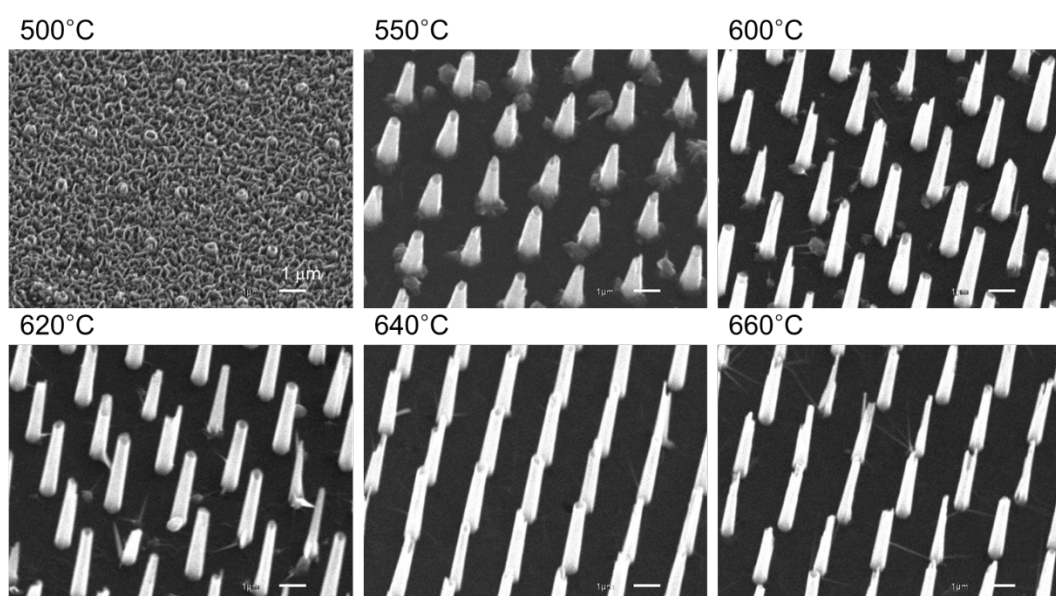
Figure A.1. Temperature dependent ZnO nanotube growth behavior.

SEM images after ZnO nanotube growth on graphene films with different

growth temperature.

A.2.2. Effect of gas and metal-organic source molecular flow rate on ZnO nanotube morphology

Morphology and growth behavior of ZnO grown on selectively revealed CVD graphene layers was examined according to reagent flow rate (Figure A.2). Flow rate of Argon, which was used as carrier gas for DEZn, was varied by 10, 20, and 30 sccm and Oxygen gas flow rate by 50, 70, and 90 sccm. ZnO grown on CVD graphene layers shifted its morphology from a vertically grown nanotube to corn shape with nanoneedles on the top of the nanotubes as Oxygen flow rate increased. On the other hand, as DEZn carrier gas flow rate increased, its morphology changed from a corn shape to a tube and the needles were disappeared. Moreover, the growth rate was increase gradually according to the increasing DEZn flow rate. In conclusion, ZnO formed on selectively exposed CVD graphene layers tended to grown in the form of a tube under DEZn rich and Oxygen poor environment. Whereas, ZnO nanotubes gradually developed into a needle and then to an island, as DEZn supply decreased and Oxygen flow rate increased.
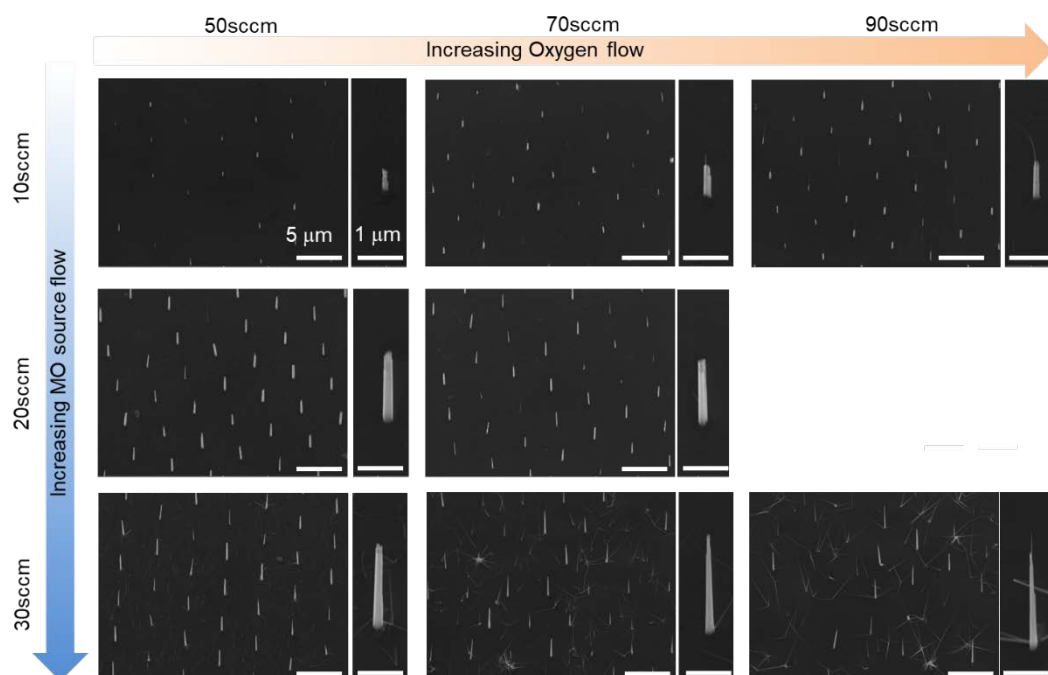
Figure A.2. ZnO nanotube growth behavior depending on metal-organic source and oxygen gas molecular flow rate. SEM images after ZnO nanotube growth on graphene films with different metal-organic source and oxygen gas molecular flow rate.

A.2.3. Effect of pressure on ZnO nanotube morphology

Growth tendency of selectively grown ZnO nanotube according to chamber pressure was investigated (Figure A.3). Chamber pressure was maintained at 40, 9, 5 and 3 Torr. Morphology of ZnO was not changed significantly from a tube, but its vertical growth rate gradually increased along with the growth pressure. However, at the 40 Torr, the growth behavior was significantly changed. The ZnO was grown on the whole surface and the hight of ZnO nanotubes on the patterned surface is also short.
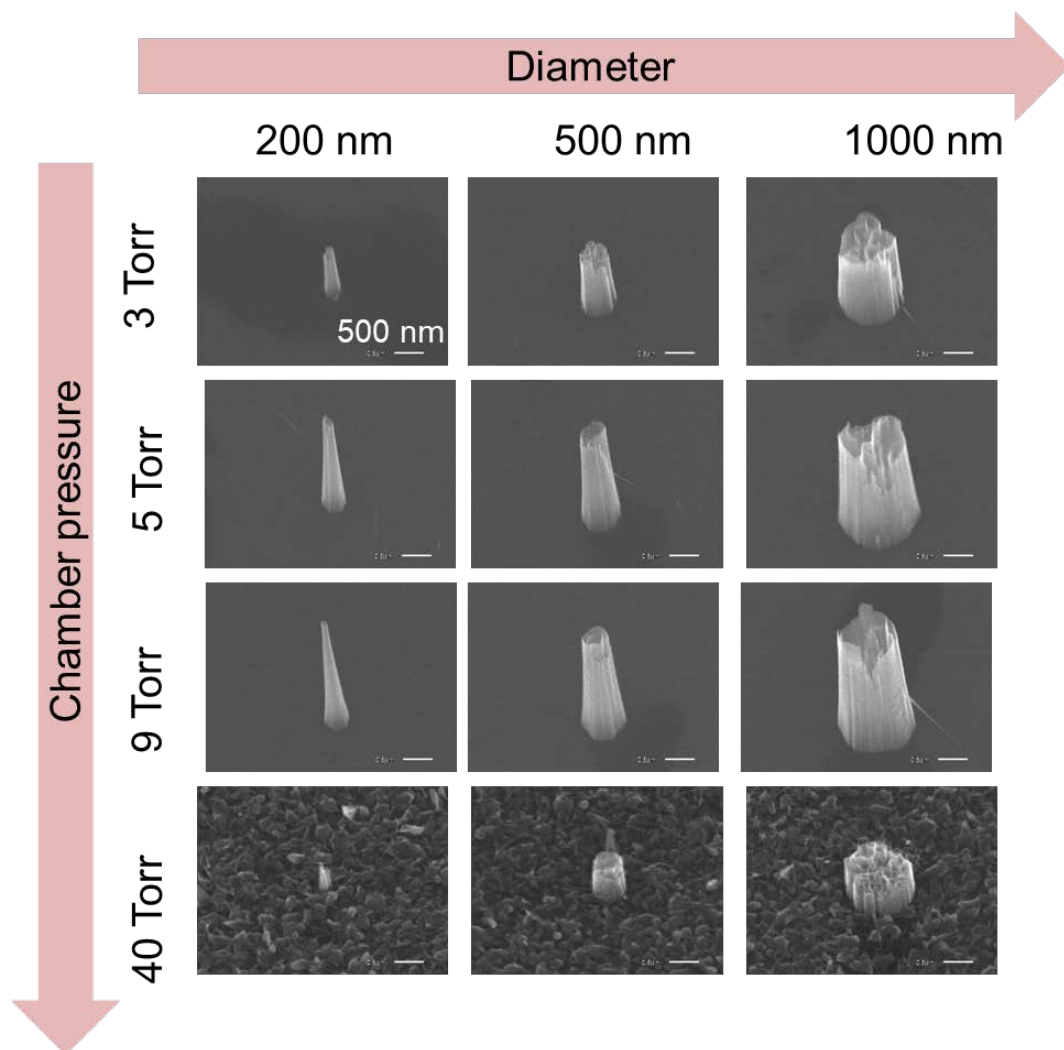
Figure A.3. ZnO nanotube growth behavior depending on chamber pressure. SEM images after ZnO nanotube growth on graphene films with different chamber pressure.

A.2.4. Effect of etching time on ZnO nanotube morphology

The dry and wet etching condition are very important for growth of ZnO nanotube on the SiO_2 growth mask. After lithography, the SiO_2 film was etched using dry-etching, followed by wet etching using CF4 plasma and BOE. The residual oxide layer on the graphene after dry etching was completely removed using BOE. For dry etching, we used OXFORD P80 RIE ETCHER. Usual etching condition was 45 sccm, 5 sccm, 150 W, 50 mTorr for CF_4 gas flow rate, Ar flow rate, RF power, and pressure, resectively. Usual thickness of SiO_2 growth mask was 50nm. Because plasma gas can etch not only SiO_2 growth mask but also graphene layer, dry etching condition should be optimized precisely. If not, then graphene layer will be etched and ZnO nanostructure cannot be grown on the graphene films. Figure A.4 shows that the SEM images with different RIE dry etching time and BOE etching time. As dry RIE etching time increases, graphene also etched and there are no ZnO nanotubes. This etching condition is very sensitive to condition of equipment and thickness of growth mask. To remove the remained SiO_2 growth mask wet etching using Buffered Oxide Etcher (BOE) should be treated after dry etching. Unlike RIE dry etching using CF_4 gas, BOE wet etching doesn't affect to graphene layer. But, wet etching is an isotropic etching process. So too much wet etching on samples can distort the patterning. And it could affect to overall area of the sample, it could be one of the reason of bad surface selectivity. Usual BOE wet etching time was 10 sec.
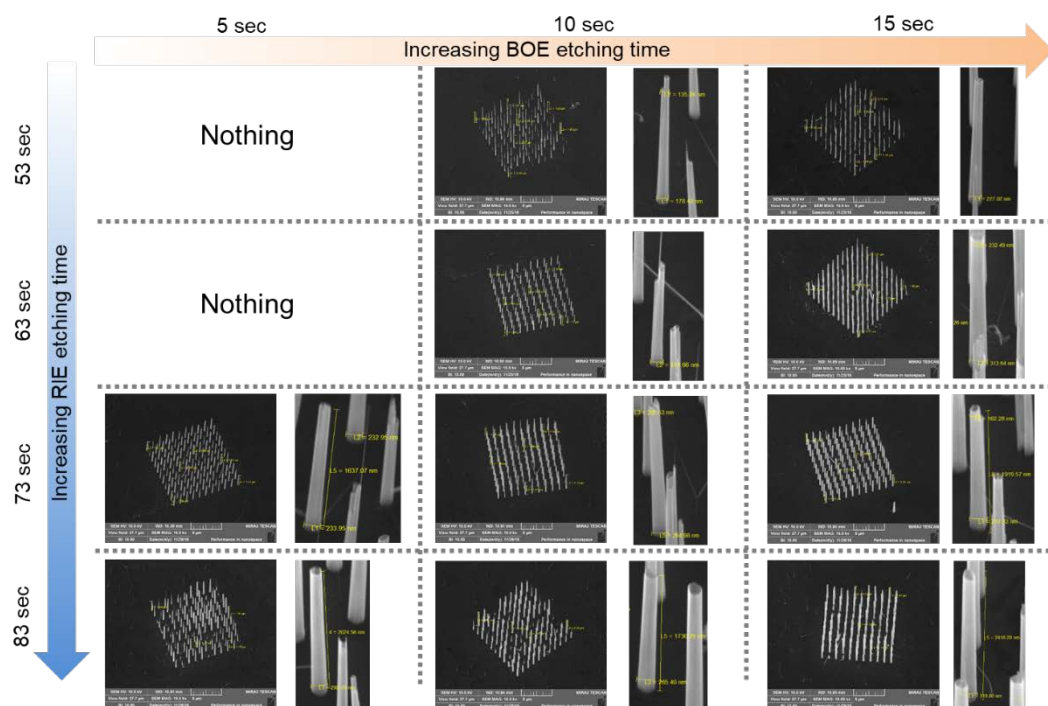
Figure A.4. ZnO nanotube growth behavior depending on wet and dry etching conditions. SEM images after ZnO nanotube growth on graphene films with various SiO$_2$ growth mask wet and dry etching conditions.

A.3. Summary

In this chapter, the position and morphology controlled ZnO nanotbue growth behavior according to the different growth conditions and growth mask etching conditions. The growth behavior was sensitively changed by growth temperature, metal-organic source and oxygen gas molecular flow rate, growth pressure, and growth mask etching conditions. This growth conditions can be used for other applications.

Appendix B

Highly-sensitive, flexible pressure sensors using ZnO nanotube arrays grown on graphene films

B.1. Introduction

1D piezoelectric nanomaterials have attracted tremendous attention due to their diverse applications ranging from sensors to microdisplay as well as the self-powered devices. Although a lot of research has been carried out to exploit the piezoelectric properties of the nanomaterials as high sensitivity pressure sensor, the application is restricted when the pressure is too small (<1Pa). On the other hand, inorganic nanomaterial-based pressure sensors are also constrained to utilize as flexible and wearable applications such as healthcare devices. Conventionally, flexible piezoresistive pressure sensors are composite polymers with conductive fillers (i.e., active phase) such as carbon nanotubes (CNTs), metallic nanofibers and nanoparticles.[39-41] However, the sensing performance of piezoresistive pressure sensors based on low cost composite elastomers with a planar structure is low and easily degrades in ambient atmosphere. Therefore, significant research attention are focused on the pressure sensors composed of piezoelectric inorganic nanomaterials

having considerable sensitivity, mechanically robust yet flexible. Amongst various piezoelectric material system, ZnO based nanotube/nanowires are considered to be highly advantageous for piezoelectronic devices.[42-45] However, there are some major obstacles in manufacturing pressure sensing devices using semiconductor nanostructures. Firstly, controlled fabrication of high- quality, 1D ZnO nanomaterials is a great challenge and enormous effort is required to achieve these nanomaterials. Secondly, combining 1D nanomaterials with a flexible substrate is a huge obstacle over the years. The difficulties accompanied by solid single crystal substrates can be circumvented by using graphene films as growth templates. The graphene films are extremely flexible and stretchable due to their excellent mechanical strength, perfect for flexible device application. Importantly, its thermal and chemical stability, as well as a hexagonal structure, made it possible for their use as a crystal growth template. Recently, vertically aligned, dimension and position-controlled ZnO nanotube arrays are grown on CVD-graphene films. These 1D ZnO nanotube arrays on graphene are expected to have plenty of potential for addressing the problems and challenges associated with the fabrication of flexible and wearable pressure sensors.

Here, we present the fabrication process and demonstration of 1D piezoelectric pressure sensors with flexibility and high-sensitivity. The device is fabricated using ZnO nanotube arrays grown on CVD-graphene films. The CVD-graphene films are not only a growth buffer but also work as a bottom electrode, which forms a flexible

Ohmic channel between ZnO nanotubes and metal electrodes. Meanwhile, the thin diameter and high aspect-ratio of nanotubes offer the flexibility of each nanotube that is enabling respond to a tiny external pressure with a nanostructure bending. The prototype sensor showed considerable pressure response over a wide range of pressure with a considerable sensitivity. The capability of detecting the tiny airflow enabled its potential application as a human breath and pulse sensor.

B.2. fabrication of ZnO nanotube pressure sensor

The highly sensitive flexible ZnO nanotube pressure sensor was fabricated using position and morphology controlled ZnO nanotube arrays grown on chemical vapor deposited (CVD) graphene films[29]. Figure B.1(a) represents the schematic illustrations for the fabrication processes of ZnO nanotube pressure sensor on CVD-grown graphene films. Before growing the nanorods, a SiO_2 growth mask layer of thickness 50 nm was deposited on the graphene films using plasma-enhanced CVD (PECVD). Conventional e-beam lithography technique was used for patterning the substrate and subsequent dry and wet etching techniques were used to make a sub-micron hole array pattern on SiO2-coated CVD-grown graphene films. Then vertically aligned ZnO nanotubes were grown selectively on the exposed graphene layers. The growth was performed 690 °C by using metal organic CVD (MOCVD) of ZnO from a high-purity (six nines) Diethylzinc source. Accordingly, these methods enable us to grow ZnO nanotubes with an outer diameter of 200–300 nm

and a height of 15–18 μm, which were employed for the fabrication of pressure sensor. The field-emission scanning electron microscopy (FESEM) image of as-grown ZnO nanotube arrays are shown in Figure B.1(b). In order to fabricate freestanding as well as flexible pressure sensors from those ZnO NTs, a novel and superior approach was adopted. The nanotubes grown on graphene films were easily transferable onto various foreign substrates including flexible printed circuit board (FPCB) due to the weak van der Waals bonding between graphene films and the original substrates. Polyimide (PI) layer was coated on the ZnO nanotube arrays to lift-off efficiently along with the graphene layer. Furthermore, PI layer was partially etched using an oxygen plasma asher to expose the tips of ZnO nanotube arrays for making a metal-semiconductor junction. This PI layer also acts as an insulating layer between top and bottom electrodes. Then, Au 100 nm was deposited on the top side of ZnO nanotube to make Schottky contact (ZnO/Au) and Cr/Au with 10/90 nm were deposited at the bottom side to make Ohmic contact (ZnO/graphene/Cr/Au). The corresponding cross-sectional schematic of fabricated ZnO nanotube pressure sensor is shown in the Figure B.1(a). Optical microscope (OM) and FESEM images of a fabricated sensor is shown in the Figure B.1(c).
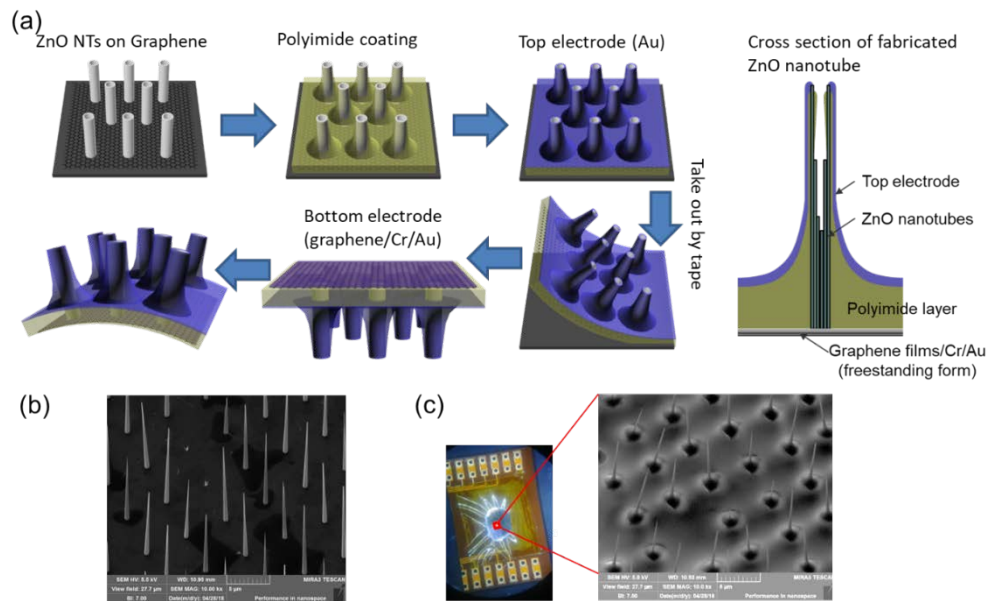
Figure B.1. Fabrication of ZnO nanotube-based pressure sensor. (a)
Schematic diagram of the process used to fabricate the ZnO nanotube
pressure sensor using the ZnO nanotube arrays heteroepitaxially grown
on graphene layers with cross sectional schematic of fabricated ZnO
nanotube pressure sensor. (b) Field-emission SEM (FE-SEM) images of
a ZnO nanotube array on a graphene substrate. (c) An microscope image
of fabricated flexible ZnO nanotube pressure sensor.

B.3. Current responses of ZnO nanotube pressure sensor

For further investigation of sensitivity of ZnO pressure sensor at ultra-low pressure, we used the mass flow controller (MFC) for applying ultra-low pressure. The measurement system is schematically shown in Figure B.3(a). A MFC with a resolution of less than 0.1 sccm was used to apply the pressure on the pressure sensor. To avoid the chemical reaction with ZnO nanotube and applying gas, we used Ar gas and the direction of applying gas was normal to the sample surface. In this experiment, we fix the distance between sensor and outlet of MFC as 2 mm. We flowed Ar gas from the 10 sccm to 1000 sccm for applying pressure and the 10 sccm corresponds to less than 0.5 Pa pressure. We calibrated pressure from the flow of gas in a constant rate using a weighing machine with accuracy of 0.1 mg. For further investigation of the relationship between the applying gas flow rate and the current variation, we applied the different amount of gas flow onto the pressure sensor using MFC. The clear current variation was observed according to the increasing gas flow rate (Figure B.3(b)). With small flow rate under 100 sccm, the dramatically increasing current varying ratio was occurred but the increasing current varying ratio was almost saturated at the high flow rate more than 200 sccm. It may due to the bending of ZnO nanotube was saturated. In this case, the bending mechanism may different from the voice coil motor. When we applied the pressure with voice coil motor, the force was unidirectional (normally from top of nanotubes only) and hence the ZnO NTs were bent in one direction only. Under gas flow

condition, the gas molecules can apply the pressure not only on the top end of nanotubes but also on the side wall of nanotubes because of the turbulence of gas molecule at the surface of pressure sensor. Note that, this gas turbulence can cause not only the bending but also small vibration of ZnO nanotube. Due to this, the current variation is very significant at ultra-low pressure. On the other hand, higher fluctuation was observed in case gas flow (Figure B.3(b)) as compared to the case of voice coil motor for applying pressure (Figure B.2(c)). In the Figure B.3(c), gradually decreasing sensitivity can be observed which is possibly due to the increasing elastic resistance with increasing bending of ZnO nanotubes. The ZnO nanotube pressure sensor shows vary high sensitivity (0.0108 sccm^{-1}) at low gas flow <100 sccm. In the >200 sccm flow range, the sensitivity of ZnO nanotube pressure sensor was reduced to 0.0047 sccm^{-1}. This decreasing sensitivity with increasing applying pressure has been reported in many papers.[46-48] If we tilt the direction of gas flow, most of gas molecules can directly apply the pressure at the side wall of ZnO nanotubes. These results higher current varying ratio than the normal flow direction. However, this high sensitivity and capability of detecting ultra-low pressure opens up huge opportunity to use in a variety of daily-life applications.
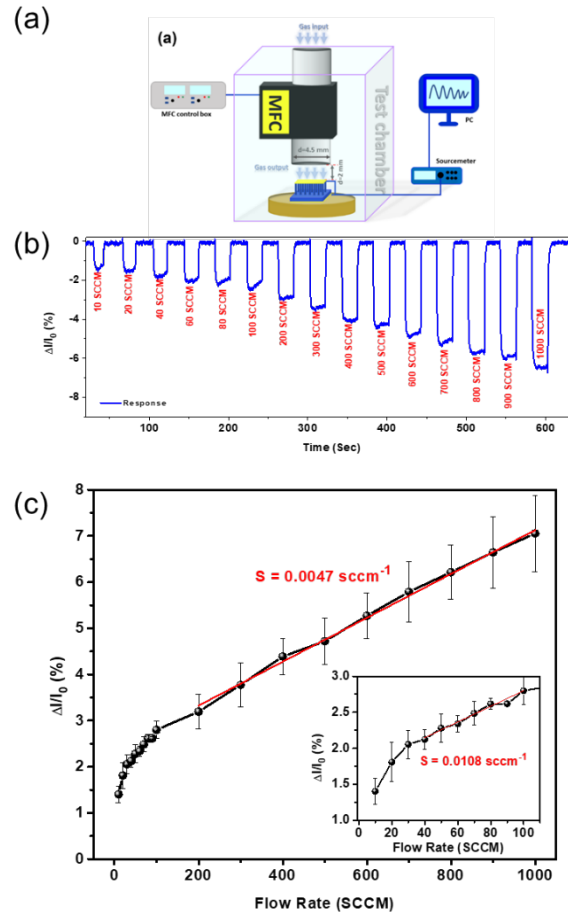
Figure B.2. Current response of ZnO nanotube pressure sensor. Pressure was applied by mass flow controller (MFC) with Ar gas. (a) Schematic of the measurement system to characterize the performance of the ZnO nanotube pressure sensor device. (b) Current response of ZnO nanotube pressure sensor with different applying pressure. (c) Current varying ratio $\Delta I/I_0 = (I-I_0)/I_0$ of ZnO nanotube pressures sensor with different applying gas flow. The inset shows the corresponding curve at ultra-low flow rate (10-100 sccm)

B.4. Pressure responses according to the different ZnO nanotube dimensions

Figures B.3 shows that the dramatic change in sensitivity according to the thickness of ZnO nanotube. The experimental method and setup was same as in the figure B.3(a). The sensitivity of pressure sensor was decreasing with increasing thickness of ZnO nanotube. As we expected the pressure response of ZnO nanotube pressure sensor with 30 nm wall thickness shows the high fluctuation with high pressure response because the high aspect ratio of ZnO nanotube can be more affected by not only applying pressure but also gas turbulence. At low gas flow <200 sccm, The ZnO nanotube pressure sensors showed different sensitivity of –0.0186, –0.0097, and –0.0055 in case of 30, 170, and 600 nm wall thickness, respectively. In the >200 sccm flow range, the sensitivity of ZnO nanotube pressure sensors were reduced to –0.0059, –0.0028, and –0.0019 for the 30, 170, and 600 nm wall thickness, respectively. The higher sensitivity decreasing was observed from the pressure sensor with thinner ZnO nanotube because the pressure response was not changed dramatically in >200 sccm flow range.

We also investigated the pressure response change from the pressure sensor according to the length of ZnO nanotube. Figure B.4(a) shows that ZnO nanotube with length of 7, 12, 18 µm were prepared after 1, 2, and 3 hrs vertical growth, respectively. But, the exposed length of ZnO nanotube was 2, 7, 12 µm because the thickness of PI layer was 5 µm. The vertical growth rate was estimated to be 6

µm/hr. The thickness of ZnO nanotubes was fixed to 600 nm after 4 hrs lateral growth followed by vertical growth. Figures B.5(b, c) shows that the dramatic change in sensitivity according to the length of ZnO nanotube. The sensitivity of pressure sensor was decreasing with decreasing length of ZnO nanotube. It was also expected that the pressure response from the pressure sensors with the high aspect ratio of ZnO nanotube can be more affected by applying pressure. At low gas flow <200 sccm, The ZnO nanotube pressure sensors showed different sensitivity of –0.0055, –0.0047, and –0.0003 in case of 18, 12, and 7 µm length of ZnO nanotubes, respectively. In the >200 sccm flow range, the sensitivity of ZnO nanotube pressure sensors were reduced to –0.0019, –0.0014, and -3×10^{-5} for the 8, 12, and 7 µm length of ZnO nanotubes, respectively. In this case, the dramatic sensitivity decreasing was also observed from the pressure with different length. These results shows that the sensitivity of ZnO nanotube pressure sensor can be adjusted by changing the ZnO nanotube aspect ratio for practical applications.
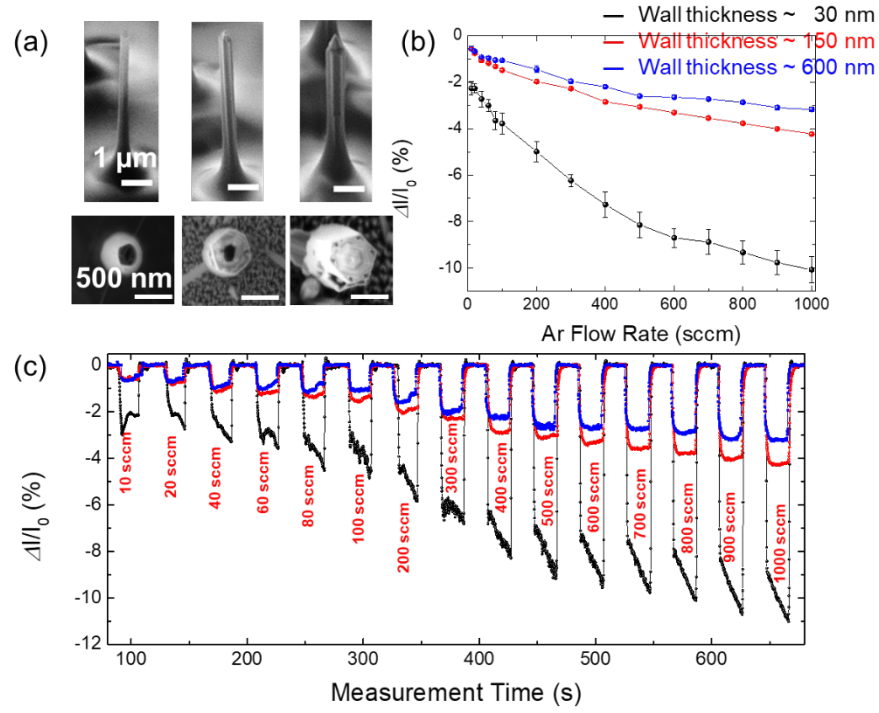
Figure B.3. Pressure responses according to the different ZnO nanotube thickness. (a) SEM images of ZnO nanotubes. (b) Current varying ratio $\frac{\Delta I}{I_0} = \frac{I - I_0}{I_0}$ of ZnO nanotube pressures sensor with different.

(c) Current response of ZnO nanotube pressure sensor with different applying pressure.
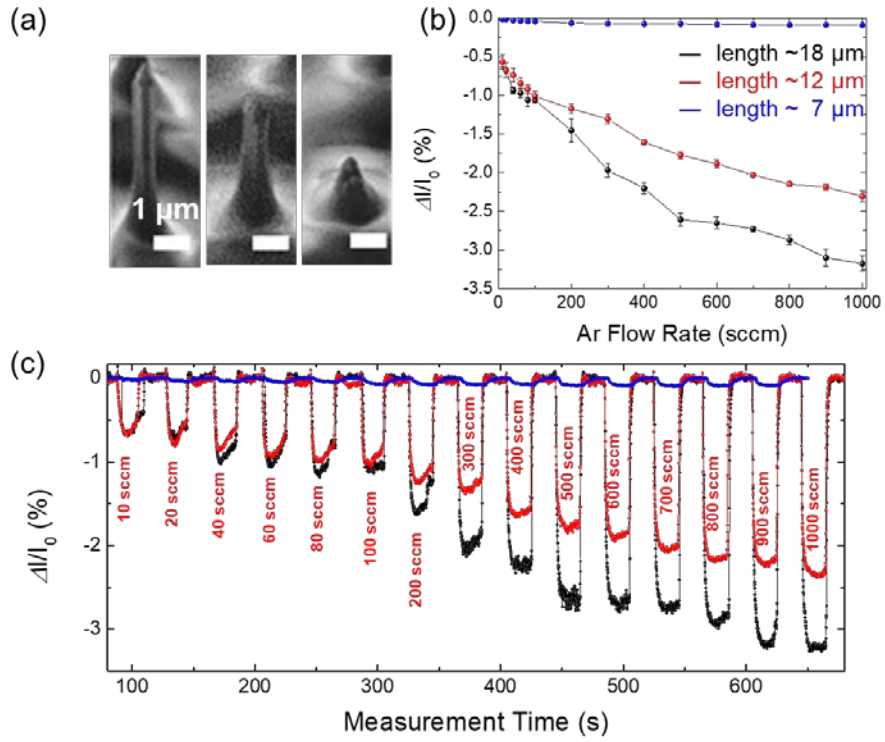
Figure B.4. Pressure responses according to the different ZnO nanotube length. (a) SEM images of ZnO nanotubes. (b) Current varying ratio $\frac{\Delta I}{I_0} = \frac{I - I_0}{I_0}$ of ZnO nanotube pressures sensor with different. (c) Current response of ZnO nanotube pressure sensor with different applying pressure

B.5. Bio-medical applications using flexible ZnO nanotube pressure sensor

For demonstration of practical application such as medical applications, we tried to detect human breath and pulse using ZnO nanotube-based sensor. In modern preventive medicine, monitoring of human vital sign is important for diagnosis of various diseases at the early stage. The pattern of breath is a key indicator for diagnosis of sleep apnea that can induce many other complications such as cardiovascular and brain injury.[49,50] For detecting the human breath, we attached our flexible sensor device on the philtrum (Figure B.5(a)). We found that the sensor can resolve the significant change in normal and hold breathing as shown in Figure B.5(b). In normal breathing, the respiration rate was 15–25 per a minute. This corresponds to normal for a specific adult person at rest. This result indicates that the sensor can be used to detect a simple pause in normal breathing, which is the symptom of sleep apnea.

Wrist pulse is also a key indicator of arterial blood pressure and heart rate by providing lots of useful information for noninvasive medical diagnosis. For example, cardiovascular disease such as atherosclerosis is in asymptomatic phase in the very early stage, but it leads arterial pulse pathologic and affects arterial blood pressure, hence continuous monitoring arterial blood pressure by wrist pulse will provide a rapid and noninvasive way for diagnosing cardiovascular diseases. In

order to monitor the blood pulse, we placed our flexible sensor device on the wrist (Figure B.5(c)).   We have monitored the pulse of a normal person at rest and the same after a small workout (running) as shown in Figure B.5(d) The pulse rate was found to be 13 per 10 sec, whereas it was 16 after running. The current varying ratio (depth of pulse) was also increased around from 0.4 % to 0.5 % after running due to stronger heartbeat. This result is very promising for the use of the present sensor as exercise counter.
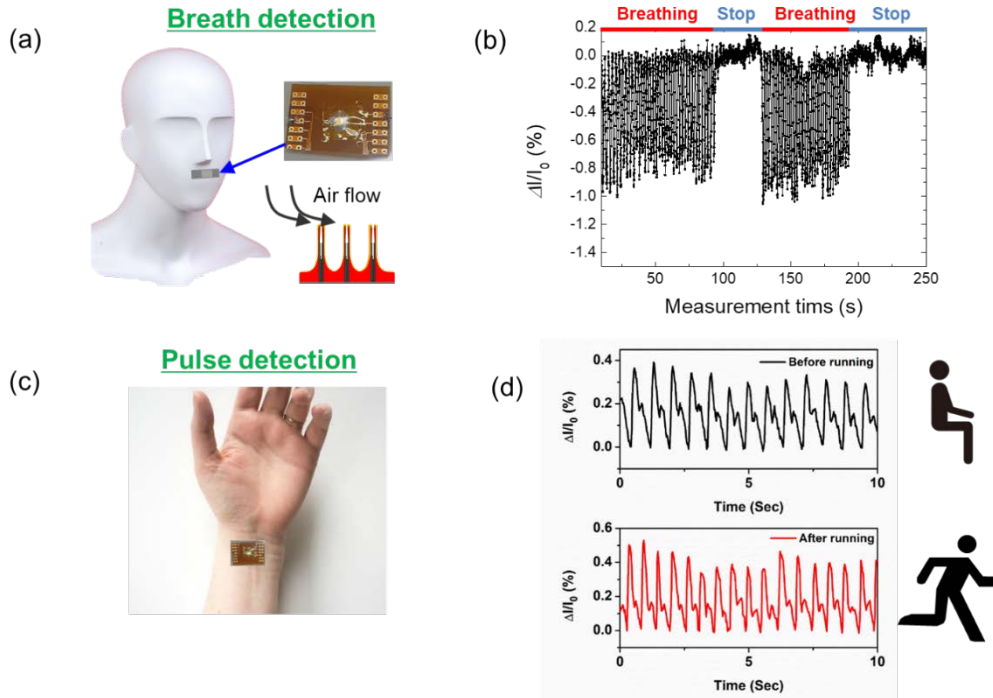
Figure B.5. Bio-medical applications using flexible ZnO nanotube pressure sensor. (a) The schematic shows directly attached to philtrum for detecting human breathing. (b) Real time current response of the ZnO pressure sensor during monitoring human breathing. (c) The schematic shows directly attached to wrist for human pulse detection. (d) Real time current response of the ZnO pressure sensor during monitoring human pulse before and after running.

B.6. summary

We have fabricated piezoresistive pressure sensors by utilizing vertically aligned, position- and dimension-controlled ZnO nanotube arrays on graphene layers and successfully demonstrated the practical application of these sensors for preventive medicine. A facile and novel approach is adopted for the transfer of ZnO nanotubes arrays for fabricating the freestanding as well as flexible devices. Our ZnO nanotube sensor has proven its high sensitivity (>0.3 kpa^{-1}) with fast response time (<10 ms), great stability with repeated applying pressure for more than one day. The prototype device has shown enough response to a pressure subjected by a small flow of inert gas. Moreover, we have demonstrated breath and pulse detection for preventive medicine applications with noninvasive way. This device can be one of promising candidate for the future wearable electronics for the diagnosis of pulmonary and cardiovascular diseases at the early stage.

Appendix C

Neuronal mRNP transport follows an aging Lévy walk

C.1. Introduction

A messenger ribonucleoprotein (mRNP) particle is a macromolecular complex consisting of messenger RNA (mRNA) and RNA binding proteins (RBPs). When a gene is activated, the genetic information in DNA is transcribed into mRNA, which is subsequently associated with many RBPs to form an mRNP complex. The mRNP particles are exported from the nucleus to the cytoplasm to be translated into proteins. However, certain mRNA molecules are not immediately translated into proteins but are rather stored in a translationally repressed state and transported to specific regions inside a cell.[51,52] In neurons, about one-third of mRNA species are transported from the cell body to the dendrites and axons[53] and locally translated into proteins upon signal transduction.[54] Local translation of mRNA has emerged as a key mechanism for regulating gene expression in space and time for long-term memory formation and neuronal development.[55,56] Moreover, dysregulated RNA localization and translation have been strongly associated with neurodegenerative and neurodevelopmental diseases.[57,58] Therefore, it is of

great interest to understand how mRNP particles are transported and targeted to specific locations inside a neuron.

Recent advances in RNA imaging techniques have enabled real-time observation of individual mRNP particles in living neurons and brain tissues.[59-61] While mRNPs in bacteria or fibroblasts exhibit mostly diffusive or subdiffusive motion[59,62,63], neuronal mRNPs show distinct directed motion along the dendrites[64]. Dendritic trafficking of mRNP has been shown to be mediated by microtubule-dependent molecular motors, kinesins and dyneins (Figure C.1a)[65]. A recently proposed scenario called the sushi-belt model states that mRNPs are stochastically transported along the microtubules bidirectionally until they are captured by synaptic tags at the activated synapses.[66] However, the search patterns of mRNPs as they reach their target sites are still largely unknown.[54]

Lévy walk is a physical regularization for Lévy flights that describes a generalized diffusion process in terms of a constantly moving particle of a finite velocity (in the simplest case) and the joint probability of its random flight (or jump) lengths and times.[67] The model has a finite second moment (mean squared displacement) $\langle x^2(t) \rangle$ and depending on the decay slowness of the random walker's distributions it encompasses from superdiffusion to normal diffusion with $\langle x^2(t) \rangle \propto t^\beta$ with $1 \leq \beta \leq 2$. Recently, interests in Lévy walks have risen within physics communities because they have been demonstrated to explain diverse complex dynamic phenomena, such as blinking quantum dots[68], cold atoms[69],

124

light in inhomogeneous media[70], and Hamiltonian systems[71-73]. In the biological sciences, foraging movements of diverse organisms from bacteria to humans have been modeled as a Lévy process.[74] It has also been suggested that Lévy strategies are more efficient for finding randomly located target objects compared with other mechanisms.[75-77] More recently, with the help of single-particle tracking techniques[78,79], it was shown that some biological superdiffusions such as motor driven active transport in the cytoplasm[80,81] and swarming bacteria migration34 exhibit patterns of Lévy walks in the sense that their flight length distribution or the velocity autocorrelation decays following a (truncated) power-law.

To the best of our knowledge, this report describes the first observation of an *in vivo* molecular transport process with superdiffusive characteristics that are consistent with an aging Lévy walk. Theoretically, this process belongs to an extended Lévy walk model, allowing a rest period between the successive flights. Previously, such Lévy models were int1roduced for a flow motion in a rotating annulus and a related Hamiltonian system.[72,73] In the neuronal mRNP motion studied here, we find that this type of Lévy walk process emerges because of the bidirectional microtubule-dependent transport by kinesin and dynein, which is interrupted by localization of mRNP at the target sites. It turns out that the dynamics of neuronal mRNP, distinguished from the pause dynamics in the tug-of-war motion of molecular motors[73,82], exhibits heavy-tailed scale-free sojourn time statistics,

125

resulting in a sub-ballistic Lévy walk with weak ergodicity breaking (WEB) and aging. Intriguingly, aging masks WEB within the observational time window of this study. By combining single-particle tracking experiments with a theoretical study of the proposed Lévy walk process, we investigate the complicated in vivo mRNP dynamics with detailed analysis of various aspects. In the literature, Lévy-like superdiffusion has been identified mostly by the scaling analysis of the mean squared displacement (MSD) and/or the distribution profile of the flight length (or time) in a limited window. It is worthwhile to mention that beyond the simple experimental analyses, we explicitly set forth a predictive Lévy walk model for neuronal mRNP transport. Excellent agreement of this Lévy walk model with the experiment is demonstrated by various quantities, such as the ensemble- and time-averaged MSDs, the fluctuation of time-averaged MSDs, and the probability density function. Furthermore, the aging time of the observed mRNP particles in the experiment is deduced from the aging-dependent MSD curves predicted from the model. Also, the theoretical study of the Lévy model elucidates how the MSD exponents depend on the exponents of flight-localization time distributions, aging time, and noisy environment.

C.2. Active transport of individual endogenous mRNP in neurons

A schematic diagram of mRNP movement in a neuron is depicted in Figure B.1a. A newly transcribed mRNA binds multiple RBPs to form an mRNP, which is subsequently transported into a dendrite. There are multiple microtubule tracks

along each dendrite. An mRNP particle is transported bidirectionally by concerted work of motor proteins along the microtubules. Using a genetically engineered mouse that expresses β-actin mRNA labeled with green fluorescent proteins (GFPs)[59], we imaged individual β-actin mRNP particles in hippocampal neurons using wide-field fluorescence microscopy. Because each β-actin mRNA is labeled with up to 48 GFPs, individual mRNPs appear as bright spots in fluorescence images (Figure C.1b). In neurons, mRNP complexes, often called neuronal RNA granules, contain many RBPs and ribosomes and are particularly large with an estimated size of 175–600 nm[83]. The addition of 48 GFPs, each of which is approximately 4 nm in diameter, would not significantly alter the overall size of RNA granules (less than 0.06% difference) or their native dynamics. By tracking these spots in time-lapse images, we monitored the active transport of mRNP particles in live neurons. We selected a region of interest along a dendrite, as highlighted in yellow in Figure C.1b, and generated a straightened image of the dendrite. From the straightened timelapse image stack, we obtained one-dimensional trajectories of individual mRNPs along the curvilinear line of the dendrite they reside in. Shown in Figure C.1c is one of the obtained kymographs from the selected regions of dendrites. Here, the x- and y-axes represent the elapsed time and the distance along the dendrite, respectively. We collected data from 57 cells in 12 batches of neuron culture and obtained 101 kymographs. The trajectories

of 682 mRNP particles were analyzed with a time resolution of $t_0 = 100$ ms and a

spatial resolution of 205 nm.
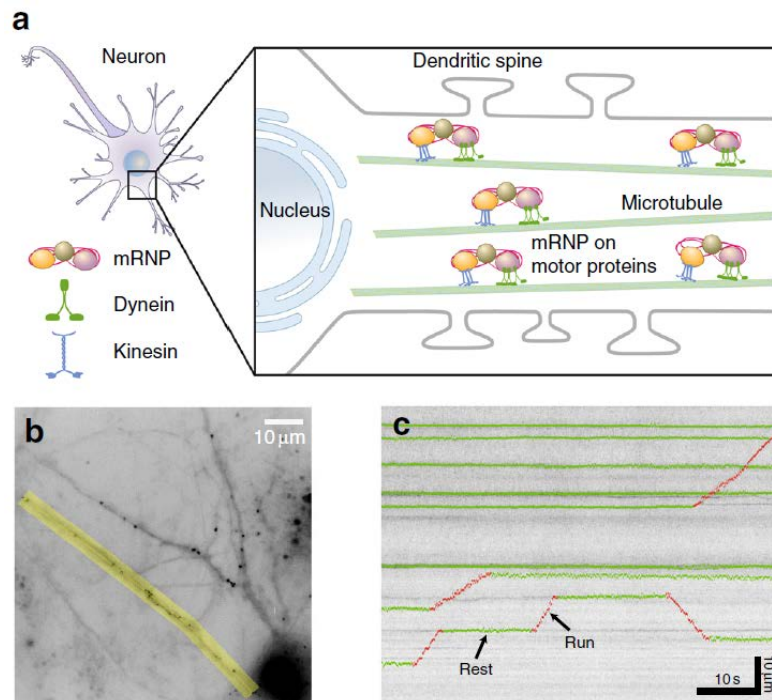
Figure C.1. Schematic and experimental data showing motor-driven transport of mRNPs in a neuron. (a) An ensemble of mRNP complexes are transported by kinesin and dynein motor proteins along microtubules in the dendrite. (b) A live-cell image showing fluorescently labeled β-actin mRNP complexes in a hippocampal neuron. The region of interest for analysis is marked in yellow. Scale bar, 10 μm. (c) A kymograph for an ensemble of mRNP particles obtained from an image similar to the yellow area in (b). For a few trajectories, their two distinct dynamic modes, rest and run, are denoted in green and red, respectively. The kymographs exhibit constant small-length scale fluctuations. Scale bars, 10 s and 10 μm, respectively.

C.3. Transport of mRNP is composed of discrete runs and rests

The kymographs show that the mRNP transport is intermittent and stochastic in nature. The motion of mRNP comprises two phases: namely, the directed movement, referred to as 'run' in either the anterograde or retrograde direction, and the 'rest' period (see the schematic in Figure C.2a). We segmented the kymographs into these two phases and analyzed them separately. It turns out that run is indeed a ballistic motion where the MSD grows with the power exponent of about 2. Meanwhile, rest is a very slow subdiffusive motion, with the exponent $\beta \approx 0.1$ for the average MSD curve. Such seemingly subdiffusive motion for the trapped particles is ubiquitously observed in various systems, stemming from the viscoelastic anti-correlated positional fluctuation in crowded media.[84-86] In the kymographs, an mRNP particle is transported along the dendrite in such a pattern that its dynamic state is repeatedly switched between the run and rest phases with random sojourn times. Here, we note that the rest phase dominates over the run. For more than 80% of the total trajectories analyzed in the experiments, the mRNP particles were in the rest phase over the total observation time of $T = 60$ s. This long rest, presumably associated with the localization of mRNPs, appears to be a unique feature of the RNA transport in neuronal systems. This behavior is distinguished from the previously reported motor-driven active transport in cytoplasmic environments, where runs are only interrupted by short pauses with durations

characterized by a sharply decaying probability density function (pdf) such as an exponential decay.[81,87]

We further investigated the statistical properties of both dynamic states. We estimated the conditional probabilities of the four possible directional combinations for all consecutive runs separated by a rest. The four probabilities turn out to be fairly even, suggesting no directional memory in the mRNP transport. Shown in Supplementary Figure C.3a is the velocity distribution of all individual runs. The velocity profile is almost symmetric in the anterograde and retrograde directions and exhibits two sharp peaks at ~ ±1 μm/s with narrow distributions. Consistent with these data, a linear relation between the run length and time was found. The larger error bar at longer run times is due to the smaller number of the observed events. From the curve, the average speed of mRNPs during a run period was estimated to be 1.25 μm/s. This value lies within the range of the kinesin or dynein speed experimentally estimated *in vitro* and *in vivo*.[88] In addition, we treated neurons with nocodazole to disrupt microtubules and found that the percentage of mRNPs with run phase was significantly decreased. This result suggests that intact microtubules are needed for run phase of mRNP movements.

Figure C.2b, c presents experimentally determined pdfs of run and rest times, respectively. It is found that both distributions have substantially long tails; an mRNP particle is continuously transported, by a single run, for up to >20 s corresponding to distance of 20 μm, within our observation time. The run time pdf

131

is found to be nicely explained by an exponentially truncated power-law of the form $\psi_r(t) \propto \frac{exp(-t/\tau_r)}{(t+t_0)^{1+\gamma}}$. The dashed line in Figure C.2b depicts the best fit to the data with the estimated characteristic run time τ_r = 12.5 s and γ = 0.52. Although the difference in the goodness of fit between the truncated power-law and a simple power-law is rather small, the exponential truncation ensuring the finiteness of mRNP run times is essential in explaining the observed mRNP dynamics as described in the next section. Previously, such an exponentially decaying run distribution was theoretically elucidated within the tug-of-war model of the motor-driven cooperative transport dynamics of cargos on microtubules.[87] The pdf of run length was found to be similar to that of run time because of the relation of $l = |v|t$. In Figure C.2, the pdf of rest times has a much longer tail than that of run times. This is expected from Figure C.1c, in which rest events with periods exceeding T are substantially found. The rest times follow a power-law decay of the form $\psi_s(t) \propto 1/(t + t_0)^{1+\alpha}$ (dashed curve in Figure C.2c), with the waiting time exponent $\alpha \approx 0.32$. From the fact that the rest events have a diverging average time, $\langle t \rangle = \int t\psi_s(t)\mathrm{d}t \rightarrow \infty$, it can be inferred that the overall transport dynamics of mRNP particles is highly affected by the statistics of the occurrence of long rest events.

We investigated in detail the anomalous transport dynamics of mRNPs. Plotted in Figure C.2d are time-averaged (TA) MSD curves $\overline{x^2(\tau)}$ as a function of

lag time τ for all individual mRNP trajectories found in the experiment (see Caption for the definition of TA MSD). Huge heterogeneity exists in individual transport dynamics, which is primarily attributable to their localization events. The average curve over all $\overline{x^2(\tau)}$ is depicted with the thick line (blue). In Figure C.2e, the more commonly used ensemble-averaged (EA) MSD $\langle x^2(\Delta t)\rangle$ is plotted as a function of elapsed time Δt from the initiation of measurement, compared with the averaged TA MSD (blue) in Figure C.2d. Both curves, having almost the same behaviors at least up to $T = 60$ s, exhibit the following anomalous characteristics: first, superdiffusive transport of mRNPs is transient; second, they are sub-ballistic with the MSD exponent $\beta \approx 1.6 < 2$; and third, it is also notable that the short-time dynamics (of times <1 s) are not ballistic. Instead, the MSDs grow non-algebraically from a nonzero offset value at $\Delta t = 0$. As will be investigated in the simulation below, this turns out to be the consequence of positional fluctuations prevailing at short length scales, shown as a small wiggling in the kymograph trajectories. For times $>O(10)$ s, it appears that the superdiffusive motion is slowed down to a Fickian diffusion with the exponent $\beta \approx 1$. The observed trends in MSDs are not due to the inclusion of the abundant silent trajectories that correspond to a single rest event of a duration greater than or equal to the observation window T. Consistent scalings are found for TA and EA MSDs evaluated only with the subset of trajectories that have at least one run phase during the observation.
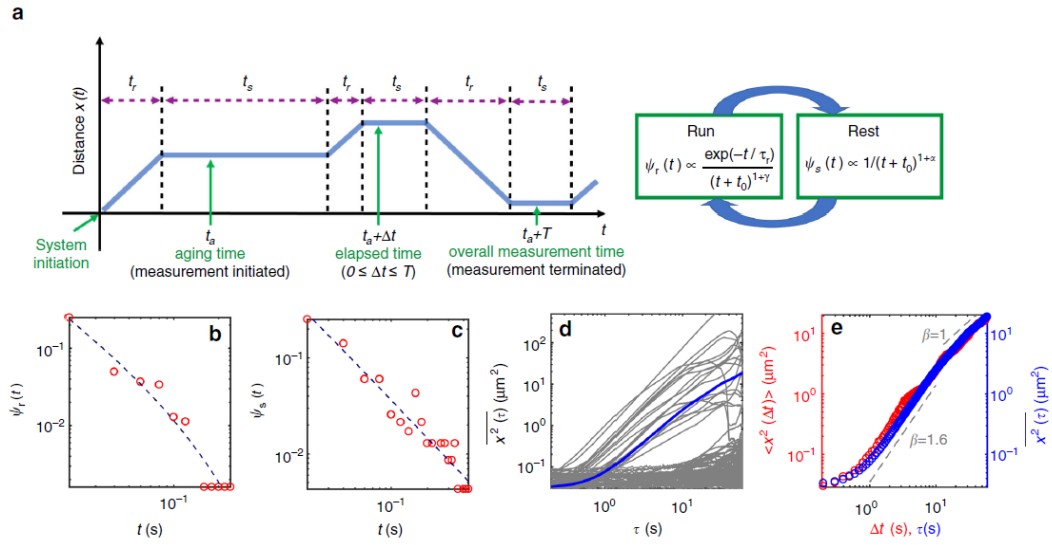
Figure C.2. Stochastic transport dynamics of individual mRNP particles. (a) A simplified diagram describing an individual mRNP motion. The flow diagram shows the distribution of the sojourn times. The direction of run is either anterograde or retrograde with equal probability and without memory of the previous run. (b) Experimental data of the run time pdf $\psi_r(t)$. (c) Experimental data of the rest time pdf $\psi_s(t)$. The rest times follow a power-law distribution (dashed line). (d) TA MSD curves from individual trajectories. Thick line (blue) denotes the average curve over all TA MSDs. (e) EA MSD (red) plotted together with the average TA MSD curve (blue) shown in (d)

C.4. Transport of mRNP is composed of discrete runs and rests

Based on the above experimental investigation, we quantified the mRNP transport dynamics in the framework of a generalized Lévy walk model. In accordance with the experimental data, the motion of an mRNP is described as an alternating sequence of the ballistically moving run and rest phases (see Figure C.2a). The mRNP sojourn time t is given by a truncated power-law pdf with $0 < \gamma < 1$. The space-time joint pdf of the Lévy walk is then given by $\psi_{run}(x,t) = \frac{1}{2}\delta(|x| - vt)\psi_r(t)$. This process is interrupted by the rest event, whose pdf, according to our observation in Figure C.2c, is modeled as a power-law function of $\psi_s(t) \propto \frac{t_0{}^\alpha}{(t+t_0)^{1+\alpha}}$ with $0 < \alpha < 1$. We emphasize that all the parameters required in this model are already determined from the experimental analyses above. In this sense the above Lévy walk is a fit-free model, enabling us to have a quantitative comparison between the experiment and the theory. Along with this truncated Lévy walk model, we considered a truncation-free Lévy walk having power-law pdfs for both ψ_s and ψ_r (i.e., $\tau_r \to \infty$) to quantify the effect of truncation on the transport dynamics. Note that for both Lévy walk processes, we are interested in the case where the rest times have a broader distribution than the run times, specified by the condition $0 < \alpha < \gamma < 1$ in our model. Simulations were performed with the parameter values determined from the experiment and with the initial condition (x, t) = (0, 0). The two processes look evidently different even within the experimental

observation time scale. For the truncated Lévy walk, the obtained trajectories (Figure C.3a) exhibit similar patterns observed in the mRNP motion (Figure C.1c); most trajectories contain rest periods longer than the overall observation time $T = 60$ s. The generalized Lévy walk including rests was previously introduced for a flow motion in a rotating annulus[72] and a related Hamiltonian system[73]. Recently, continuous time random walk models generalizing the conventional Lévy walks were studied.[89] In the context of single-particle behaviors[90,91], however, the current model has not been investigated to date.

For the proposed Lévy walk descriptions, we first investigated the properties of their MSDs. The EA and TA MSDs are plotted together in Figure C.3b. For the truncation-free model, both the EA and TA MSDs unanimously illustrate that the process becomes a sub-ballistic superdiffusion with the anticipated scaling exponent $\beta = 2 + \alpha - \gamma \approx 1.819$ soon after the short-time ballistic dynamics. This result contradicts with the experimental curve (Figure C.2e), which shows only a transient superdiffusion with $\beta \neq 1.8$. Thus, this disagreement strongly corroborates our analysis that the run time distribution is truncated. For the truncated Lévy walk, a distinct result is observed. Importantly, its dynamics are substantially nonergodic. Both the EA and TA MSDs have the same initial ballistic growth. However, for times longer than the τ_r, the EA MSD demonstrates subdiffusive dynamics of $\sim(\Delta t)$ α whereas the TA counterpart shows apparent Fickian dynamics of $\sim\tau^1$. This suggests that, depending on the method of averaging, the transport dynamics appear

seemingly different. This so-called WEB for $t > \tau_r$ is mainly attributed to the intervened heavy-tailed rest events. When $t \gg \tau_r$, the truncated Lévy walk is analogous to a subdiffusive continuous time random walk governed by a waiting time pdf $\psi(t) \propto (t + t_0)^{-(1+\alpha)}$. This process is shown to exhibit WEB where the time-averaging produces $\overline{x^2(\tau)} \sim \tau/T^{1-\alpha}$ albeit the underlying motion is subdiffusive with $\overline{x^2(t)} \sim t^\alpha$.[78,92,93] Notice, however, that the mRNP dynamics observed in Figure C.2e are apparently inconsistent with that of the truncated Lévy walk and its WEB (Figure C.3b).
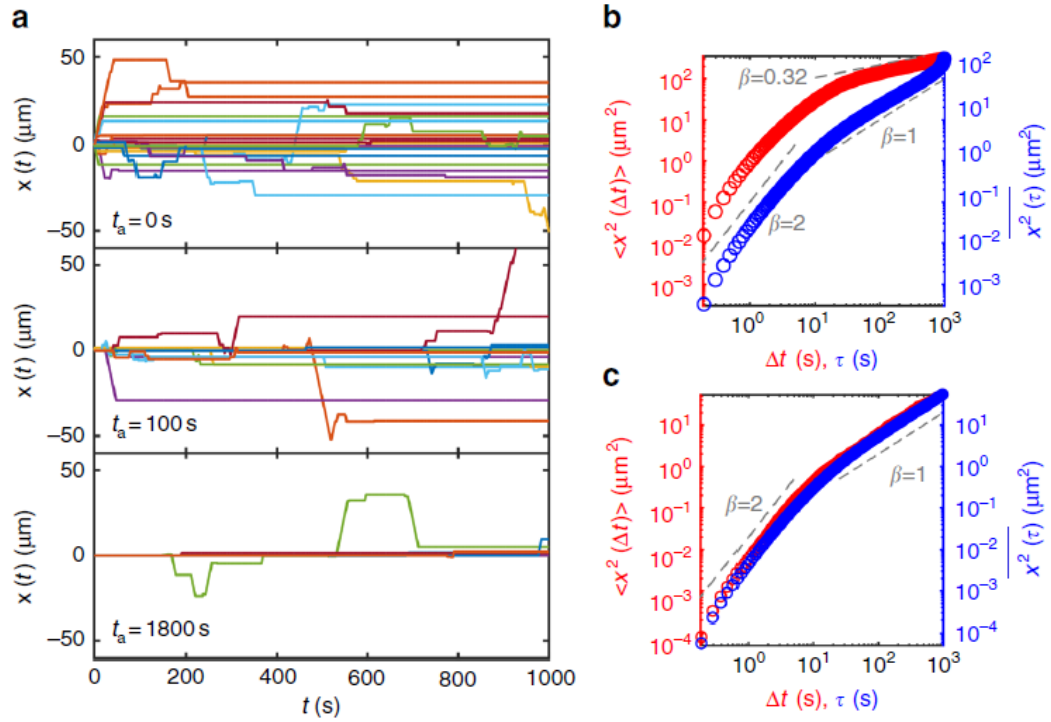
Figure C.3. Weak ergodicity breaking and aging in the simulation of truncated Lévy walk with rests. (a) Sample trajectories from the simulations with three different measurement initiation times t_a (see Figure C.2a). Top: Lévy walk trajectories when the measurement begins with the start of the process ($t_a = 0$). Middle: Trajectories when the measurement is initiated at $t_a = 100$ s. Bottom: Trajectories with the aging time ta = 1800 s. In each panel, 436 trajectories are plotted, the majority of which are silent trajectories. (b) EA and TA MSD curves when the measurement initiation time is the same as the process start time (i.e., $t_a = 0$, top panel in (a)). Inequivalence between the EA and TA MSDs, called weak ergodicity

138

breaking, is clearly visible in this case. (c) EA and TA MSD curves when the measurement is initiated at t_a = 1800 s after the start of the process (bottom panel in (a)). Owing to aging, the EA MSD also shows the same apparent Fickian scaling as in the TA MSD for $\tau_r < \Delta t < T$.

C.5. Neuronal mRNP particles perform an aging Lévy walk

A key point to reconcile this discrepancy is the aging effect shown for non-stationary non-equilibrium processes including the neuronal mRNP transport.[78,94-96] In such systems, the apparent dynamics explicitly depends on the aging time $t_a(>0)$ at which the observation was initiated and on the elapsed time Δt from ta (see the schematic in Figure C.2a). We show the aging effect in our truncated Lévy walk process in Figure C.3a, where the simulated 436 truncated Lévy walks are plotted at three different tas. With increasing aging time, the motion tends to be more immobile and fewer particles display run phases. Using the sufficiently aged trajectories ($t_a = 1800$ s), in Figure C.3c, we plot the aged EA and TA MSDs for the time window $[t_a, t_a + T]$. It shows that aging seemingly violates WEB, altering the scaling relations of the MSDs; analogously to the experimental curves (Figure C.2e), the two aged MSDs appear almost identical within the observation duration T = 60 s, being apparently ergodic. Moreover, the EA MSD exhibits the Fickian scaling $\langle x^2(\Delta t; t_a) \rangle \sim \Delta t$ after the ballistic regime. The observed aging behaviors may be explained by the theory of aging renewal processes47. In terms of the elapsed time Δt, the aged EA MSD exhibits seemingly Fickian scaling $\langle x^2(\Delta t; t_a) \rangle \sim \Delta t / t_a^{1-\alpha}$ for $\Delta t \ll t_a$ but eventually recovers the non-aged subdiffusion scaling $\langle x^2(\Delta t; t_a) \rangle \sim (\Delta t)^\alpha$ or longer observation, i.e., $\Delta t \gg t_a$. Thus, the Fickian scaling in the experimental data (Figure C.2e) is interpreted as

the intermediate scaling of the aged EA MSD of the simulation data. A longer experiment would allow the observation of the terminal subdiffusive dynamics $\langle x^2(\Delta t; t_a) \rangle \sim (\Delta t)^\alpha$ as shown in the longer time scale. However, the aged TA MSD behaves as $\overline{\langle x^2(\Delta t; t_a) \rangle} \sim \Lambda_\alpha \left(\frac{t_a}{T} \right) \frac{\tau}{T^{1-\alpha}}$ with $\Lambda_\alpha(z) = (1+z)^\alpha - z^\alpha$[94], which means that the scaling relation is invariable to the aging, yet the amplitude is decreased with ta (blue curves in Figure C.3b, c). The exact same properties are observed for $\Delta t > \tau_r$ in the experiment and simulation (Figures C.2e and 3c).

At $\Delta t \lesssim \tau_r$, theoretically, the aging Lévy walk predicts the ballistic movement for mRNPs. However, a sub-ballistic motion with $\beta \approx 1.6$ is observed in the experiment (Figure C.2e). The apparent sub-ballistic dynamics are explained by considering the inherent noise from the subdiffusive motion of mRNP particles and/or the localization error in particle detection.[97] The noisy Lévy walk is constructed by superpositioning the original model with the noise extracted from the experimental data (see the idea of noisy continuous time random walks51). The effect of the noise is shown in a sample trajectory and the EA MSD. The simulation result shows that indeed the effect of the ambient noise is large enough to mask the ballistic exponent. The experimentally observed value $\beta \approx 1.6$ is seen as a crossover value from the ballistic to the Fickian exponent.

Based on the truncated Lévy walk with noise, we extracted the aging time of mRNP particles observed in our measurement. In the experiment, we obtained

hundreds of mRNP traces that have different t_a s from the moment $t = 0$ the particle

begins to be loaded and transported by motor proteins. With the assumption that the

distribution for the random aging time has a well-defined mean value, we plot in

Figure 4a, b the theoretical MSDs at different aging times $\langle t_a \rangle$ for our Lévy walk

process. With the average aging time $t_a \sim 100$ s, we found excellent agreement

between the experiment and simulation for both EA and TA MSDs (Figure C.4a, b).

Surprisingly, both their amplitudes and scalings are well explained by the simulated

truncated Lévy walk process with $t_a \sim 100$ s.

We cross-checked that the aging effect indeed exists in the mRNP transport

by examining several additional dynamic quantities as well as the MSD curves.

Figure C.4c shows the plots of the individual TA MSD curves from the simulation.

The fluctuation of the TA MSDs from their average value (blue line) at a fixed lag

time is displayed in Figure C.4d. Here, the amplitude scatter distributions $\phi(\xi)$ are

plotted as a function of a rescaled variable of $\xi = \overline{x^2}/\langle \overline{x^2} \rangle$. The fluctuations in the

experimental data are consistently explained by the simulation data with $t_a \sim 100$ s

at various lag times of 5 s, 30 s, and 60 s. The sharp peak at $\xi \sim 0$ signifies a portion

of trajectories having no displacement, the population of which is increased with ta.

This effect has been coined as population splitting, and was first recognized.[94] In

Figure C.4e, we compare the aged probability density functions $P(x, \Delta t)$ of mRNP

particles determined from the experimental and simulation data. We also found

excellent agreement between the experiment and simulation with $t_a \sim 100$ s, with both having a sharp cusp at the origin. Finally, we estimated the probability $q(t_a;T)$ of finding a silent trajectory (i.e., no run event at all) in $[t_a, t_a + T]$ as a function of t_a (Figure C.4f)[94]. As expected from Figure C.3a, this probability increases with ta, eventually saturating to unity. Figure C.4f depicts the predicted $q(t_a;T)$ from the simulation in the presence of the experimental uncertainty of ~1 μm for discriminating rest (i.e., the silent trajectory) from run. From the experiment, q was estimated to be approximately 0.82 (the horizontal dashed line) for the overall observation time $T = 60$ s. Again, the expected aging time for $q \approx 0.82$ turns out to be $t_a \sim 100$ s. What, then, is the meaning of the measured aging time? Recall that ta is effectively the elapsed time starting from when mRNP particles had their first run to when the measurement is performed. Accordingly, the estimated aging time provides information about the effective distance $\sim \langle x^2(t_a) \rangle^{1/2}$ of mRNP particles from the cell body (dendrite entrance) when they were measured in the experiment. According to the theoretical EA MSD curve (Figure C.3b) of our Lévy walk, the traveled distance for the elapsed time $\Delta t = 100$ s is approximated to be ~10 μm. The estimated distance is indeed consistent with our experiment where the mRNP data for kymographs were taken in the proximal dendrite of length 0–50 μm from the cell body (Figure C.1b). The aging property presented here is a purely physical effect arising from the prevailing long rest events responsible for mRNA localization dynamics. Although the full microscopic mechanism underlying

143

mRNA localization is still unknown, the heavy-tailed rest time distribution may be associated with the dynamic nature of synaptic tags and their interactions with mRNP particles. For instance, the dynamic interaction between clathrin-coated pits and endocytic cargos also displays long-tail power-law statistics.[98] A similar effect may be present between synaptic tags and target mRNPs, but the molecular composition of synaptic tags still needs to be identified. Additionally, regarding the microscopic mechanism for the exponentially truncated run distribution, our control experiment demonstrated that run is a microtubuledependent directed motion. It is speculated that the exponential truncation is related to the microtubule-associated kinesin/dynein-driven transport in a tug-of- war manner.[87]
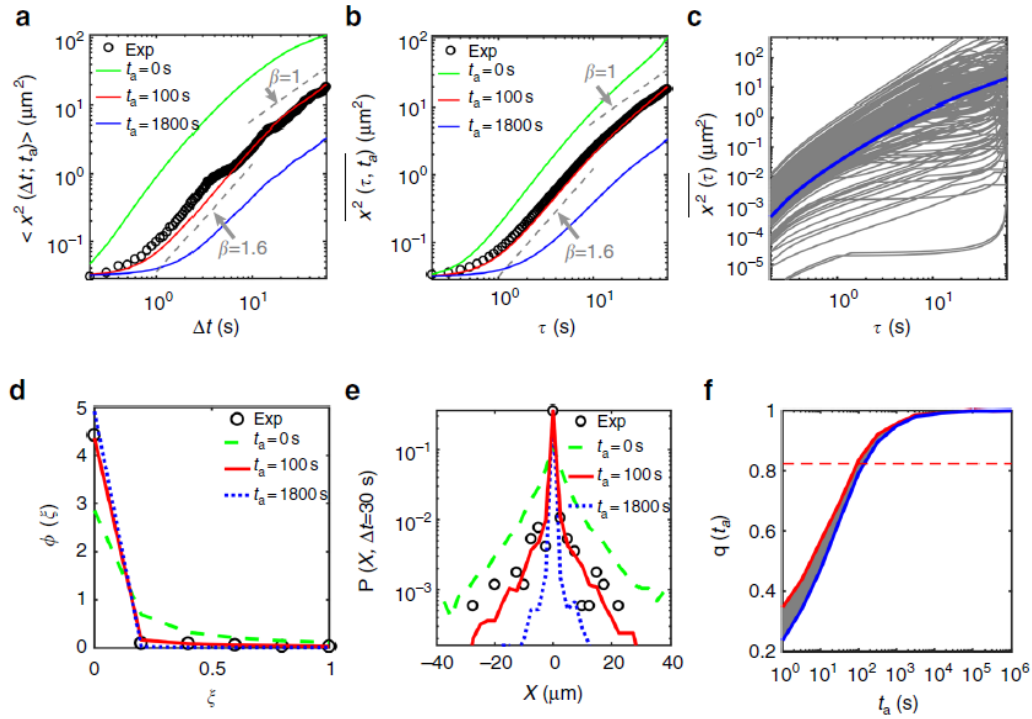
Figure C.4. Quantitative comparison of the experiment and simulation of the aging Lévy walk process. (a) Comparison of EA MSD curves for the aging Lévy walks at various aging times t_a = 0, 100, and 1800 s (green, red, and blue curves, respectively) with the EA MSD from the experiment (black circles, which is the same data shown as red circles in Figure C.2e). The simulation data at t_a = 100 s is in excellent agreement with the experimental data. (b) Comparison of TA MSD curves. The simulation data with aging time ta = 100 s, unequivocally, match both the EA and TA MSDs from the experiment. (c) Individual TA MSD curves of the aging Lévy walk processes with the aging time t_a = 100 s. The thick blue curve is the average

of the TA MSDs (gray curves). (d) Normalized amplitude scatter distributions $\phi(\xi)$ for the TA MSDs as a function of the rescaled variable $\xi = \overline{x^2}/\langle \overline{x^2} \rangle$. The experimental distribution from Figure C.2d (black circles) is compared with the theoretically expected distributions from the aging Lévy walk at three different aging times. (e) Aged probability density functions $P(x,\Delta t)$ of mRNP particles from the experiment and the aging Lévy walk simulations. (f) A fraction $q(t_a;T)$ of the trajectories showing no run at all in $[t_a, t_a + T]$ as a function of ta. Two theoretical curves for the aging Lévy walk were obtained from simulations with and without the uncertainty of ~1 μm (red and blue curves, respectively) for identifying the silent trajectories. Thus, the shaded region indicates the expected probabilities $q(t_a;T)$ in theory. The horizontal dashed line represents the experimental values for mRNP particles. It can be seen in the plot that the expected aging time is about $t_a = 100$ s.

C.6. Summary

In this study, we provide a systematic investigation on the stochastic transport and localization dynamics of neuronal mRNP particles *in vivo*. Their combined dynamics of individual mRNP particles follows a generalized aging Lévy walk comprised of a ballistic run with a truncated Lévy distribution of the sojourn times and a localizing rest with a Lévy distribution. The aging dynamics, distinguished from the usual Lévy-like superdiffusion in other biological systems, turns out to be a prominent feature of the neuronal mRNP transport having a broad spectrum of localization time scale. Upon key dynamic observables such as the scaling of EA and TA MSDs, fluctuations in TA MSD, aged probability density, and fraction of silent trajectories, our aging Lévy walk model demonstrates excellent agreement with the experiment as well as knowledge of the proper interpretation of nontrivial aging mRNP dynamics. While there have been a few theoretical models to predict the optimal parameters for mRNP trafficking in neurons, our study is the first to suggest a predictive theoretical model and to perform an extensive quantitative comparison between the model and experimental data. We envision that the aging Lévy walk model can serve as a framework for characterizing the transport dynamics of different cargos in neurons. It remains unknown how different mRNA molecules are packaged into distinct mRNP granules to be delivered to their own target sites. Likewise, other cargos, such as mitochondria, neurotransmitter receptors, and endoplasmic reticulum subcompartments, could

exhibit different transport characteristics. With more detailed information on transport and localization dynamics, a next step would be to evaluate the efficacy of the aging Lévy walk as an optimal search mechanism for hidden target sites.

References

[1] C. M. Denais *et al.*, Science **352**, 353 (2016).

[2] E. Akhan, D. Tuncel, and K. C. Akcali, Biomed Res Int (2015).

[3] G. Ariel, A. Rabani, S. Benisty, J. D. Partridge, R. M. Harshey, and A. Be'er, Nature Communications **6** (2015).

[4] G. van der Horst, J. J. van Asten, A. Figdor, C. van den Hoogen, H. Cheung, R. F. M. Bevers, R. C. M. Pelger, and G. van der Pluijm, Eur Urol **60**, 337 (2011).

[5] M. T. Hill and M. C. Gather, Nat Photonics **8**, 908 (2014).

[6] D. McGloin, Nat Photonics **9**, 559 (2015).

[7] K. M. Dean and A. E. Palmer, Nat Chem Biol **10**, 512 (2014).

[8] N. Martino *et al.*, Nat Photonics **13**, 720 (2019).

[9] A. H. Fikouras, M. Schubert, M. Karl, J. D. Kumar, S. J. Powis, A. Di Falco, and M. C. Gather, Nature Communications **9** (2018).

[10] X. Q. Wu, Q. S. Chen, P. Z. Xu, Y. C. Chen, B. M. Wu, R. M. Coleman, L. M. Tong, and X. D. Fan, Nanoscale **10**, 9729 (2018).

[11] H. Baek, J. K. Hyun, K. Chung, H. Oh, and G. C. Yi, Applied Physics Letters **105** (2014).

[12] L. Liu, M. Q. Sun, Q. Z. Li, H. M. Zhang, P. J. J. Alvarez, H. J. Liu, and W. Chen, Environ Eng Sci **31**, 373 (2014).

[13] M. Hofstetter, J. Howgate, M. Schmid, S. Schoell, M. Sachsenhauser, D. Adiguzel, M. Stutzmann, I. D. Sharp, and S. Thalhammer, Biochem Bioph Res Co **424**, 348 (2012).

[14] C. R. Chen and T. H. Young, Biomaterials **29**, 1573 (2008).

[15] K. L. Shaklee, R. E. Nahory, and R. F. Leheny, J Lumin **7**, 284 (1973).

[16] G. Miller, Science **314**, 1674 (2006).

[17] K. Deisseroth, Nat Neurosci **18**, 1213 (2015).

[18] E. S. Boyden, F. Zhang, E. Bamberg, G. Nagel, and K. Deisseroth, Nat Neurosci **8**, 1263 (2005).

[19] D. R. Hochbaum *et al.*, Nat Methods **11**, 825 (2014).

[20] N. C. Klapoetke *et al.*, Nat Methods **11**, 338 (2014).

[21] A. S. Chuong *et al.*, Nat Neurosci **17**, 1123 (2014).

[22] E. Meijering, O. Dzyubachyk, and I. Smal, Method Enzymol **504**, 183 (2012).

[23] M. Humar and S. H. Yun, Nat Photonics **9**, 572 (2015).

[24] M. Schubert, A. Steude, P. Liehm, N. M. Kronenberg, M. Karl, E. C. Campbell, S. J. Powis, and M. C. Gather, Nano Letters **15**, 5647 (2015).

[25] A. Berndt, O. Yizhar, L. A. Gunaydin, P. Hegemann, and K. Deisseroth, Nat Neurosci **12**, 229 (2009).

[26] A. Steude, E. C. Witts, G. B. Miles, and M. C. Gather, Sci Adv **2** (2016).

[27] N. Grossman *et al.*, J Neural Eng **7** (2010).

[28] D. C. Mao, N. W. Li, Z. S. Xiong, Y. B. Sun, and G. Y. Xu, Iscience **21**, 403 (2019).

[29] J. B. Park, H. Oh, J. Park, N. J. Kim, H. Yoon, and G. C. Yi, Apl Mater **4** (2016).

[30] D. Y. Wong, T. Ranganath, and A. M. Kasko, Plos One **10** (2015).

[31] K. Chung, H. Beak, Y. Tchoe, H. Oh, H. Yoo, M. Kim, and G. C. Yi, Apl Mater **2** (2014).

[32] S. Gradecak, F. Qian, Y. Li, H. G. Park, and C. M. Lieber, Applied Physics Letters **87** (2005).

[33] Q. M. Li, J. B. Wright, W. W. Chow, T. S. Luk, I. Brener, L. F. Lester, and G. T. Wang, Opt Express **20**, 17873 (2012).

[34] H. W. Xu *et al.*, Applied Physics Letters **101** (2012).

[35] E. Ejder, Phys Status Solidi A **6**, 445 (1971).

[36] P. Y. Liu *et al.*, Lab Chip **16**, 634 (2016).

[37] R. Caricchio, L. McPhie, and P. L. Cohen, J Immunol **171**, 5778 (2003).

[38] O. Yizhar *et al.*, Nature **477**, 171 (2011).

[39] C. H. Hu, C. H. Liu, L. Z. Chen, Y. C. Peng, and S. S. Fan, Applied Physics Letters **93**, 033108 (2008).

[40] S. Gong, W. Schwalb, Y. Wang, Y. Chen, Y. Tang, J. Si, B. Shirinzadeh, and W. Cheng, Nature Communications **5**, 3132 (2014).

[41] B. C. K. Tee, C. Wang, R. Allen, and Z. Bao, Nature Nanotechnology **7**, 825 (2012).

[42] Z. L. Wang, Advanced Materials **24**, 4632 (2012).

[43] R. Bao, C. Wang, L. Dong, R. Yu, K. Zhao, Z. L. Wang, and C. Pan, Advanced Functional Materials **25**, 2884 (2015).

[44] M. Y. Choi, D. Choi, M. J. Jin, I. Kim, S. H. Kim, J. Y. Choi, S. Y. Lee, J. M. Kim, and S. W. Kim, Advanced Materials **21**, 2185 (2009).

[45] K. Y. Lee, M. K. Gupta, and S. W. Kim, Nano Energy **14**, 139 (2015).

[46] Z. Q. Zhang, D. L. Geng, and X. D. Wang, J Appl Phys **119** (2016).

[47] Y. Zhang, Y. Liu, and Z. L. Wang, Advanced Materials **23**, 3004 (2011).

[48] Y. Gao and Z. L. Wang, Nano Letters **7**, 2499 (2007).

[49] M. H. Lee, C. H. Yun, A. Min, Y. H. Hwang, S. K. Lee, D. Y. Kim, R. J. Thomas, B. S. Han, and C. Shin, Sleep   (2019).

[50] J. S. Floras, Circ Res **122**, 1741 (2018).

[51] C. Eliscovich and R. H. Singer, Curr Opin Cell Biol **45**, 38 (2017).

[52] J. M. Taliaferro, E. T. Wang, and C. B. Burge, Rna Biol **11**, 1040 (2014).

[53] I. J. Cajigas, G. Tushev, T. J. Will, S. T. Dieck, N. Fuerst, and E. M. Schuman, Neuron **74**, 453 (2012).

[54] A. R. Buxbaum, Y. J. Yoon, R. H. Singer, and H. Y. Park, Trends Cell Biol **25**, 468 (2015).

[55] C. E. Holt and E. M. Schuman, Neuron **80**, 648 (2013).

[56] M. Costa-Mattioli, W. S. Sossin, E. Klann, and N. Sonenberg, Neuron **61**, 10 (2009).

[57] H. Jung, C. G. Gkogkas, N. Sonenberg, and C. E. Holt, Cell **157**, 26 (2014).

[58] L. Liu-Yesucevitz, G. J. Bassell, A. D. Gitler, A. C. Hart, E. Klann, J. D. Richter, S. T. Warren, and B. Wolozin, Journal of Neuroscience **31**, 16086 (2011).

[59] H. Y. Park, H. Lim, Y. J. Yoon, A. Follenzi, C. Nwokafor, M. Lopez-Jones, X. Meng, and R. H. Singer, Science **343**, 422 (2014).

[60] M. Vera, J. Biswas, A. Senecal, R. H. Singer, and H. Y. Park, Annu Rev Genet **50**, 267 (2016).

[61] H. C. Moon, B. H. Lee, K. Lim, J. S. Son, M. S. Song, and H. Y. Park, J Phys D Appl Phys **49** (2016).

[62] I. Golding and E. C. Cox, Phys Rev Lett **96**, 098102 (2006).

[63] T. J. Lampo, S. Stylianidou, M. P. Backlund, P. A. Wiggins, and A. J. Spakowitz, Biophys J **112**, 532 (2017).

[64] Y. J. Yoon, B. Wu, A. R. Buxbaum, S. Das, A. Tsai, B. P. English, J. B. Grimm, L. D. Lavis, and R. H. Singer, Proc Natl Acad Sci U S A **113**, E6877 (2016).

[65] N. Hirokawa, Journal of Neuroscience **26**, 7139 (2006).

[66] M. Doyle and M. A. Kiebler, EMBO J **30**, 3540 (2011).

[67] V. Zaburdaev, S. Denisov, and J. Klafter, Rev Mod Phys **87**, 483 (2015).

[68] F. D. Stefani, J. P. Hoogenboom, and E. Barkai, Phys Today **62**, 34 (2009).

[69] E. Barkai, E. Aghion, and D. A. Kessler, Phys Rev X **4** (2014).

[70] P. Barthelemy, J. Bertolotti, and D. S. Wiersma, Nature **453**, 495 (2008).

[71] M. F. Shlesinger and J. Klafter, Phys Rev Lett **54**, 2551 (1985).

[72] T. H. Solomon, E. R. Weeks, and H. L. Swinney, Phys Rev Lett **71**, 3975 (1993).

[73] J. Klafter and G. Zumofen, Phys Rev E **49**, 4873 (1994).

[74] A. M. Reynolds and C. J. Rhodes, Ecology **90**, 877 (2009).

[75] M. A. Lomholt, T. Koren, R. Metzler, and J. Klafter, P Natl Acad Sci USA **105**, 11055 (2008).

[76] V. V. Palyulin, A. V. Chechkin, and R. Metzler, P Natl Acad Sci USA **111**, 2931 (2014).

[77] G. M. Viswanathan, S. V. Buldyrev, S. Havlin, M. G. E. da Luz, E. P. Raposo, and H. E. Stanley, Nature **401**, 911 (1999).

[78] R. Metzler, J. H. Jeon, A. G. Cherstvy, and E. Barkai, Phys Chem Chem Phys **16**, 24128 (2014).

[79] C. Manzo and M. F. Garcia-Parajo, Rep Prog Phys **78** (2015).

[80] N. Gal and D. Weihs, Phys Rev E **81** (2010).

[81] K. J. Chen, B. Wang, and S. Granick, Nat Mater **14**, 589 (2015).

[82] J. M. Newby and P. C. Bressloff, B Math Biol **72**, 1840 (2010).

[83] R. B. Knowles, J. H. Sabry, M. E. Martone, T. J. Deerinck, M. H. Ellisman, G. J. Bassell, and K. S. Kosik, Journal of Neuroscience **16**, 7812 (1996).

[84] J. H. Jeon, H. M. S. Monne, M. Javanainen, and R. Metzler, Phys Rev Lett **109** (2012).

[85] I. Y. Wong, M. L. Gardel, D. R. Reichman, E. R. Weeks, M. T. Valentine, A. R. Bausch, and D. A. Weitz, Phys Rev Lett **92** (2004).

[86] J. H. Jeon, N. Leijnse, L. B. Oddershede, and R. Metzler, New J Phys **15** (2013).

[87] M. J. I. Muller, S. Klumpp, and R. Lipowsky, P Natl Acad Sci USA **105**, 4609 (2008).

[88] C. Kural, H. Kim, S. Syed, G. Goshima, V. I. Gelfand, and P. R. Selvin, Science **308**, 1469 (2005).

[89] M. Magdziarz and T. Zorawik, Phys Rev E **95** (2017).

[90] D. Froemberg and E. Barkai, Phys Rev E **87** (2013).

[91] A. Godec and R. Metzler, Phys Rev Lett **110** (2013).

[92] J. H. Jeon, V. Tejedor, S. Burov, E. Barkai, C. Selhuber-Unkel, K. Berg-Sorensen, L.

Oddershede, and R. Metzler, Phys Rev Lett **106** (2011).

[93]   A. Weron, K. Burnecki, E. J. Akin, L. Sole, M. Balcerek, M. M. Tamkun, and D. Krapf, Sci Rep-Uk **7** (2017).

[94]   J. H. P. Schulz, E. Barkai, and R. Metzler, Phys Rev X **4** (2014).

[95]   E. M. Bertin and J. P. Bouchaud, Phys Rev E **67** (2003).

[96]   X. Brokmann, J. P. Hermier, G. Messin, P. Desbiolles, J. P. Bouchaud, and M. Dahan, Phys Rev Lett **90** (2003).

[97]   H. Y. Park, A. R. Buxbaum, and R. H. Singer, Methods in enzymology **472**, 387 (2010).

[98]   A. V. Weigel, M. M. Tamkun, and D. Krapf, P Natl Acad Sci USA **110**, E4591 (2013).

Abstract in Korean(국문초록)

나노/마이크로 물질은 매우 작은 크기를 가지고 있으며, 이를 이용해 세포와 나노물질 사이의 바이오 인터페이스 형성에 유리다. 이러한 나노물질을 이용한 바이오메디컬 응용분야는 최근 각광을 받는 분야이며, 많은 연구자들에 의해 연구되어 왔다. 세포는 모든 생명체의 기본 단위이며 이러한 세포들의 크기는 수백 나노에서 수백 마이크로 사이에 있다. 이러한 이유로 바이오메디컬 응용을 하기 위해서는 만들어진 소자와 세포간의 직접적인 인터페이스 형성이 매우 중요하고 할 수 있다. 많은 바이오메디컬 응용분야 중에 광유전학 분야는 신경세포 연구에 널리 쓰이는 분야중 하나이다. 최근 많은 연구자들이 다양한 발광다이오드를 이용하여 광유전학 분야에 이용 가능한 소자를 연구 중이다.

높은 자유 엑시톤 결합에너지와 직접밴드갭을 갖는 질화갈륨은 발광다이오드 소자제작에 가장 적합한 물질중 하나이다. 특히 높은 광특성과 함께 무독성과 생체적합성을 갖는 질화갈륨 물질은 바이오메디컬 응용을 위한 적합한 소재라고 할 수 있다. 이를 이용한 바이오메디컬 응용분야는 많은 연구자들에 의하여 연구되고 있으며, 본 학위논문은 질화갈륨 나노/마이크로 소재와 질화갈륨 마이크로막대 발광다이오

드를 이용한 바이오메디컬 응용분야에 대하여 다룬다.

첫 번째 주제로는 질화갈륨 마이크로막대를 이용한 세포내 레이저 실험에 관하여 다룬다. 질화갈륨 마이크로 막대의 레이징 특성을 이용한 세포 라벨링은 다수의 세포추적을 위해 이용될 수 있다. 이를 위해 질화갈륨은 금속화학기상증착법을 이용하여 그래핀 위에 성장이 되었다. 약한 반데르발스 결합을 갖는 그래핀 기판위에 성장시킨 질화갈륨 마이크로막대는 손쉽게 기판으로부터 분리가 가능하다. 또한 크기가 작은 질화갈륨 마이크로막대는 자발적인 세포내이입과정을 거쳐 손쉽게 세포내부로 유입시킬 수 있다. 질화갈륨이 유입된 세포는 2주간의 세포배양 후에도 정상적인 세포이동과 세포분열을 나타내는 등 정상적인 세포활동을 보였다. 더욱이 세포내부로 유입된 질화갈륨 마이크로막대로부터 강한 레이징 신호가 측정됨을 확인 하였으며, 270 kW/cm^{2}의 낮은 레이징 문턱전력밀도를 보임을 측정 하였다.

이어지는 연구에서는 질화갈륨 마이크로막대 발광다이오드 소자의 제작과 이를 이용한 광유전학 분야로의 응용에 대하여 다룬다. 이 연구에서는 200 nm 의 지름을 갖는 질화갈륨 마이크로막대 발광다이오드 소자가 건식식각공정과 습식식각공정을 이용하여 제조 되었다. 또한 제조된 발광다이오드 소자에서는 광유전학 분야에 사용되기 충분한 세

기의 빛이 발광됨을 측정 하였다. 제조된 소자를 이용해 빛에 의해서 개폐가 조절되는 이온 채널이 발현된 세포를 자극하였으며, 세포내부에서의 전압변화가 패치 클램프 법을 이용해 측정 되었다.

Acknowledgement

제가 박사과정을 시작하여 박사를 받기까지 많은 분들의 도움이 있었습니다. 이 자리를 빌려 고마운 분들께 감사의 말을 전합니다.

우선, 박사학위 기간 동안 저를 지도해 주신 이규철 교수님께 감사드립니다. 저에게 연구뿐만 아니라 삶에 대한 자세 등 많은 것들을 알려 주셔서 감사합니다. 다만 제가 부족하여 교수님께서 지도해 주신 많은 사항들을 소화를 다 못하고 졸업하게 되어 후회도 되고 죄송스러운 마음이 많이 있습니다. 학위기간동안 교수님께서 지도해주신 많은 것들은 제 삶에 있어서 많은 것들을 깨닫게 해주셨으며 이 은혜는 잊지 않겠습니다. 졸업 후에 제가 어디로 가든 최선을 다해 열심히 살도록 하겠습니다. 감사합니다. 교수님.

또한 연구실에서 함께 연구한 선후배들에게도 감사의 말씀을 전합니다. 처음 연구실에 들어와 나에게 많은 것들을 알려준 현준이, 준범이, 종우. 잘 알려준 덕분에 박사학위 기간 동안 많이 도움이 되었어. 연구하는 동안 많은 토론을 하며 즐거운 연구실 생활을 하게 해주었던 영빈, 근동, 희훈에게 정말 고마워. 항상 친절하게 나를 대해 주었던 지영, 홍석에게는 함께한 시간이 짧아 아쉬운 마음이 커. 동주, Asad, 윤재, 자민에게는 더 많은 것들을 도와주고 모범이 되는 선배가 되어야

157

했는데 그렇지 못해 미안한 마음이 크네. 새로 우리 연구실에 들어온 현철, 석제, 현식은 교수님께 지도를 잘 받아서 훌륭한 연구자가 되길 바랄게. 연구실에서 함께 연구하며 연구에 관해 많은 조언과 도움을 준 Ramesh, Kumar, Puspendu 에게도 감사합니다. 실험을 하는데 많은 도움이 되어준 혜진누나, 희나씨, 현주씨 에게도 감사의 말씀 전합니다.

　　마지막으로 항상 제 편이 되어주고 옆에서 많은 힘이 되어준 제 가족들에게도 감사의 말씀을 드립니다. 항상 나를 믿어주고 응원해주고 걱정해준 엄마, 고마워. 지금까지 엄마에게 받은 것들을 고맙다는 말로 표현 하는 것이 아쉬울 따름이야. 그동안 바쁘다고 많이 챙겨주지 못한 동생에게는 미안한 마음이 많이 있어. 저희 가족을 보살펴 주시고 많은 도움을 주신 고모할머니, 고모할아버지, 성룡삼촌, 성희이모에게도 감사의 말씀을 드립니다. 많이 부족한 저와 경아의 결혼을 허락해 주신 장인, 장모님께도 감사드립니다. 그리고 사랑하는 연인이자 평생 동반자로 같이 함께할 경아는 내가 가장 힘들 때 옆에서 함께 있어줘서 고마워, 우리 앞으로도 행복하게 잘 살자.

Curriculum Vitae

Education

Seoul National University, Department of Physics   Sep. 2013 ~ Aug. 2020

Ph.D. Physics

*. Advisor: Prof. Gyu-Chul Yi

Kyung Hee Uuniversity, Department of Applied Physics   Mar. 2004 ~ Aug. 2013

B.S. Applied Physics

Research Experiences

Kyung Hee Uuniversity, Department of Applied Physics

Prof. Suk-Ho Choi's Lab. (2011 ~ 2012)

- Research on the single layer graphene transfer processes

Seoul National University, Department of Physics

Prof. Hye Yoon Park's Lab. (2013 ~ 2015)

- Movable objective microscope & two photon microscope setup

- Neuron cell culturing

- mRNA tracking program development (based on MATLAB)

- Research on dynamics of neuronal messenger ribonucleoprotein transport

Prof. Gyu-Chul Yi's Lab. (2016 ~)

- Photoluminescence measurement system setup

- MOCVD system setup

- Single addressable GaN micro LED growth & fabrication

- ZnO nanotube pressure sensor

- Bio application using ZnO nanotubes (molecular delivery channel, neural probe, wave guide)

Journal Publications

1. Y. Tchoe, **M. S. Song**, H. Kim, H. Baek, J. Y. Park, H. Oh, K. Lee, K. Chung, J. K. Hyun, G.-C. Yi, Individually addressable, high-density vertical nanotube Schottky diode crossbar array. Nano Energy. 104955 (2020)

2. **M. S. Song**, H. C. Moon, J.-H. Jeon, and H. Y. Park, Neuronal messenger ribonucleoprotein transport follows an aging Lévy walk. Nature Communications. 9, 344, (2018)

3. H. Baek, H. Kwak, **M. S. Song**, G. E. Ha, J. Park, Y. Tchoe, J. K. Hyun, H. Y. Park, E. Cheong, and G.-C. Yi, ZnO nanotube waveguide arrays on graphene films for local optical excitation on biological cells. APL Materials. 5, 046106, (2017).

4. H. C. Moon, B. H. Lee, K. Lim, j. Son, **M. S. Song**, and H. Y. Park. Tracking single mRNA

molecules in live cells. Journal of Physics D: Applied Physics, 49(23), 233001, (2016).

5. H. Y. Park, **M. Song**, Visualizing mRNA Dynamics in Live Neurons and Brain Tissues. Post-Transcriptional Gene Regulation, 325-334, (2016).

Manuscripts under preparation

1. **M. S. Song**, J. B. Park, R. Ghosh, B. Kim, S.-W. Kim, and G.-C. Yi, Highly-sensitive, flexible pressure sensors using ZnO nanotube arrays grown on graphene films. (aiming at Nano Energy)

2. **M. S. Song**, H. Baek, K. Lee, D. Yoo, K. Chung, and G.-C. Yi, Intracellular GaN microrod laser. (aiming at APL Materials)

Conference Presentations

1. **M. S. Song**, H. Baek, and G.-C. Yi, Intracellular GaN microrod laser. Nano Korea (2019).

2. **M. S. Song**, H. Baek, and G.-C. Yi, Intracellular GaN microrod laser. Korean Physical Society (2019).

3. **M. S. Song**, H. Baek, and G.-C. Yi, Intracellular GaN microrod laser. CLEO Laser Science to Photonic Applications (2019).

4. H. Baek, H. Kwak, **M. S. Song**, G. E. Ha, J. Park, Y. Tchoe, J. K. Hyun, H. Y. Park, E. Cheong, and G.-C. Yi, ZnO nanotube waveguide arrays on graphene films for local optical excitation on biological cells. OSA bio photonics congress: optics in the life sciences (2017).

5. **M. S. Song**, H. C. Moon, J.-H. Jeon, and H. Y. Park, Observing a Levy walk in mRNA transport in neurons, Korean Physical Society (2014).

Patents under preparation

1. 이규철, **송민호**, 박준범, 눌림힘과 표면 쓸림힘의 방향을 감지하는 유연한 압력센서. Korean Patent 1020200066710 (pending)

Award and scholarship

1. Excellent presentation award, Applied Physics, Korean Physical Society (2019)

2. Full scholarship, Korea Student Aid Foundation (2011)

Expertise

1. Material growth

   ● Highly experienced with operation, maintenance, and setup in MOCVD for GaN and ZnO growth

   ● Dimension and position-controlled nanostructure growth of GaN and ZnO using MOCVD

   ● CVD graphene growth on Cu foil using CVD

2. Nano/microfabrication

- Highly experienced with ultra-flexible device fabrication

- Highly experienced with nano- and micro- structure ZnO and GaN based device fabrication

3. Material characterization

- Highly experienced with Pressure Photoluminescence spectrometer integrated with He-cryostat and electroluminescence setup, micro-Raman spectrometer, UV-Vis-NIR spectrometer

- Highly experienced with e-beam lithography and imaging with (FE)SEM system

- Highly experienced with fluorescent optical microscope and two photon microscope setup and characterization

4. Computational Skill

- Development of single particle tracking program for single RNA tracking in neuron cells using MATLAB

- FDTD simulation for wave guiding experiment using Lumerical

5. Biological experiments

- Neuron cell culturing

- *In vivo* and *in vitro* imaging using two photon and fluorescent microscope